Liquid Precursors in Non-Classical Crystallization

Dissertation

Submitted for the degree of Doctor of Natural Science

“doctor rerum naturalium”

Presented by

Wolf, Stefan Leo Philipp

at the

Universität Konstanz

Mathematisch-Naturwissenschaftliche Sektion

Fachbereich Chemie

Tag der mündlichen Prüfung: 09. Juni 2017

1. Referent: Dr. Denis Gebauer

2. Referent: Prof. Dr. Helmut Cölfen

“Was einmal gedacht wurde kann nicht mehr zurückgenommen werden”

Friedrich Dürrenmatt

Die Physiker 1962

Vorwort

Die vorliegende Arbeit entstand zwischen Mai 2013 und Dezember 2016 vorwiegend an der Universität Konstanz und in Kooperationen mit der Universität Bayreuth, der Universidad de Santiago de Chile und der Ruhr Universität Bochum.

Ohne die Hilfe und Unterstützung von vielen Personen wäre diese Arbeit nicht möglich gewesen. Daher möchte ich mich bei vielen Menschen bedanken die mir sowohl das Leben als auch die Arbeit erfreulicher und angenehmer gestaltet haben.

An erster Stelle möchte ich Dr. Denis Gebauer und Prof. Dr. Helmut Cölfen danken. Nicht nur für das entgegengebrachte Vertrauen und das interessante Thema, sondern vor allem für die immer sehr schöne Zeit die wir sowohl bei wissenschaftlichen Diskussionen aber auch auf AG Ausflügen oder Konferenzen verbracht haben.

Des Weiteren möchte ich allen meinen Kollegen und Kommilitonen für die nicht immer angenehme aber stets schöne Zeit im Büro und im Labor danken. Meinen Freunden möchte ich für die unterhaltsamen Stunden außerhalb der Universität danken, hierzu zählen auch die geselligen Abende in Bars und Kneipen von Hanga Roa über Valencia bis nach Konstanz.

Für die sehr vielen Stunden, die Herr M. Hagner und Frau Dr. M. Krumova bei der Einführung in unterschiedlichste Geräte geopfert haben möchte ich mich herzlichst bedanken. Ebenso bedanke ich mich bei Dr. F. Sebastiani und Dr. B. Born für die THz Messungen und bei Herrn L. Caballero für die *in-situ* AFM Messungen.

All meinen HiWis, Bachelor und SPK Studenten danke ich für die geleistete Arbeit und den angenehmen Stunden im Labor. Andra-Lisa Hoyt, Julian Brunner und Ricarda Weiler möchte ich für die Korrektur der vorliegenden Arbeit danken.

Musik hat mir während den vergangen Jahren immer sehr geholfen, sowohl um Ruhe und Ausgeglichenheit, als auch um Inspiration und Ablenkung gleichermaßen in ihr zu finden. Daher sei hier einer kleinen Auswahl an Künstlern gedankt: InFlames, Motörhead, Amon Amarth, Slayer, Heaven Shall Burn, Arch Enemy, Kreator, Dritte Wahl, Behemoth, Dimmu Borgir und Sonic Hiker.

Zu guter Letzt möchte ich noch meinen Eltern und Großeltern für die grandiose Unterstützung während meines gesamten Studiums danken ohne welche diese Arbeit nicht möglich gewesen wäre. Vielen Dank dafür.

Table of Content

1. Introduction[1]

Clouds affect the climate directly as they absorb infrared light and reflect incoming sun light. Every cloud formation needs the occurrence of nucleation sites – in this case dust particles – to start their growth.[1] The formation of raindrops, snowflakes or hailstones in clouds also involves the formation of a metastable nucleus, which can then further evolve – depending on temperature and pressure – to rain showers, snow or hailstorms.[2] Nucleation events are crucial for climate and, consequently, also for climate change on our planet. Such processes play an important role for our climate not only in the atmosphere but also for the carbon dioxide equilibrium in the oceans.[3] The absorption of carbon dioxide by the oceans is the biggest consumption of anthropogenic carbon dioxide.[3-5] Atmospheric carbon dioxide is the main source for carbonate ions, which are fundamental for nucleation events during the formation of calcium carbonate – the most abundant biomineral – in the oceans.[6-7]

Biominerals are formed *via* biomineralization, which is a cell mediated nucleation and crystallization process by which marine animals produce complex structures for different applications such as organs of visions, defence structures or masticatory.[6-10] Biominerals have improved properties compared to the geological occurrence of such materials, e.g. improved toughness in case of bivalve shells.[11-12] Due to the complexity of biomineralization, it is not entirely understood yet.[13] So far, it is known that some ions like magnesium or citrate and specialized proteins play a key role during biomineral formation.[14-15] Despite the lack of understanding of biomineralization, scientists seek inspiration from the outstanding properties of biominerals to produce advanced materials by means of biomimetic material design.[6]

Calcium carbonate is not only an important mineral for our environment and nature but also of high interest for industrial applications.[16] It is used in many industrial areas, *e.g.* in construction, paper production, agriculture or health care. In each of these fields, calcium carbonate is used for different reasons; in paper production it is used as a brightener, in agriculture to mediate the pH of the soil, and in construction as a filler material. However,

---

[1] Parts of this chapter are published in *Angew. Chem. Int Ed,* **2017**, 56, 490-495, *Langmuir* **2017**, 33,158-163, and *CrystEngComm* **2015**, 17, 6857-6862. For the sake of readability not all passages assumed from the published manuscript are marked by quotation marks (“ ”) additionally. Figures taken from these publications are also not marked additionally.

sometimes there is unwanted crystallization of $CaCO_3$ in pipelines (scaling) that can be prevented by additives, so-called anti-scalants.[17]

Nucleation events have attracted the attention of scientists since the beginning of the last century.[18] To describe the formation of water droplets in a saturated atmosphere, classical nucleation theory (CNT) was developed.[19] Afterwards, CNT was applied to describe the precipitation and crystal growth in aqueous media.[20-22] One very important subject of research in the field of nucleation and crystallization is calcium carbonate, which is investigated since the early 20th century.[23-24] Nevertheless, a complete model to predict the nucleation of calcium carbonate in aqueous solution is still missing.[25-26] This work provides further insights into the underlying mechanism of the nucleation and crystallization pathways of calcium carbonate in aqueous solution.

Due to experimentally observed discrepancies with CNT, this theory was developed further over several decades, e.g. by the introduction of kinetic contributions from Farkas[27-28] or later by the introduction of pre-exponential-factors like the Zeldovich factor.[29] CNT assumes stochastic density fluctuations in the supersaturated system: when molecules, atoms, or ions – like in the calcium carbonate system – collide, a nucleus can be formed. This nucleus then can grow or disappear, depending on its size. The free energy (ΔG_{ex}) of such a nucleus and, therefore, its stability is controlled by two different contributions, a surface contribution (interfacial energy) – which scales with the square of the radius of the nucleus – and a bulk contribution – which scales with the cube of the radius. The contributions of both counterparts are schematically shown in Figure 1.

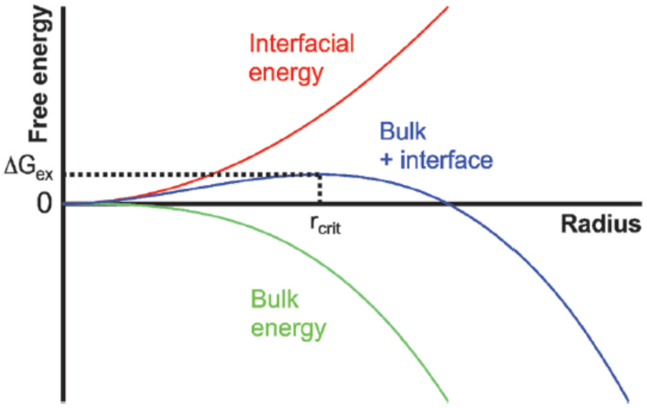

Figure 1 | Schematic illustration of the interfacial energy (red) and the bulk energy (green) and the sum of both (blue). This image is re-used from ref.[18]

A mathematical description is given in equation 1. The first part relates to the bulk energy and the second to the surface part:

$$\Delta G = \frac{4}{3}\pi r^3 \Delta G_v + 4\pi r^2 \gamma \tag{1}$$

Here r is the radius and γ is the surface tension of the nucleus. ΔG_v is the free energy change of the conversion from ions in solution to a solid.[30] The free energy change of the transformation per unit volume ΔG_v can be written as follows.

$$\Delta G_v = \frac{-k_b T \ln S}{v} \tag{2}$$

S is the supersaturation defined as ion activity product (IAP) divided by the solubility constant K_{sp} (for minerals in aqueous solution), k_B is the Boltzmann constant, *T* the Temperature and ν the molecular volume. To find the maximum of the blue curve in Figure 1 and the corresponding critical free energy, the first derivation of ΔG must be set to zero.

$$\frac{dG}{dr} = \Delta G_{ex} = 4\pi r^2 \Delta G_v + 8\pi r \gamma = 0 \tag{3}$$

Therefore, r_{crit} can be calculated and inserting of equation 2 in equation 3 yields:

$$\Delta G_{ex} = \frac{16\pi\gamma^3 v^2}{3(k_B T \ln S)^2} \tag{4}$$

Nucleation rates (*J*) can be calculated with these values, using the Arrhenius reaction velocity equation and a material dependent pre-exponential factor A:[31-32]

$$J = A \cdot exp\left(\frac{\Delta G_{crit}}{k_B T}\right) \tag{5}$$

In all of these equations CNT assumes that all properties of the critical nucleus are the same as the bulk properties (γ, ΔG_v) – the so called capillary assumption.[25, 31] Below the critical size of the nucleus, the free energy is positive and therefore the nucleus will dissolve. Above r_{crit} ($dG_{ex}/dr < 0$) the energy barrier is crossed and an instable nucleus is formed which then grows larger by ion addition with the rate *J* until the final crystal is formed.

Calcium carbonate was considered for a long time to be the prime example for the CNT.[33-34] Nevertheless, there is a huge discrepancy between experimental observations and the theoretically predicted nucleation rates.[35] In 2008 Gebauer *et al.* discovered the existence of pre-nucleation clusters (PNCs) in aqueous calcium carbonate solutions.[36] The presence of PNCs was shown by means of analytical ultracentrifugation and by the amount of bound calcium and carbonate ions during the addition of calcium chloride to a bicarbonate buffer in undersaturated, in saturated, and supersaturated solutions. PNCs can also occur in other systems like calcium phosphates, iron oxides or amino acids.[37-39] Molecular dynamic simulations indicate that $CaCO_3$ PNCs consist of alternating calcium and carbonate ions, a structural motive called dynamically ordered liquid like oxyanion polymers (DOLLOPs).[40] As result, PNCs are solutes, highly dynamic, and in equilibrium with ion pairs. The pH value influences the cluster stability and therefore the structural motifs of the PNCs.[36] In Figure 2 the PNC pathway and the classical pathway are shown schematically:

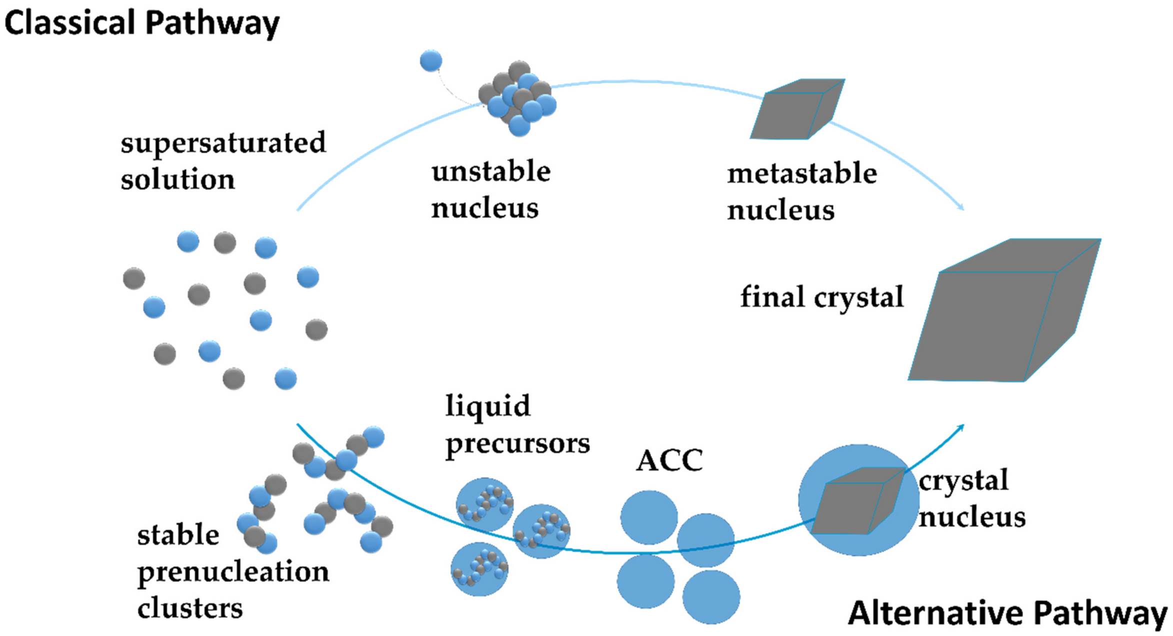

Figure 2 | Schematic comparison of the classical (top) and the PNC pathway (bottom); based on [19]

Computer simulations also suggest that upon reaching a certain critical ion activity product (IAP), the clusters can internally develop higher coordination numbers than in the initial chain-like form.[40-41] This was interpreted as entering a metastable state with respect to liquid-liquid demixing,[25, 42] whereas the loci of the corresponding binodal and spinodal limits remain yet unknown. It was proposed that upon binodal demixing, pre-nucleation clusters become nanodroplets whose aggregation is driven by the reduction of interfacial surface area. Later, these phases can solidify or undergo a second nucleation event, yielding amorphous calcium carbonate (ACC) and finally crystals. During this densification process a liquid-liquid phase separation must occur as first postulated by Faatz *et al.*[42] Experimentally Gower and co-workers were the first to observe such a liquid mineral phase.[43-44] Due to the presence of polymers in their experiments they named this species polymer-induced liquid precursors (PILP).[44-45] They also speculated that PILPs may play a key role in biomineralization as they form under the influence of polycarboxylates – namely poly(aspartic acid) – which occur remarkably often as repeating units in peptides involved in biomineralization.[6, 13, 46-49] Liquid mineral phases of calcium carbonate subsequently received more attention by scientists. For example, Wolf *et al.* reported the observation of a liquid phase in a levitated drop experiment by means of cryogenic (cryo-) SEM and TEM.[50-51] The liquid character of the PILP phase was demonstrated by a spin-spin (T_2) relaxation time NMR study.[52] Two different diffusion coefficients for two different carbonate species were observed, one belongs to PILPs the other to free ions in solution. These results concerning liquid-liquid phase separation were recently supported by molecular dynamic simulation.[41] Experimental evidence for the location of the liquid-liquid binodal limit will be part of this project.

Based on the PNC-pathway different pH values and additives lead to different ACCs.[36] ACCs can exhibit short range order relating to crystalline calcium carbonate polymorphs.[53] The three different anhydrous polymorphs of calcium carbonate are calcite (with a trigonal crystal system), aragonite (which crystallizes in an orthorhombic crystal symmetry), and vaterite (which exhibits a complex hexagonal lattice together with another coexistent structure rotated by 30°).[54-55] Short-range orders in ACCs, which are related to structural motives of their crystalline counterparts, can be identified by means of ss-NMR, EXAFS and IR spectroscopy. The chemical shifts, calcium-oxygen distances and dipole moments of the ACCs observed by the above mentioned methods can be assigned to the anhydrous forms of $CaCO_3$ and are therefore named proto-calcite- (pc), proto-vaterite- (pv) and proto-aragonite- (pa)

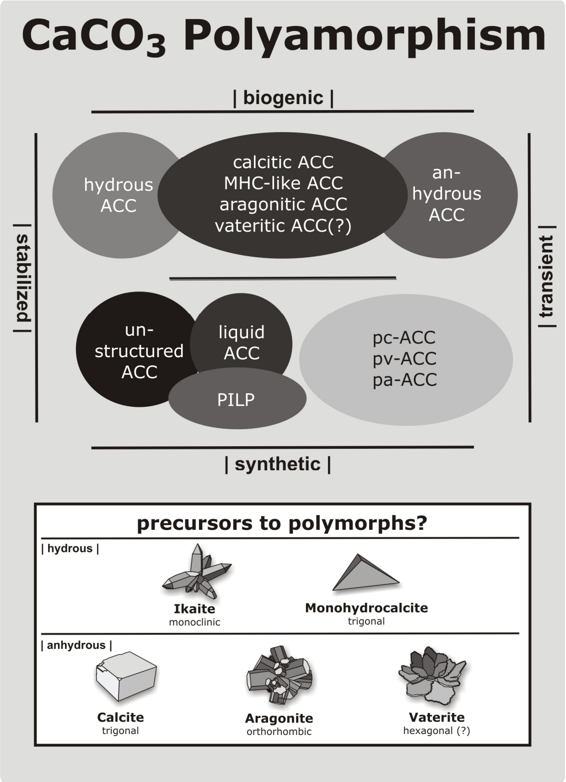

Figure 3 | Classification of different ACCs and of crystalline forms of CaCO$_3$. Figure taken from ref.[41]

ACC.[53, 56] A listing of all known ACCs is presented in Figure 3. Proto structured ACCs can also be found in nature e.g. in *Pyura Pachidermatina*, a sea tulip. (*cf.* Figure 3).[57]

Amorphous materials are very important for invertebrates due to manifold reasons, an overview of different ACCs and their functions produced by marine animals can be found in the literature.[58] In some cases, ACC also acts as a precursor for the final crystal in biominerals.[59-60] In other cases, ACC can improve the toughness of the resulting materials, *e.g.* in the sea urchin spine.[61]

Macroscopic properties of biominerals like the Young's modulus or the stiffness are mainly dominated by a complex interplay between inorganic crystals causing the toughness, and organic macromolecules, which cause the elasticity, sometimes – as mentioned above – also by incorporation of amorphous material.[61-62] Therefore, it is expected that bio-macromolecules have a great influence on the nucleation and crystallization pathway.[59] In nature, also rather simple additives like magnesium, phosphate or citrate ions occur to stabilize ACC particles in addition to macromolecules.[63-64]

The role of magnesium ions in calcium carbonate formation has been studied particularly well [63, 65] because of its relevance in biomineralization and its presence in sea water.[58, 66-68] While their main function appears to relate to the kinetic stabilisation of amorphous calcium carbonate (ACC), magnesium ions are also required for the wetting of proteinaceous organic matrices by liquid precursors of CaCO$_3$.[69] Such PILPs[44] are effectively stabilised by polycarboxylates – as mentioned above –, which have also been studied in combination with magnesium ions.[70-72] In the case of magnesium-stabilised ACC, aspartic-acid rich molecules can trigger crystallisation, which can be understood by an enhanced desolvation of the hydrated precursors.[71] On the other hand, carboxylated molecules regulate the Mg/Ca ratio in ACC based on sequence-dependent binding affinities for the two ions.[73] This illustrates that the combination of magnesium ions with carboxylated molecules can probably give rise to synergistic effects for controlling $CaCO_3$ formation.

Quantitative studies utilising a so-called titration assay have shown that different classes of additives — ranging from simple ions and molecules like sugars and amino acids to complex macromolecules that can effectively influence $CaCO_3$ precipitation — have different effects,[74-78] and interact with the nascent calcium carbonate before, during, and after nucleation. While magnesium ions[79] and poly(aspartic acid)[76] have already been investigated in this way individually and exhibit distinct effects, a study of both additives with the focus on nucleation and not on the final crystal structure, in one system has not been performed.

Not only the nucleation of (bio)minerals can follow non-classical pathways, but also the subsequent crystal growth can follow non-classical particle-based pathways[80-81] including oriented attachment[82-83] or mesocrystal formation.[84-85] This novel view also includes the presence of liquid precursors and amorphous intermediates.[6, 52, 55, 69] Such intermediates are generally known for their appearance in protein crystallization as well.[86-88] Such precursors are also intermediates in the crystallization of amino acids or other small molecules like dyes. In these cases, the liquid precursors could be isolated by centrifugation.[89-91] Nevertheless, a characterisation of the physical properties of liquid precursors for calcium carbonate or any other inorganic crystal system was not possible. PILPs can be used for crystal growth by the addition of liquid precursors to a substrate or a seed crystal and for bio-inspired material synthesis.[6, 92-95] A nanoscopic observation of the growth mechanism of such liquid precursors is, however, still an open challenge.

2. Objective

Nucleation events are crucial for many fields in sciences and for our day-to-day live. One of the most important systems in this case is calcium carbonate. However, a complete description of the different nucleation and crystallization pathways in this system is still missing. The focus of this thesis lays on the investigation of the early phase transitions in the aqueous calcium carbonate system and is organized in four main chapters. In the first chapter the locus of the liquid-liquid binodal, which was postulated theoretically,[41-42] shall be located experimentally. THz spectroscopy is the method of choice to observe changes in water dynamics, which have to occur during a liquid-liquid phase separation. Therefore, it is possible to locate the liquid-liquid binodal by a combination of THz spectroscopy together with a titration assay. In the second chapter, a phase diagram for different ACCs formed *via* solidification of the second liquid phase shall be constructed. For this purpose temperature- and rate-dependent titration experiments are performed to investigate the temperature dependency of the liquid-liquid binodal limit. These experiments also reveal the stability of the second liquid phase and of the nucleated ACCs. This knowledge can be a huge step towards a better understanding of (bio-)mineralization processes. The third chapter shall explore the influence of additives on the liquid-liquid binodal limit, which will also be obtained by use of the above mentioned methods. In addition, a combination of different additives is investigated to develop new strategies for anti-scalants. In the last chapter, the physical behavior of liquid precursors stabilized by polymers shall be the main task. *In-situ* AFM is a powerful technique to gain information about the Young's modulus and morphology of the liquid precursors, which leads to insights into non-classical growth mechanisms of $CaCO_3$.

To sum the above mentioned up, the main scopes of the thesis are:

- Determination of the locus of the liquid-liquid binodal in the aqueous $CaCO_3$ system
- Construction of a phase diagram for the polyamorphs of calcium carbonates formed *via* solidification
- Investigation of the stability of ACCs nucleated at different stages in the phase diagram
- Exploration of the influence of different additives on the liquid-liquid binodal and on the stability of the nucleated ACCs
- Characterization of the physical properties of the liquid precursors during crystal growth

3. Methods and Experimental

3.1 Electrodes

3.1.1 pH Electrodes

The most commonly used electrodes are pH electrodes and have in-built reference electrode, usually silver/silver chloride, sometimes a mercury/amalgam reference is used. The membrane has to be selective for protons or hydronium ions. At the membrane a potential evolves due to the concentration difference between protons and hydronium ions on either side of the membrane, quantified by the Nernst law. Common electrodes have glass membranes, which are still state of the art concerning live time, selectivity and manufacturing. The glass consists of a mixture of different salts, like CaO, Na_2O, Al_2O_3 and the main component SiO_2.[96] The composition of the glass membrane is one of the best-kept secrets of the manufacturers of the electrodes.

In this work a polymer membrane electrode was used. The membrane consists of protonophores, a conducting salt, a poly(vinyl chloride) matrix and, a softener.[96]. The most common protonophores are tridodecylamine (TDDA), methyldioctadecylamine (MDUDA) and octaphenylcyclotetrasilane.[97-98] The main advantage of the polymer membrane is the fast reaction times caused by the flat and thin membrane. The major drawback is the short lifetime of such electrodes in comparison to glass membrane electrodes.

3.1.2 Ion-Selective Electrodes

A pH electrode is also an ion-selective electrode (ISE), which is selective for hydrogen ions. An ISE for Ca^{2+} ions was applied, to measure the activity of calcium ions in solution. A Ca^{2+}-ISE consists of a polymer membrane, which includes selective organic molecules for calcium transport.[99] These so called ionophores are available for several different cations and anions. A summary for different cations can be found in the literature.[100] For calcium ions, several different macromolecules have been developed.[99]. The membrane is constructed like the polymer membrane for the pH electrode but with other ionophores specific for calcium ions. A reference solution is placed on the other side of the membrane within the electrode. As a result, from different potentials of the reference solution in the electrode and the investigated solution, a potential difference is formed. This potential difference can be measured and evaluated according to Nernst's law (*cf.* chapter 3.6). As a reference electrode for the Ca^{2+}-ISE the in-build reference of the pH electrode was used.

3.2 Electron Microscopy

The de Broglie equation describes the wave-particle duality – stating that electrons also have a wavelength dependent on their mass and momentum. Therefore, they can be used for observations in a microscope. The applied voltage at the cathode can control the speed and therefore the wavelength of the electrons. The wavelength of an electron with an applied voltage of 100 kV is 0.012 nm, so a sub-nanometre resolution can be achieved. If the electron is interacting with a specimen, different events can occur. They are summarized in Figure 4.

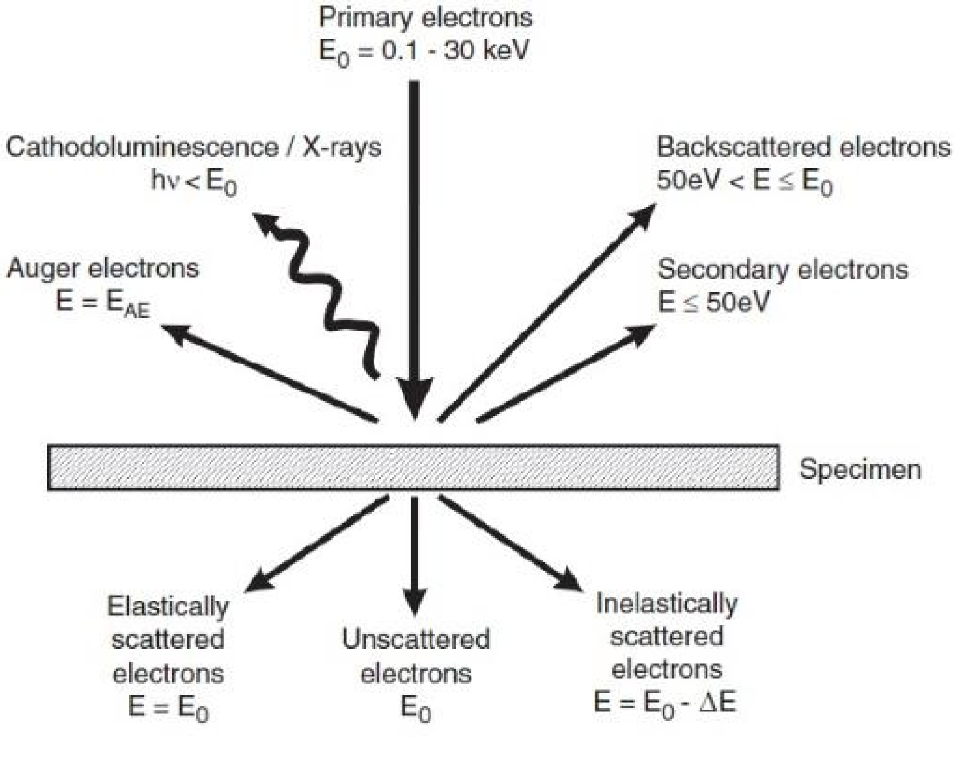

Figure 4 | Possible results of the interaction of an electron with a specimen. This graph is re-used from ref [95]

Of all these events, the backscattered electrons and transmitted electrons are crucial for imaging techniques, like transmission electron microscopy (TEM) and scanning electron microscopy

(SEM).[101] By analysis of emitted Auger electrons and X-rays, information about the chemical composition can be gained.

TEM and SEM were developed to achieve better resolutions than in classic light microscopes. The setup of TEM exhibits similarities to that of a light microscope. The two big differences are that magnetic coils are used instead of optical lenses and, of course, the light source is an electron beam instead of a lamp. The acceleration voltage of TEMs lie in the range of 120 kV and 300 kV for commercially available devices. For the visualization a CCD camera is used to take pictures. If an electron beam interacts with a sample, as shown in Figure 4, the beam is weakened and scattered. The weakening depends on the atomic number of the atom because the beam is scattered only by the electrons and their counts increases with the atomic number.

In SEMs the energy is lower as the acceleration voltage is normally between 5 kV and 20 kV. In this electron microscopy approach, not the transmitted electrons are detected but the backscattered electrons. A picture of the morphology can be gathered because less electrons are backscattered at edges and corners compared to flat surfaces.

3.3 Titration Setup

A commercially available titration set-up manufactured by Metrohm AG was employed. The titration software tiamo 2.3 and a titration robot (Metrohm) Titrando 809 with two Dosing Units 807 with a volume of 2 mL (No.: 6.3032.120) was utilized. For the calcium potential measurements an ion-selective electrode (ISE) (No: 6.0508.110) and for pH-measurements a pH-electrode (No.: 6.0256.100) both manufactured by the Metrohm AG were used. The pH-electrode was applied as the reference electrode for the ISE. All experiments were carried out in a 150 mL vessel.

Experiments where calcium chloride solution was titrated into bicarbonate buffer are labelled $Ca^{2+}{\rightarrow}CO_3^{2-}$ and in the *vice versa* case $CO_3^{2-}{\rightarrow}Ca^{2+}$ titrations. For an addition rate of 0.1 µmol/min a 10 mM calcium chloride solution was titrated at a rate of 0.01 mL/min into a 10 mM bicarbonate buffer at the designated pH value. A 10 mM NaOH solution was used to keep the pH constant. For addition rates of 1.0 µmol/min and 10 µmol/min, a 100 mM calcium chloride solution was titrated into sodium bicarbonate buffer (10 mM) at a rate of 0.01 mL/min and 0.1 mL/min, respectively. Here, a 100 mM sodium hydroxide solution was applied to keep the pH constant. The temperature was controlled by a FP50 thermostat obtained from Julaba. The reproducibility of the experiments is shown in the appendix (Figure 43 for pH 9.0 and in Figure 44 for pH 10, respectively). For the experiments described in chapter 4 the NaOH concentration was 10 mM for the THz experiments and 30 mM for all other experiments.

3.4 Direct Mixing Experiments

Solutions of sodium carbonate and calcium chloride with concentrations of 100 mM and 1000 mM were prepared. For each experiment, 50 mL of a $CaCl_2$ solution was poured into 50 mL of a Na_2CO_3 solution of the same concentration. The pH value was observed by a pH electrode and kept constant at pH 9.0 due to the addition of 1000 mM NaOH solution. The activity of Ca^{2+} ions was measured by a Ca^{2+}-ISE over the duration of the complete experiments, which run for several hours. The data evaluation was carried out as described in chapter 3.6.

3.5 Calibration

The pH-electrode was calibrated by a three point calibration with pH-buffers of pH = 4.01, pH = 7.00 and pH = 9.21. These were obtained by Mettler-Toledo with the product numbers: pH = 4.01: 51 302 069; pH = 7.00: 51 302 047; pH = 9.21: 51 302 070.

The calcium ISE was calibrated differently for the two different experiments described in chapter 4. For the $Ca^{2+} \rightarrow CO_3^{2-}$ experiment (*cf.* chapter 3.3) the Ca^{2+}-ISE were calibrated by the slow addition of a 10 mM calcium chloride solution into water at the same pH as the experiments were performed. The pH was kept constant by counter titration with NaOH solution. During the calibration of the ISE it is necessary to purge the vessel with nitrogen to prevent carbon dioxide diffusion into the solution. Thereby an undesired binding of Ca^{2+}-ions by carbonate can be suppressed. If other ions, such as magnesium, were present in the experiments the calibrations were performed with the same ratio of Ca^{2+}/Mg^{2+} as conducted in the experiment.

For the $CO_3^{2-} \rightarrow Ca^{2+}$ (*cf.* chapter 3.3) titrations the Ca^{2+}-ISE was calibrated before every measurement. Here also a three point calibration was applied, utilizing three calcium chloride solutions with concentrations of 0.1 mM, 1.0 mM and 10 mM. All solutions had an ionic strength of 30 mM. To keep the pH value constant, a 30 mM NaOH solution was used. To average out random fluctuations in the electrode potential every concentration was measured over 1000 s, and a data point was recorded every two seconds, which results in 500 data points. The mean of these 500 data points for every concentration was used for the calibration of the ISE. A logarithmic plot of the theoretical concentrations against the measured potential leads to a straight line, which is used to evaluate the data resulting from the experiment per the Nernst law (Figure 5). The electrode-intercept cannot be determined exactly by this calibration method. The starting calcium concentration differs from the exact value of 10 mM when the calibrated value is directly applied. Therefore the y-intercept was adjusted so that the starting concentration of $[CaCl_2]$ = 10 mM was matched. The value for the corrected y-intercept lies within the standard derivation of 15 independent calibrations.

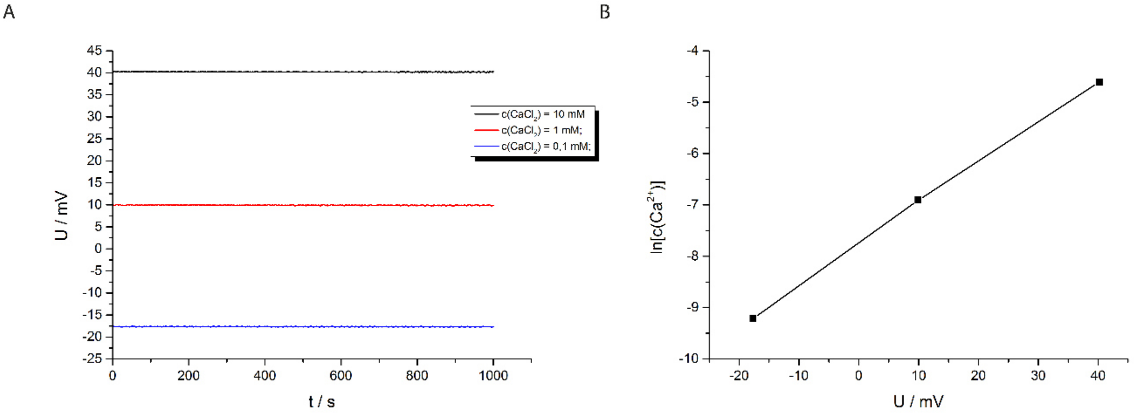

Figure 5 | Examples of the calibration data points (A; Ca^{2+} concentrations: blue: 0.1 mM; red: 1.0 mM; black 10.0 mM) and the resulting calibration straight from the points (B)

3.6 Data evaluation

3.6.1 Data from calcium potential measurements

The ion activity product (IAP) and the ion pairing product (IP) are crucial for a thermodynamic analysis of the experiments – to calculate solubility products (K_{sp}) and cluster formation constants ($K_{cluster}$). The underlying calculations are presented in the following section.

The measured calcium potentials are evaluated taking activity coefficients into account. The activity is defined as:

$$a = \gamma \cdot c \tag{6}$$

Where a is the activity, γ the activity coefficient ($0 < \gamma \leq 1$) and c the concentration. To this end, the potentials are treated in accordance to the following procedure. The use of the Nernst law results in the activity of the measured calcium ions. The activity coefficient is always smaller than one ($\gamma < 1$) in the applied concentration regime, which is taken into account in the following equations.[102-103]

$$U = U_0 + \frac{RT}{zF} \ln \frac{a}{a^{\oplus}} \tag{7}$$

Here U is the measured potential, U_0 is the standard potential of the ISE, R is the universal gas constant, T the absolute temperature, z the charge valence of the measured ion, F the Faraday constant and $a^{\oplus}$is the standard activity. Because the activity coefficient can not be measured for a single ion like it is discussed by Malatesta the apparent activity coefficient (γ_{app}) has to be applied.[104] Therefore the activity coefficient is rewritten as:

$$a = \gamma_{app} \cdot c \tag{8}$$

The activity coefficient can be calculated using the Debye-Hückel limiting law, which applies for ionic strength regimes < 100 mM. The apparent activity coefficient can be calculated using the following equation:

$$\gamma_{app} = (\gamma_{Ca}^{1} \cdot \gamma_{Cl}^{2})^{\left(\frac{1}{2+1}\right)} \tag{9}$$

Where γ_{Ca} is the activity coefficient for the calcium ions and γ_{Cl} is the activity coefficient for the chloride ions, respectively. The different activity coefficients depend on the ionic strength of the solution. The ionic strength (I) is defined as:

$$I = \frac{1}{2} \sum_i z_i^2 \cdot c_i \tag{10}$$

Here again, z is the charge valency of the ion i and c is the concentration of the ion i. The single activity coefficients can be calculated – in the applied concentration regime – by the extended Debye-Hückel equation, which is given as:

$$\log \gamma_i = -A \cdot z_i^2 \cdot \left(\frac{\sqrt{I}}{1+B\cdot a_0\sqrt{I}}\right) \tag{11}$$

Here a_0 is a parameter for the distance between the different ions.[105] Furthermore A and B are constants, which depend on the temperature and the relative permittivity ε_r of the solvent and are given as:

$$A = \frac{e^2\cdot B}{2.303\cdot 8\pi\varepsilon_0\varepsilon_r k_B T} \tag{12}$$

$$B = \frac{2\cdot e^2\cdot N_A}{\varepsilon_0\varepsilon_r k_B T} \tag{13}$$

Here ε_0 is the permittivity of the vacuum, k_B the Boltzmann constant and N_A Avogadro's number. For 289.15 K and water as a solvent the values for A and B can be calculated, according to the literature, to -0.5085 $M^{-0.5}$ and 3.281 $M^{-0.5}nm^{-1}$, respectively.[105] Hence, the values for the activity coefficients of the two species (Ca^{2+} and Cl^-) can be calculated as follows:

$$\gamma_{Ca} = -0.5085\ M^{-0.5} \cdot 2^2 \cdot \left(\frac{\sqrt{I}}{1+3.281\ M^{-0.5}nm^{-1}\cdot 0.6\ nm\cdot\sqrt{I}}\right) \tag{14}$$

$$\gamma_{Cl} = -0.5085\ M^{-0.5} \cdot (-1)^2 \cdot \left(\frac{\sqrt{I}}{1+3.281\ M^{-0.5}nm^{-1}\cdot 0.3\ nm\cdot\sqrt{I}}\right) \tag{15}$$

With this knowledge and equation 7 the Nernst law can be rewritten:

$$U = U_0 + \frac{RT}{zF}\cdot \ln\left(\frac{\gamma_{app}\cdot c(Ca^{2+})}{c^{\oplus}}\right) \tag{16}$$

$$U = U_0 + \frac{RT}{zF}\cdot \ln \gamma_{app,1} + \frac{RT}{zF}\cdot \ln\left(\frac{c(Ca^{2+})}{c^{\oplus}}\right) \tag{17}$$

$$\ln\left(\frac{c(Ca^{2+})}{c^{\oplus}}\right) = \frac{2F}{RT}\cdot U(Ca^{2+}) - \frac{2F}{RT}\cdot U_0 - \ln \gamma_{app,1} \tag{18}$$

$$c(Ca^{2+}) = c^{\oplus}\cdot exp\left[\frac{2F}{RT}\cdot U(Ca^{2+}) - \frac{2F}{RT}\cdot U_0 - \ln \gamma_{app,1}\right] \tag{19}$$

Where $\gamma_{app,1}$ is the activity coefficient during the calibration experiment. Therefore, the y-intercept b of the calibrations can be expressed as:

$$b_1 = -\frac{2F}{RT} \cdot U_0 - \ln y_{app,1} \tag{20}$$

Whereas the slope m of the straight line is given by:

$$m = \frac{2F}{RT} \tag{21}$$

It has to be taken into account that the activity coefficient γ_{app} differs between the calibration and the measurement as a consequence of the addition of the titrant and the sodium hydroxide to the reaction solution during the experiment. If the ionic strength I is calculated over the experiments development, a change in I can be observed. This leads to a difference in the electrode intercepts of the calibration and of the measurement. From this follows an implementation of a real activity coefficient $\gamma_{app,2}$ dependent on the ionic strength during the measurements. This leads to a different y-intercept than in the calibration.

$$b_2 = -\frac{2F}{RT} \cdot U_0 - \ln y_{app,2} \tag{22}$$

Because the y-intercept during the calibration influences the following calculations the b value has to be adjusted to the form:

$$b = -\frac{2F}{RT} \cdot U_0 + \ln y_{app,1} - \ln y_{app,2} \tag{23}$$

$$c(Ca^{2+}) = c^{\oplus} \cdot exp\left[\frac{2F}{RT} \cdot U(Ca^{2+}) - \frac{2F}{RT} \cdot U_0 + \ln \gamma_{app,1} - \ln \gamma_{app,2}\right] \tag{24}$$

This equation can finally be written as a standard straight line equation, from which the calcium concentration can be calculated from experimental data:

$$c(Ca^{2+}) = c^{\oplus} \cdot exp[m \cdot U(Ca^{2+}) - b] \tag{25}$$

With that knowledge, it is possible to calculate the actual Ca^{2+}-concentration and the concentration of bound calcium ions ($c_{bound}(Ca^{2+})$). The measured concentration expressed as $c_{free}(Ca^{2+})$ and the theoretical calcium concentration as $c_0(Ca^{2+})$.

$$c_{bound}(Ca^{2+}) = c_0(Ca^{2+}) - c_{free}(Ca^{2+}) \tag{26}$$

To calculate IAPs it is important to know the concentrations of both ions involved in the reaction. For this purpose the ratio of calcium to carbonate binding is assumed to be 1:1 thus the bound concentration of carbonate ions is expressed as:[106]

$$c_{bound}(CO_3^{2-}) = c_{bound}(Ca^{2+}) \tag{27}$$

And the free concentration of carbonate ions is expressed as:

$$c_{free}(CO_3^{2-}) = [c_{added}(NaHCO_3) - c_{bound}(Ca^{2+})] \cdot \beta_2 \tag{28}$$

With β_2, the molar ratio of carbonate to bicarbonate at a given constant pH. With these assumptions the (IP) and the solubility product can be calculated:

$$IP = c_{free}(CO_3^{2-}) \cdot c_{free}(Ca^{2+}) \tag{29}$$

And the ion activity product (IAP) as:

$$IAP = c_{free}(CO_3^{2-}) \cdot \gamma_{CO_3} \cdot c_{free}(Ca^{2+}) \cdot \gamma_{Ca} \tag{30}$$

After precipitation, the IAP can be treated as the solubility product (SP) of the resulting phase. It is assumed that $\gamma_{CO_3} = \gamma_{Ca}$ which is possible because the two ion radii are similar.[105] Thereby the thermodynamic solubility product of the resulting precipitate is obtained.

3.6.2 Data from sodium hydroxide addition

Due to the low change in Ca^{2+} concentration in the $CO_3^{2-} \rightarrow Ca^{2+}$ titration (*cf.* chapter 3.3; start: [$CaCl_2$] = 10 mM; nucleation: [$CaCl_2$] = 9.3 mM) and a logarithmic dependence between calcium concentrations and potentials, the noise of the ISE is large when compared to the all-over potential change, as opposed to the $Ca^{2+} \rightarrow CO_3^{2-}$ titration, where the concentration increased over several orders of magnitude considering the low detection limit of the ISE, which is in the range of $5 \cdot 10^{-7}$ M (start: [$CaCl_2$] = 0.0 mM nucleation: [$CaCl_2$] = 0.1 mM).[107] Therefore, the amounts of bound and free calcium ions were calculated from the NaOH data based on a 1:1 binding ratio of calcium and carbonate ions.[36] In addition, bicarbonate binding can be neglected at this pH as only 0.7% of the total calcium binding is due to bicarbonate ions (comparing the ion pairing constants for calcium with bicarbonate ions and carbonate ions, which are 12,7 M^{-1} and 1674 M^{-1}, respectively).[108-109] The error made here is lower than the accuracy of the measurement.[52, 106, 109] A comparison of the binding data obtained from the ISE (calcium) and from the NaOH titration (carbonate) is shown in Figure 6. Indeed, it is obvious that the NaOH titration shows the same trend (*cf.* Figure 6 red line) as the ISE measurement (black line) but with a better signal to noise ratio.

The amount of bound carbonate ($n_{bound}(CO_3^{2-})$) was calculated according to the following equation:[36]

$$n_{bound}(CO_3^{2-}) = n_{added}(NaOH) \cdot \frac{1}{2 \cdot \beta_2(CO_3^{2-}) + \beta_1(HCO_3^-)} \tag{31}$$

Where $n_{added}(NaOH)$ is the amount of added sodium hydroxide required to maintain a constant pH level, and β_2 is the molar fraction of carbonate and β_1 is the molar fraction of bicarbonate at any given pH. All other values required for the determination of solubility products can be calculated by use of the following equations:

$$c_{bound}(CO_3^{2-}) = c_{bound}(Ca^{2+}) = \frac{n_{bound}(CO_3^{2-})}{V} \tag{32}$$

Here $c_{bound}(CO_3^{2-})$ is the concentration of the bound carbonate ions, $c_{bound}(Ca^{2+})$ the concentration of bound calcium ions and V the total volume in the reaction system.

$$c_{free}(Ca^{2+}) = c_0(Ca^{2+}) - c_{bound}(Ca^{2+}) \tag{33}$$

Here $c_0(Ca^{2+})$ is the Ca^{2+} concentration at the beginning of the experiment.

$$c_{free}(CO_3^{2-}) = [c_{added}(NaHCO_3) - c_{bound}(Ca^{2+})] \cdot \beta_2 \tag{34}$$

With equations 33 and 34 the concentration-based ion product (IP) can be calculated by a multiplication of the free concentrations of calcium and carbonate ions.

The reproducibility and a comparison of the two calculation ways, one based on the NaOH data and the other on the ISE data, can be found exemplary in the Appendix (Figure 42 & Figure 43) in which the two ways of calculation yield consistent results. The error from the Ca-ISE data is by far higher than the one resulting from the NaOH titration data (*cf.* Figure 6) due to the reasons outlined above.

The calcium carbonate ion pairing constant $K_{cluster}$ was calculated for the pre-nucleation regime according to the law of mass action,[110]

$$Ca^{2+}{}_{aq} + CO_3^{2-}{}_{aq} \xleftrightarrow{K_{cluster}} CaCO_{3\,cluster} \tag{35}$$

The concentration of the PNCs is equal to the concentration of bound carbonate ions and so $K_{cluster}$ can be calculated (see Figure 13 A).[111]

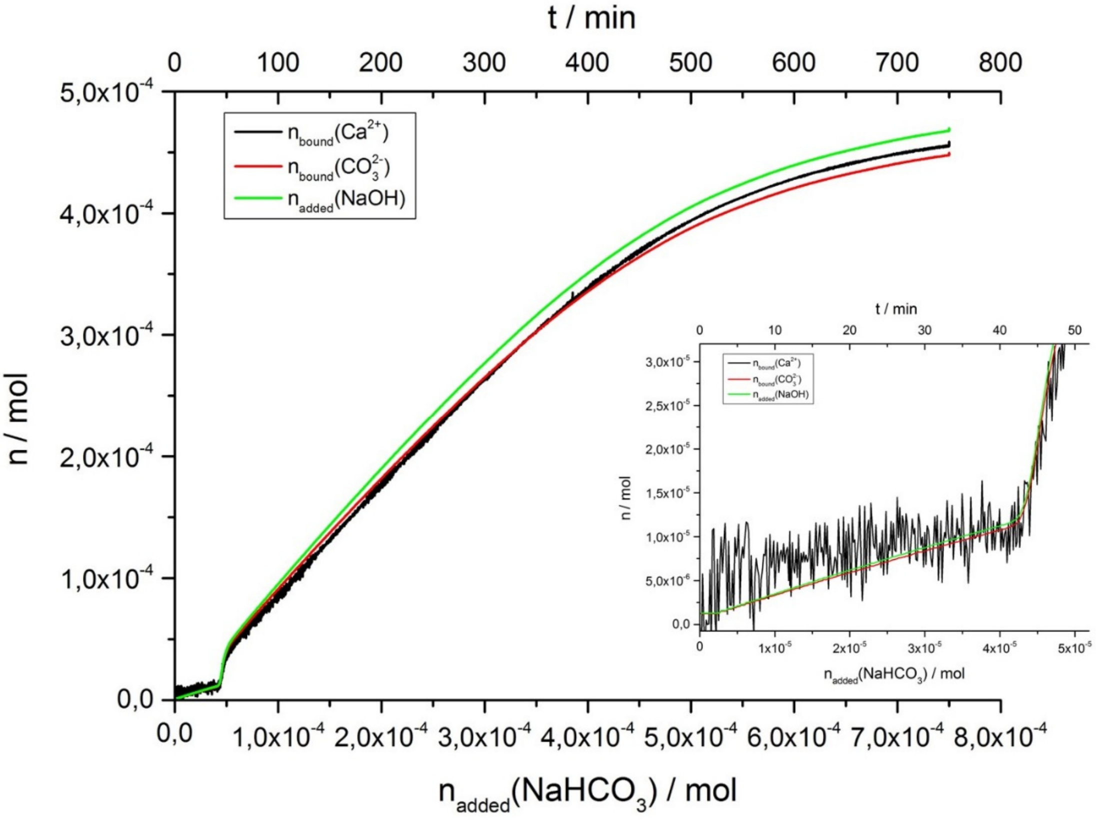

Figure 6 | Amount of bound Ca^{2+} (from ISE data, black) and bound CO_3^{2-} ions (from the NaOH data, red) and the added amount of sodium hydroxide (green) vs time. Inset zoom in into the prenucleation regime.

3.7 THz Spectroscopy Experiments

The experiments for the THz absorption spectroscopy measurements were carried out as follows: 25 mL of a 10 mM sodium bicarbonate solution at pH 9 or pH 10 were filled in a 50 ml glass beaker. At a constant rate of 0.01 mL/min a 10 mM $CaCl_2$ solution was added to the buffer while the pH was kept constant utilizing a 10 mM NaOH solution. For the experiments with polycarboxylates as additives, which were only performed at pH = 9, the addition rate was kept at 0.01 mL/min but the concentration of the $CaCl_2$ and of the NaOH solutions was increased to 100 mM. For the THz absorption spectroscopy experiments 1.5 mL of the reaction solution were drawn by a pipette at different stages of $CaCl_2$ addition (*cf.* Figure 8) and directly placed in the THz absorption spectrometer.

For the THz-TD spectroscopy experiments the samples were prepared differently than for the THz absorption spectroscopy experiments, namely by mixing the solutions with a syringe pump. Therefore, aqueous solutions of calcium carbonate were prepared from carbonate buffers, which were prepared by adding 10 mM sodium carbonate solution into 10 mM sodium bicarbonate solution (pH 8.50) until the pH of the resulting carbonate buffer was set to either pH 9.00 or pH 10.0. In order to maintain a constant pH, addition of 10 mM aqueous NaOH solution is required when calcium solution is added to these buffers. Thus, the calcium carbonate solutions were prepared by adding 10 mM $CaCl_2$ and NaOH solutions into 25 mL carbonate buffer at pH 9.00 or pH 10.0, under constant stirring, according to the volumes compiled in Table 1. $CaCl_2$ and NaOH solutions have been added at a rate of 15 μL min^{-1} each. Under continuous stirring, local high concentrations and nucleation of calcium carbonate was prevented. Calcium chloride solution was added first, and then the NaOH solution. The buffer solutions as well as all calcium carbonate solutions were prepared freshly on the day of the respective experiment. For THz-TDS analyses 70 µl of the distinct sampling stages were drawn from the calcium carbonate solutions and measured immediately.

Table 1 Preparation scheme for 10 mM calcium carbonate solutions at pH 9.00 and pH 10.0 for THz time-domain measurements.

V(10 mM carbonate buffer) / mL	pH	V(10 mM $CaCl_2$) / µL	V(10 mM NaOH) / µL
25	9	150	75
25	9	300	150
25	9	450	225
25	9	600	300
25	9	750	375
25	9	1200	1000

25	10	100	150
25	10	200	300
25	10	300	450
25	10	400	600
25	10	500	750
25	10	600	1200

THz narrow-band absorption measurements were performed at the Ruhr-Universität Bochum with a tabletop p-Ge THz laser spectrometer[112-113]. The experiments were performed and evaluated by Dr. F. Sebastiani and Dr. B. Born. For further details see literature and ref [114].

3.8 Titration experiments with additives

The data shown in chapter 6 are produced as follows and in accordance with the calculation described in chapter 3.6. All experiments were repeated at least in triplicate and generally showed a very good reproducibility. In brief, 10 mM calcium chloride solution was dosed at a constant rate of 100 µL/min, or 10 µl/min, as indicated, into 50 mL of 10 mM sodium bi/carbonate buffer at pH 9.75. The pH level was maintained constant by means of automatic counter-titration employing 100 mM NaOH, whereas the concentration of free calcium ions was monitored utilising an ion selective electrode. This experiment is the reference scenario. For experiments with additives, magnesium chloride and/or poly(aspartic acid) (PAsp, 1200-1800 g/mol) were added to the calcium solution with concentrations as indicated (50 mM Mg^{2+}; 25 mM Mg^{2+} + 5µg/mL PAsp; 10 µg/mL PAsp). The Ca^{2+}-ISE was calibrated by dosing the respective solutions into pure water (with corresponding Ca/Mg concentrations where applicable, but without PAsp), also see section 3.5. The very low concentrations of the polyelectrolyte lead to insignificant complexation of calcium ions,[74, 76] whereas both polymer and ion concentrations are sufficiently low to prevent polymer salting out. Note, that any measured ion concentrations reported herein are strictly speaking ion activities, however, owing to rather dilute solutions, any systematic errors resulting from our simplifying procedure only slightly exceed typical experimental errors, which are explicitly demonstrated elsewhere.[110]

3.9 Isolation and characterisation of mineral precursors

Mineral precursors were isolated from the titration assay experimentation at different points by a quench in excess ethanol (see ref.[53] for details). In brief, the complete $CaCO_3$ reaction mixtures were poured into 1 L of ethanol followed by stirring and sedimentation of the precipitate. Afterwards the precipitate was centrifuged, washed, and dried. The resulting powder was analysed by FT-IR, TGA and SEM. For TEM analyses, samples were drawn from the ethanolic solution and 10 µl droplets were blotted on the TEM grid and were dried in air.

FT-IR spectra were recorded utilizing a Perkin Elmer spectrometer 100 equipped with a diamond ATR crystal. TEM was carried out with an in-column OMEGA filter microscope (Zeiss Libra 120) operated at 120 kV. TGA measurements were performed under oxygen atmosphere with a heating rate of 10 K/min using an STA 449 F3 Jupiter instrument. The SEM pictures and EDX analyses were performed utilising a Hitachi TM 3000 microscope.

3.10 Preparation of the AFM substrates and Precursor solutions

All used chemicals where of analytical grade and used without further purification. The growth solutions were prepared by adding 0.1 ml of a 0.01 M NaOH solution to 5 ml of a 0.01 M solution of calcium chloride. Afterwards a volume of 0.06 ml of a 1 mg/ml PAA (M = 1200 g/mol) was added to the solution under stirring. Finally, 0.2 ml of a 10 mM $NaHCO_3$ solution was added to the reaction mixture. Note that the solution is still clear and shows no precipitate.

In situ AFM experiments were carried out at the Universidad de Santiago de Chile. The *in-situ* AFM experiments were performed by L. Caballero and myself and evaluated by L. Caballero and Prof. Dr. F. Melo. For further details check the literature in ref [115].

3.11 Materials

Sodium hydroxide solution (0.1 M), sodium (bi)carbonate and magnesium chloride hexahydrate powder were purchased from Merck. 1 M calcium chloride solution was provided by Fluka and sodium chloride was received from VWR-Chemicals. Poly(acrylic acid) (MW 5100 g/mol) by Aldrich and poly(L-aspartic acid) (MW 5750 g/mol) was received from Alamanda Polymers. Poly(L-aspartic acid) (MW 1200 g/mol -1800 g/mol) was provided by Bayer. For the preparation of all solutions, milliQ water was used to dissolve or dilute the different chemicals, which were all of analytical grade and were used without further purification.

4. The Locus of the Liquid-Liquid Binodal Limit in Aqueous Calcium Carbonate Solutions[2]

While water molecules play a key role during the formation of PNCs,[111] no information about water dynamics are available so far. To evaluate the role of water molecules during the nucleation of calcium carbonate, THz absorption and THz-TD experiments were performed. The dielectric response of samples prepared by subsequent mixing of $CaCl_2$, NaOH and sodium (bi)carbonate buffer solutions were analysed by a relaxation model in the frequency region 0.2–1.4 THz (6.7–46.7 cm^{-1}) using THz time domain spectroscopy (THz-TDS) (*cf.* chapter 3.7). From the measured time-domain data $E_{THz}(t)$, a fast Fourier transformation was applied to obtain the frequency-dependent power and phase of the transmitted pulse. Subsequently, the frequency-dependent absorption coefficient $\alpha(\nu)$ (power attenuation), index of refraction $n(\nu)$ (delay of the THz pulse) as well as complex dielectric constant $\hat{\varepsilon}(\nu) = \varepsilon'(\nu) - \varepsilon''(\nu)$ were deduced.[116]

The data was fitted into a double Debye model. It is well known to describe dielectric relaxation of aqueous samples, yielding the complex dielectric response:[117]

$$\varepsilon(\omega) = \varepsilon'(\omega) - i\varepsilon''(\omega) = \varepsilon_\infty + \frac{\Delta\varepsilon_1}{1-i\omega\tau_1} + \frac{\Delta\varepsilon_2}{1-i\omega\tau_2} \quad , \qquad (36)$$

where τ_i is the time constant for the i^{th} relaxation mode, ω is the frequency, ε' (Figure 7 A) and ε'' (Figure 7 B) is the real and imaginary part of the complex dielectric constant, respectively, and ε_∞ is the dielectric constant in the high frequency limit.

---

[2] Parts of this chapter are published in *Angew. Chem. Int Ed* **2017**, 56, 490-495. For the sake of readability not all passages cited from the published manuscript are marked with quotation marks (“ ”) additionally. Figures taken from these publications are also not marked additionally.

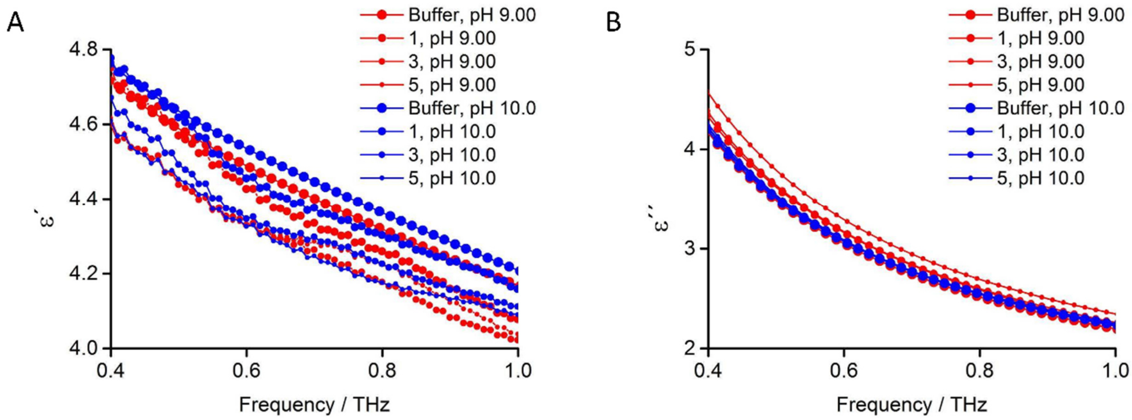

Figure 7 | A) This plot shows the real part of the dielectric constant ε´ of the THz time domain data at pH 9.0 (red) and at pH 10.0 (blue). B) Plotted is the imaginary part of the dielectric constant ε´´ of the THz time domain data at pH 9.0 (red) and at pH 10.0 (blue). The quoted volumes can be contrasted with the stages of precipitation in Figure 9.

The slower time constant τ_1 is associated with a cooperative reorientation of an ensemble of molecules (~8 ps for pure water) whereas the faster one, τ_2, emanates from hydrogen bond formation and dissociation (~200 fs for pure water).[118-121] The fitted parameters of the complex dielectric constant, using the double Debye model are summarized in Table 2. The fast relaxation (τ_2) indicating hydrogen bond formation is found to be nearly unaffected by the different stages of precipitation at both pH values, while the slower one (τ_1) indicative of slower reorientation processes, shows significant changes (Table 2). In Figure 8, the change of τ_1 at different nucleation stages is displayed. For pH 10.0, a change in τ_1 is observed at the pre-nucleation stage, when τ_1 decreases compared to the stages before (Figure 8 B).

Table 2 Fitted parameters of the complex dielectric constant to the THz time domain data using a double Debye model. The standard deviation (SD) of five independent measurements is shown. * Experimental data;^ Data from ref. [117]

pH	*Sampling stage (ml)*	ε_∞	ε_s	ε_2	τ_1 *(ps)*	*SD(τ_1) (ps)*	τ_2 *(ps)*	*SD(τ_2) (ps)*
	bulk water*	3.11	78.3	4.64	7.68	0.17	0.11	0.022
	bulk water^	5.37	78.3	3.39	8.75	0.60	0.21	0.055
9.00	0.0	3.20	78.3	4.63	7.73	0.32	0.115	0.040
9.00	0.15	3.31	78.3	4.65	7.49	0.15	0.141	0.025
9.00	0.30	3.28	78.3	4.53	7.04	0.24	0.116	0.032
9.00	0.45	3.05	78.3	4.45	7.31	0.16	0.109	0.021

9.00	0.60	3.06	78.3	4.40	6.96	0.15	0.105	0.020
9.00	0.75	2.91	78.3	4.40	6.92	0.13	0.092	0.0178
9.00	1.2	3.35	78.3	4.46	6.58	0.19	0.133	0.022
10.0	0.0	3.15	78.3	4.67	7.71	0.14	0.111	0.020
10.0	0.1	3.18	78.3	4.64	7.77	0.25	0.117	0.028
10.0	0.2	2.86	78.3	4.53	7.78	0.08	0.093	0.017
10.0	0.3	2.88	78.3	4.48	7.59	0.16	0.095	0.018
10.0	0.4	3.02	78.3	4.56	7.50	0.10	0.101	0.015
10.0	0.5	2.90	78.3	4.42	7.49	0.12	0.093	0.017
10.0	0.6	2.88	78.3	4.39	7.35	0.05	0.089	0.011

At pH 9.00, τ_1 decreases significantly upon addition of $CaCl_2$ solution. The decrease of τ_1 shows a perturbation of the cooperative relaxation of the hydrogen bond network, similar to what has been observed for confined water in organic solvent. [122] In reverse micelles, for example, the decrease of τ_1 is correlated with a decreasing size of the micelle, and is thereby indicative of the retardation of water dynamics due to confinement and interfacial hydrogen bonding. Also, τ_2 was found to be affected less.[123]

The THz-TDS data was complemented by THz narrow-band absorption measurements (see Experimental section 3.7) in the frequency range of 2.1-2.8 THz (~70–95 cm^{-1}), which are dominated by collective water hydrogen-bond network dynamics.[124] Distinct solution stages were prepared by continuous and slow addition of dilute calcium chloride solution into carbonate buffer at constant pH, and identified via the determination of the developing calcium carbonate IAP utilizing a calcium ion-selective electrode (stages of undersaturated pre-nucleation, supersaturated pre-nucleation, and early post-nucleation, i.e. Regimes I, II & III in Figure 9 A or B, respectively).

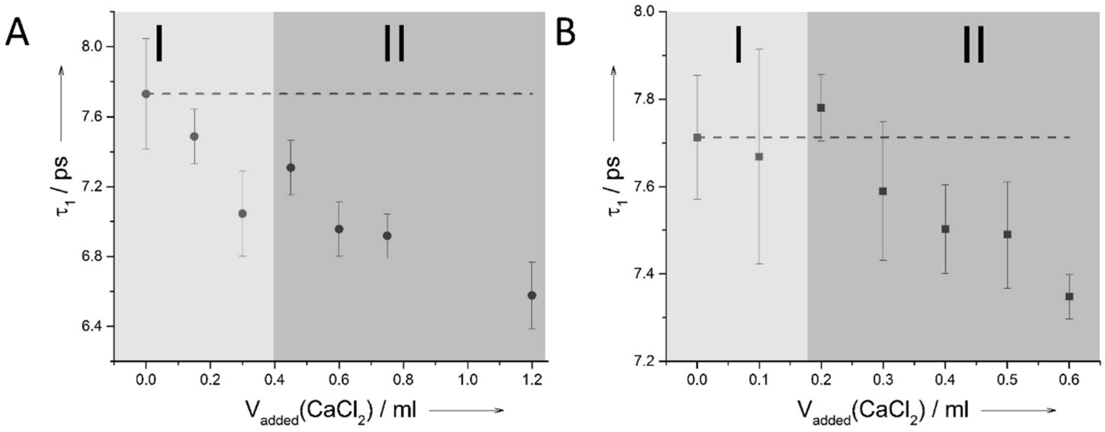

Figure 8 | Relaxation time constant (τ_1) obtained from a fit of experimental data to the double Debye model describing the complex dielectric constant at pH 9.0 (black circles, A) and at pH 10.0 (black squares, B) and of the buffer (black dashed line). The error bars represent the standard deviations of five independent measurements. The calcium chloride volumes can be contrasted with the stages of precipitation in Figure 9

The corresponding developments at a constant pH of 9.00 (Figure 9 A) and pH 10.0 (Figure 9 B) are similar, whereas the THz effects at pH 9.00 are larger than at pH 10.0 due to the larger fraction of carbonate ions in the buffer. Below the level of saturation relating to proto-calcite ACC[53] (Region I in Figure 9 C) until roughly the ACC-saturation threshold, the THz response increases linearly above the level of bulk water dynamics. Afterwards, it drops to a plateau at both pH 9.00 (Figure 9 C) and pH 10.0 (Figure 9 D), i.e. as soon as the aqueous calcium carbonate system becomes supersaturated with respect to the distinct proto-structured ACCs (Regime II).[55] The activity-based solubility product for proto-calcite and proto-vaterite ACC of $3.1 \cdot 10^{-8}$ M² and $3.8 \cdot 10^{-8}$ M² for pH 9.00 and pH 10.0, all respectively, was determined as described in the experimental section (*cf.* chapter 3.6.1),[110] and is in accordance with the literature within experimental accuracy.

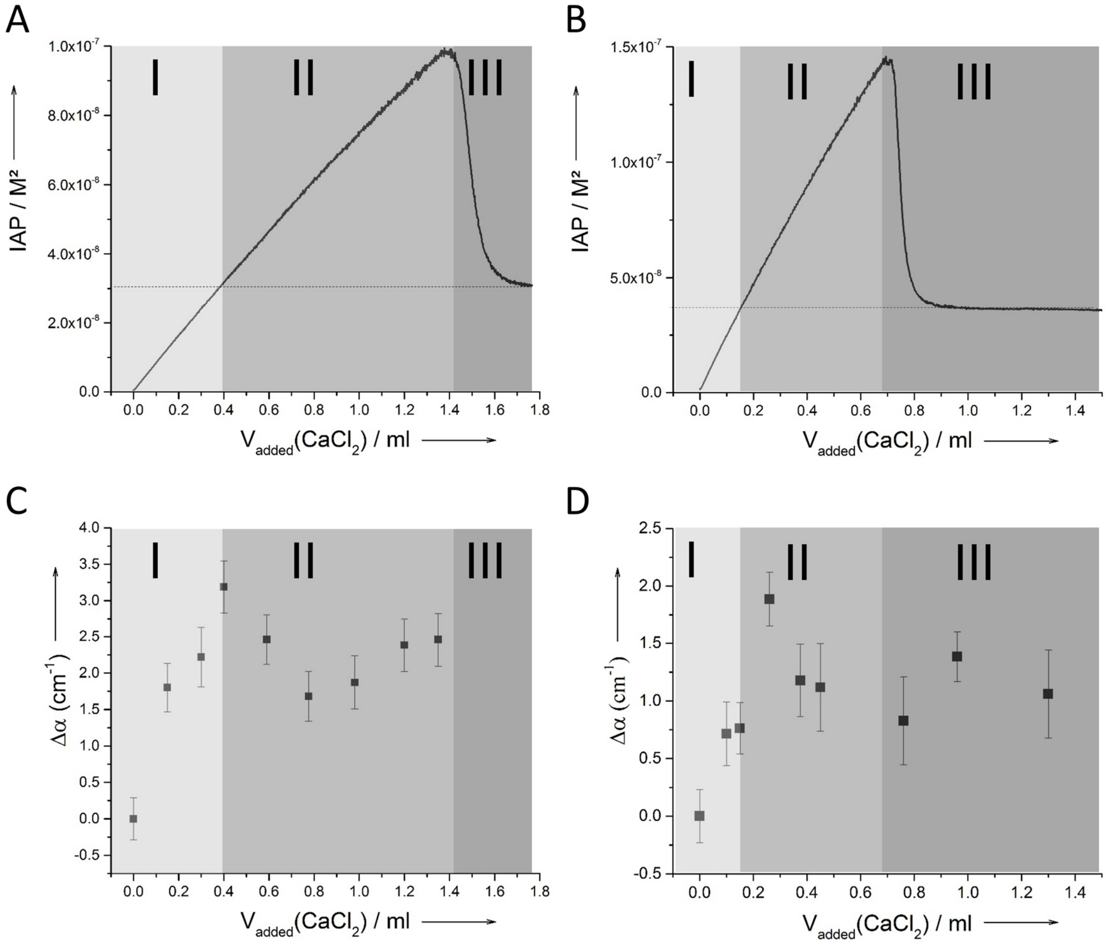

Figure 9 | Titration data at pH 9.0 (A) and pH 10 (B) together with THz-absorption in the frequency range of 2.1-2.8 THz without additives at pH 9.00 (C) and pH 10 (D); the concentration of the added calcium solution was 10 mM. The horizontal dashed line in A and B represents the solubility threshold of pc-ACC and pv-ACC, respectively. Error bars represent +/- 1-σ-standard deviation of N = 4 single measurements. The different regimes (I-III) correspond to the different nucleation regimes during the titration representing undersaturated (I) saturated (II) and nucleated (III).

Regarding the increase of the absorption at 2.1–2.8 THz in the pre-nucleation stage (under-saturated with respect to proto-calcite ACC; Regime I, Figure 9 A, B), it must be noted that the corresponding increase in the IAP (Figure 9 A, B) is deceptive. Upon addition of calcium solution into the carbonate buffer at constant pH, the total ion concentration during the pre-nucleation stage (i.e. regimes I & II) stays virtually constant at ca. $2.0 \cdot 10^{-2}$ M, increasing by only $4.8 \cdot 10^{-5}$ M upon entering Regime II (i.e. after addition of ca. 0.4 mL $CaCl_2$ solution, Figure 10). At the same point, the free calcium concentration has increased from initially zero to $7.3 \cdot 10^{-5}$ M. The corresponding increase in THz absorption thus cannot be attributed to the increasing calcium ion concentration. In fact, Funkner *et al.* observed a linear THz absorption change in the order of 70 cm^{-1} M^{-1} with respect to the $CaCl_2$ concentration and assigned to rattling modes of anions and cations within their hydration cages.[125] Here, the corresponding change would be less than 0.01 cm^{-1} due to the low investigated concentrations.

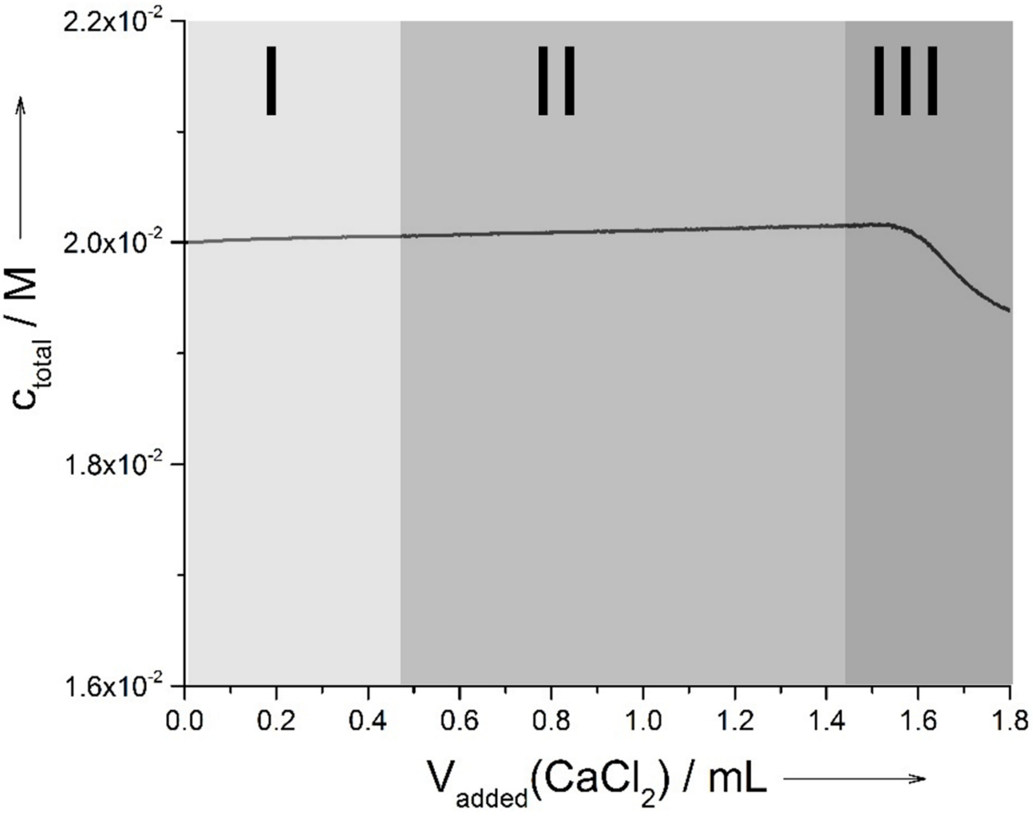

Figure 10 | Development of the total ion concentration during the early stages of the titration experiment without additives at pH 9.0.

The absorption of carbonate buffer solution was also recorded and compared to water ($\Delta\alpha = 0.6 \pm 0.2$ cm^{-1}). Thus, the reason for the increase in THz absorption remains unclear, but it can be speculated that it is due to $CaCO_3$ pre-nucleation cluster formation. Also, the nonlinear subsequent response as soon as Regime II is entered (Figure 9 C and Figure 9 D, for pH 9.00 and pH 10.0, respectively), cannot be attributed to any single ion contribution.[125] Both THz-TDS and THz narrow band absorption data sets provide strong evidence for a structural and dynamical transition in the aqueous calcium carbonate system, occurring at an IAP corresponding to the solubility product of the proto-structured ACCs, within experimental accuracy. This occurs upon entering Regime II, long before the drop of the IAP in Regime III (Figure 9 A, B) that indicates the formation of a solid calcium carbonate phase. All absorption changes are more typical for the formation of neutral species rather than highly charged ionic complexes, which would give rise to more dramatic differences in the absorption, $\Delta\alpha$.[125-128] More importantly, the observation of the turnover in THz absorption is not due to induction times associated with the formation of solid $CaCO_3$. Experiments where the addition of $CaCl_2$ was stopped at defined IAPs show that the induction time after the addition of 0.8 mL $CaCl_2$ (10 mM, minimum in Figure 9 C see also Figure 11) still exceeds 60 minutes; however, the sample drawn from the titration assay after 1.0 mL has likely nucleated solid CaCO3 during the THz analysis (THz absorption measurements last about 1 h; Figure 11). As the distinct change of the THz absorption spectroscopy cannot be attributed to already nucleated $CaCO_3$ species, the change in water dynamics must be related to the locus of the liquid-liquid binodal, where water dynamics are slowed down again due to a confinement as water is "bound" in nanodroplets, the second liquid phase. The fact that the binodal limit lies directly at the solubility product of proto structured ACC strongly suggests that proto structured ACCs form *via* solidification of the second liquid phase, after the liquid-liquid binodal is crossed.

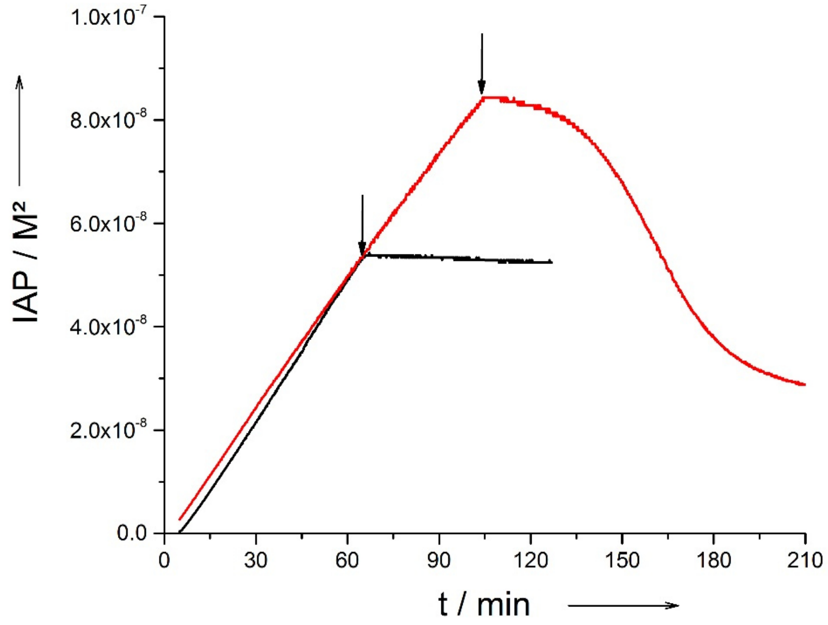

Figure 11 | Stop experiments after the addition of 0.6 ml (black curve) and 1.0 ml (red curve) of 10mM $CaCl_2$ solution to the additive-free system Black arrows mark the time point at which the addition of $CaCl_2$ was stopped.

In order to provide evidence for the locus of the liquid-liquid binodal limit, independent of investigations based on THz spectroscopy, $Ca^{2+}\rightarrow CO_3^{2-}$ titration experiments being stopped at different ion products were performed (IPs, Figure 12). It can be recognised that at high levels of ion products (note, that these are not IAP for further explanation see chapter 3.5 and ref. [110]), e.g., $IP = 1.6\cdot10^{-7}$ M², at which the induction time can be expected to be short, ACC is formed directly ($IP_{ACC} = 3.5\ 10^{-8}$ M² see Figure 12). At lower supersaturations, however, a longer induction time and the direct formation of vaterite is observed ($IP_{Vat} = 1.4\ 10^{-8}$ M²). Both solubility values are in accord with the literature within experimental error (literature value for vaterite: IP_{vat}=1.7 10^{-8} M²).[36, 129] If the IP or the IAP does not exceed the ACC solubility threshold, and with it, the liquid-liquid binodal limit, no precipitation is observed within times up to 16 hours (Figure 12 black curve). This is evidence that the liquid-liquid miscibility gap has to be entered to enable the formation of solid calcium carbonate, however, it does not show whether crystals can be formed directly, or whether ACC has not to be present as an intermediate as speculated recently.[130] This question will be addressed later in this chapter.

The influence of the ionic excess on the nucleation pathway was explored; as it is well known that transient liquid precursors like PILPs are preferably formed at low pH values, in which bicarbonate ions were suggested to play a key role, or in an excess of Ca^{2+} ions.[52] To further explore the latter effect, we performed $CO_3^{2-}\rightarrow Ca^{2+}$ titration experiments. Figure 13 compares the evolution of IPs between the $CO_3^{2-}\rightarrow Ca^{2+}$ titration and the $Ca^{2+}\rightarrow CO_3^{2-}$ titration. In the pre-nucleation regime, a linear increase in IPs can be observed in both cases (Figure 13 A, B). The slope of the $CO_3^{2-}\rightarrow Ca^{2+}$ titration is steeper than in the *vice versa* case. Note, if bicarbonate ions would play a significant role in this binding equilibrium, more calcium ions would be bound, which would result in an even flatter slope. Also, activity effects do not play a role, as they have been accounted for by calibration (*cf.* chapter 3.5). The calculated values for the ion pairing constant in the $Ca^{2+}\rightarrow CO_3^{2-}$ titration are $K^{Ca}_{cluster} = 2210.3 \pm 14$ M^{-1} and for the $CO_3^{2-}\rightarrow Ca^{2+}$ titration $K^{CO3}_{cluster} = 1001.5 \pm 30$ M^{-1} (Figure 13, A). While the first value is in accordance with literature, the value for the $CO_3^{2-}\rightarrow Ca^{2+}$ titration is slightly lower, as the literature values cover a range from 1258 M^{-1} to 30199 M^{-1}.[129] A difference of bound calcium and carbonate ions in PNCs can be observed (cf. Figure 14). This is supported by a lower value for $K_{cluster}$ for the $CO_3^{2-}\rightarrow Ca^{2+}$ titration. In this case, a lower amount of bound calcium and carbonate ions leads to a delayed nucleation as indicated by a later drop in the IP (Figure 13 B).

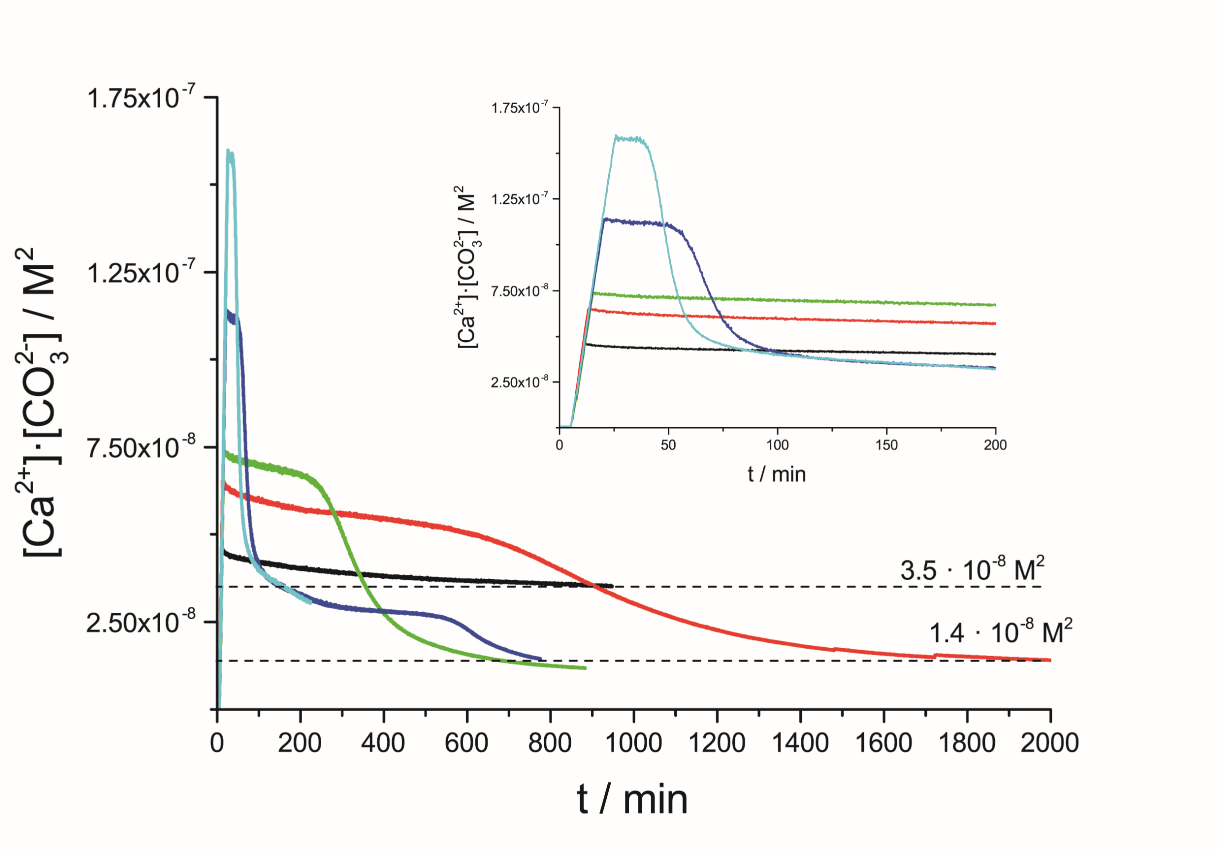

Figure 12 | Ca^{2+}→CO_3^{2-} titration curves where the addition of the calcium solution was stopped after 0.6 mL (black), 0.8 mL (red), 1.0 mL (green), 1.5 mL (blue) and 2.0 mL (cyan blue), but the measurement of the calcium ion potential and the pH titration was continued.

The same effect was observed in previous work, where an increasing ionic strength leads to a progressively reduced calcium carbonate ion association, delaying nucleation, despite a formally higher level of supersaturation.[110] It implies that the actual level of supersaturation, calculated based on the free ions, is not relevant for the quantitative assessment of phase separation, but rather the amount of ions bound in PNCs. In the CO_3^{2-}→Ca^{2+} titration, more titrant – in this case carbonate buffer – has to be added to the system to bind enough ions in PNCs to nucleate a solid phase (cf. Figure 14) due to the reduced association constant.

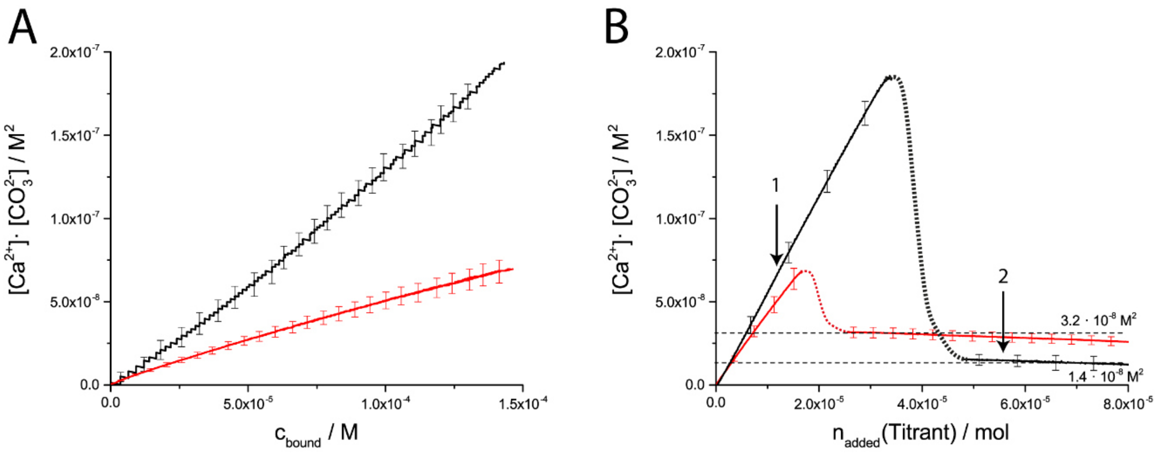

Figure 13 | Comparison of the titrations the $Ca^{2+}\rightarrow CO_3^{2-}$ (red) and $CO_3^{2-}\rightarrow Ca^{2+}$ (black) experiments; A) comparison of the pre-nuclation binding from which $K_{cluster}$ was calculated as described in the experimental part; B) complete titration curves plotted versus the added titrant (calcium chloride solution for the red and carbonate buffer for the black curve); the arrows indicate the time points where samples for the cryo-TEM investigation were taken. The coloured dashed lines represent the kinetically controlled part of the titration experiments. In this regime a thermodynamic consideration is not possible therefore no error bars are shown here. The black dashed lines represent the solubility product of the precipitated phases.

In contrast, in the $Ca^{2+}\rightarrow CO_3^{2-}$ titration an increased ion association leads to a higher value for $K^{Ca}_{cluster}$. Moreover, in the $CO_3^{2-}\rightarrow Ca^{2+}$ titrations, vaterite is formed directly (IP_{Vat} = 1.4 10^{-8} M^2),[129] without a detectable amorphous intermediate phase (which, however, may be highly transient), as opposed to the $CO_3^{2-}\rightarrow Ca^{2+}$ titration. Such a behaviour can also be observed for the $Ca^{2+}\rightarrow CO_3^{2-}$stop experiments (Figure 12).

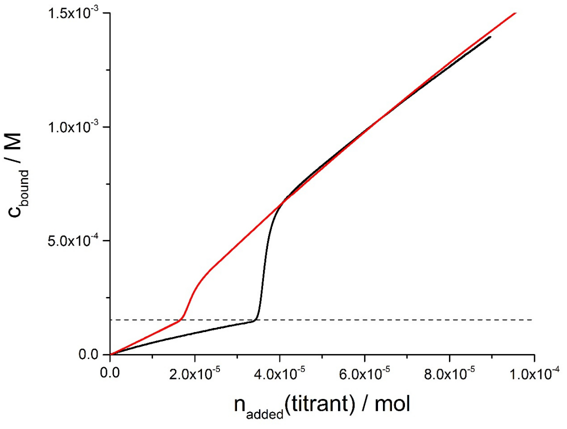

Figure 14 | Amount of bound bicarbonate and bound Ca^{2+} ions in the $CO_3\rightarrow Ca$ titration (black) and in the $Ca\rightarrow CO_3$ titration (red)

From a thermodynamic viewpoint, ACC can be formed in both cases, because the level of supersaturation is sufficient (cf. Figure 12 & Figure 13). Thus, a straightforward explanation for this observation cannot be given based upon the notions of CNT. In order to shed further light onto this question, we performed additional titrations; in accordance with previous work by Kellermeier *et al.* employing $Ca^{2+} \rightarrow CO_3^{2-}$ titrations, the nucleation time depends on ionic strength,[110] also in the $CO_3^{2-} \rightarrow Ca^{2+}$ experiment (Figure 15).[110]

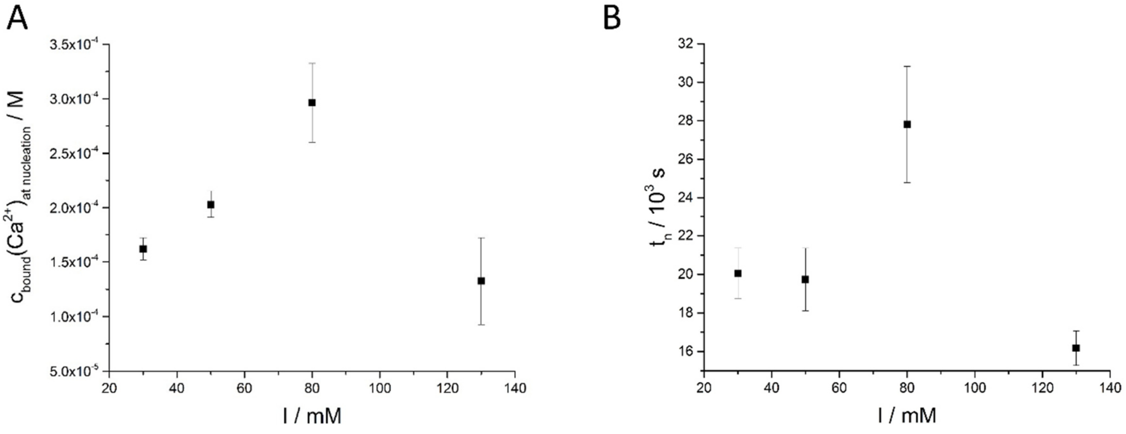

Figure 15 | Plot of the ionic strength applied in the $CO_3^{2-} \rightarrow Ca^{2+}$ titrations versus the concentration of bound of Ca at nucleation (A) and the time at which nucleation occurs (B).

However, in the $CO_3^{2-} \rightarrow Ca^{2+}$ titrations, nucleation is only delayed at moderate ionic strengths, but promoted at high ionic strengths (130 mM). The delay of nucleation in the $CO_3^{2-} \rightarrow Ca^{2+}$ experiments can be explained by activity effects as outlined above.[110] The promotion of nucleation can be understood within the notions of the PNC pathway. Due to the higher charge of calcium ions compared to bicarbonate ions, the liquid droplets may carry a higher charge density then in the $Ca^{2+} \rightarrow CO_3^{2-}$ titrations. This could lead to a stronger electrostatic stabilization of the nano-droplets compared to nano-droplets in the $Ca^{2+} \rightarrow CO_3^{2-}$ titrations. By an increase of ionic strength the colloidal stabilization of droplets is lowered due to a screened coulomb potential so that repulsive forces downsize. Therefore, it can be speculated that the colloidal stabilization of the nano-droplets drop at high ionic strength and therefore nucleation is promoted in the $CO_3^{2-} \rightarrow Ca^{2+}$ titrations at high ionic strength. However, it was impossible to show this by means of zeta potential measurements, probably owing to the very small size of the droplets. In any case, this effect may be interpreted as the opposite scenario discussed for the colloidal stabilization of PNCs by silica.[131]

To investigate whether crystals form directly in the different settings, cryo-TEM measurements were performed. In the Ca^{2+}→CO_3^{2-} titrations, the formation of a solid amorphous phase is detected by the ISE in the post-nucleation stage, and indeed, ACC particles with a diameter of ca. 20 nm can be observed in the cryo-TEM images (Figure 16 A).

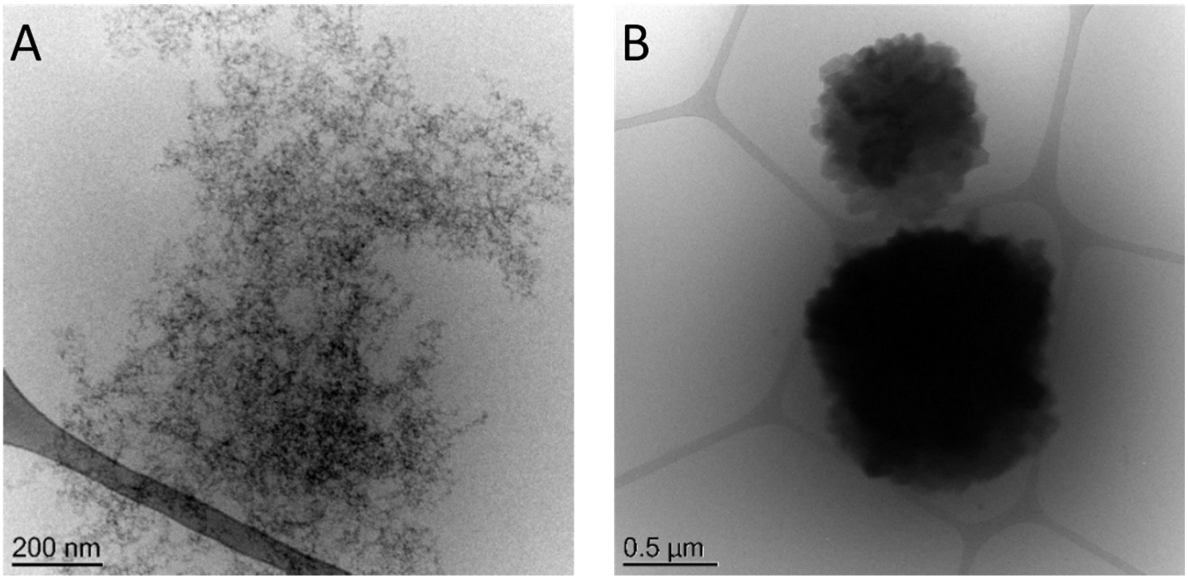

Figure 16 | Cryo-TEM pictures of samples drawn at arrow 2 (Figure 13 B) for the Ca^{2+}→CO_3^{2} titration.

At the same time, also vaterite crystals can be observed (Figure 16 B) but the ISE detects the more soluble phase (pc-ACC) as expected.

From CO_3^{2-}→Ca^{2+} titrations, samples were drawn at time points indicated by arrows in Figure 13. In the pre-nucleation regime (Figure 13 arrow 1) extended networks of aggregated nanoscopic species can be observed as shown in Figure 17 and in Figure 18 A. These structures likely represent a phase-separated dense liquid. The micrographs for the pre-nucleation regime show denser parts indicated by a higher contrast surrounded by less dense structures, which is likely a hint towards a solidification of the second liquid phase as the liquid-liquid binodal is already crossed at this point.

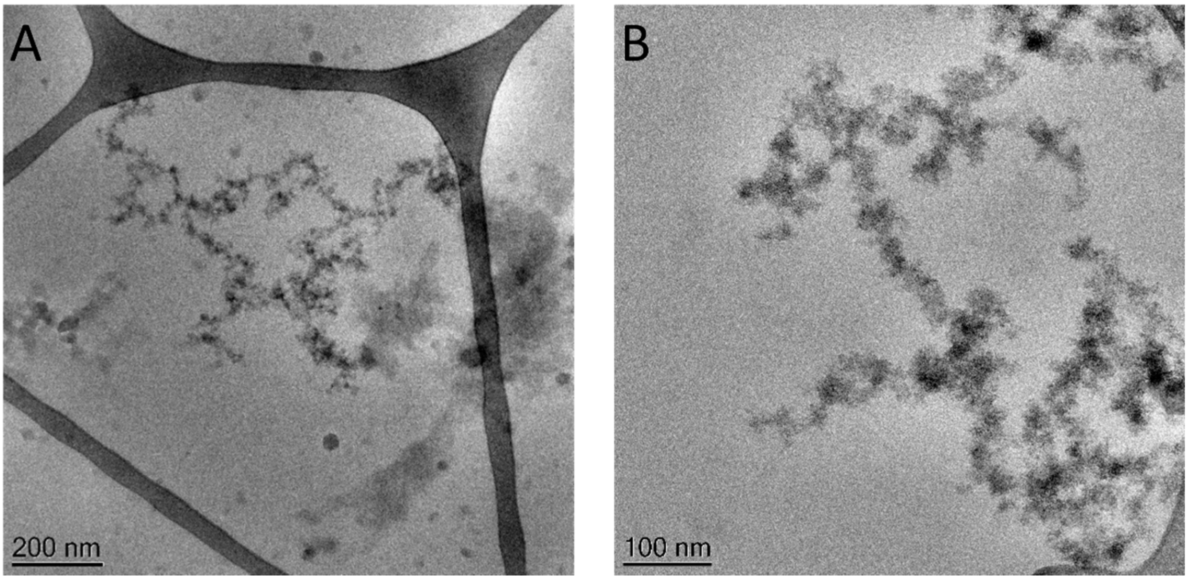

Figure 17 | Cryo-TEM pictures of samples drawn at arrow 1 see Figure 13 B for the CO_3^{2-}→Ca^{2+} titration

The results for the post-nucleation time point (arrow 2 in Figure 13) are shown in Figure 18 B. Here, again, amorphous particles as suggested by the ED with a diameter of ~50 nm can be observed (Figure 18 B). As the particles exhibit a contrast variation, it can be assumed that a less dense layer surrounds them. This layer can be interpreted as the second liquid phase, which is not completely solidified compared to the particles with a higher contrast. The particles in the post-nucleation regime seem to have a smoother structure compared to the pre-nucleation stage, as they show no grain structures on the lower nanometre scale. Crystalline structures are also present in the post-nucleation regime as shown in Figure 19. This observation contradicts the results from the titration experiment only at first sight, which shows a solubility product that can be assigned to vaterite ($Ks_{Vat} = 1.4\ 10^{-8}\ M^2$). Nevertheless, a *bona fide* amorphous phase is present in the system. This implies that ACC particles are hidden – in a second liquid phase as they are surrounded by a layer with a lower contrast.

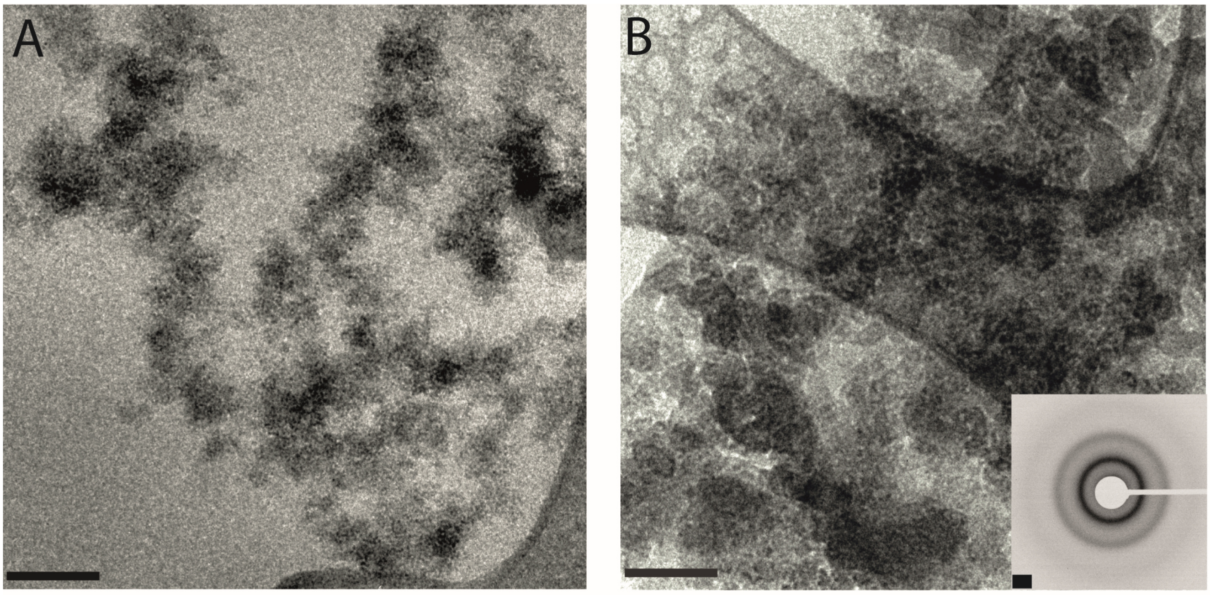

Figure 18 | Cryo-TEM pictures at stage 1 (A) as indicated in figure 2 for the CO_3^{2-}→Ca^{2+} experiment and taken at stage 2 (B). Scale bars are 50 nm in every image and 2 1/nm for the ED inset in B.

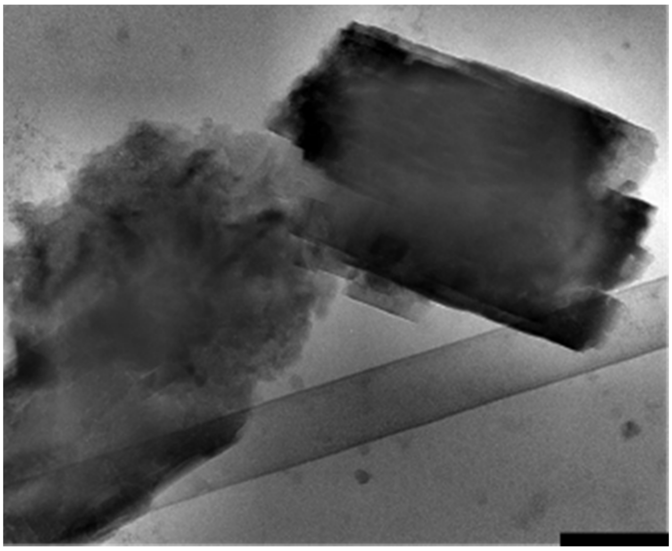

Figure 19 | Cryo-TEM image taken at stage 2 as indicated in figure 2 B for the CO_3^{2-}→Ca^{2+} titration. Scale bar represents 100 nm

5. The Existence Region of Different Amorphous Calcium Carbonates — a Novel Phase Diagram for Aqueous Calcium Carbonate

To determine the phase diagram for the aqueous calcium carbonate system, titration experiments by adding 10 mM $CaCl_2$ solution into 10 mM $NaHCO_3$ buffer at a dosing rate of 0.1 µmol/min at different temperatures and pH values were performed. The regions, which are accessible by this approach, are shown in Figure 20. At the slowest addition rate (0.1 µmol/min) in the titration experiment the $CaCO_3$ system crosses the liquid-liquid binodal border and enters a metastable regime (Figure 20 A), and the solubility of the nucleated ACC quantitatively reflects the locus of the liquid-liquid binodal limit.[114] As it was shown in chapter 4 the liquid-liquid binodal has to be crossed for a homogeneous nucleation of solid calcium carbonate.

With faster addition rates (e.g. 10.0 µmol/min), a wider area of metastable regions can be approached (Figure 20). Therefore, the existence regime for ACCs nucleated via liquid-liquid phase separation can be determined. To explore where the border between ACCs formed via binodal and spinodal demixing occurs direct mixing experiments were performed to access the unstable region as shown schematically in Figure 20.

In Figure 21, titration experiments at different addition rates (black curve corresponds to an addition rate of 0.1 µmol/min, red 1.0 µmol/min, and green 10.0 µmol/min) at pH 9.0 and different temperatures are shown. The linear increase in the pre-nucleation regime is due to the constant addition of calcium ions to the carbonate buffer. In this stage, PNCs are formed and the added amount of calcium ions is higher than the detected value, because calcium and carbonate ions are bound in PNCs.[36] In the pre-nucleation regime, differences in the slope for all addition rates are negligible. Therefore, the cluster equilibrium is not affected by the addition rate and hence, the pre-nucleation slope of the curve characterizes the thermodynamic equilibrium of calcium carbonate ion association. The ion activity product (IAP) evolves linearly until solid calcium carbonate is formed. In the post-nucleation regime, the solubility product of the precipitated ACC is detected. The solubility product is directly linked to the stability of the formed phase due to the connection between the solubility products K_{sp} and the Gibbs free energy ($\Delta G = -RT \ln K_{sp}$). As the ISE only detects the most soluble phase in the system (as mentioned above), the final stable phase is most likely already present shortly after nucleation, but the solubility is governed by the most soluble phase, which is the kinetic product under these conditions.

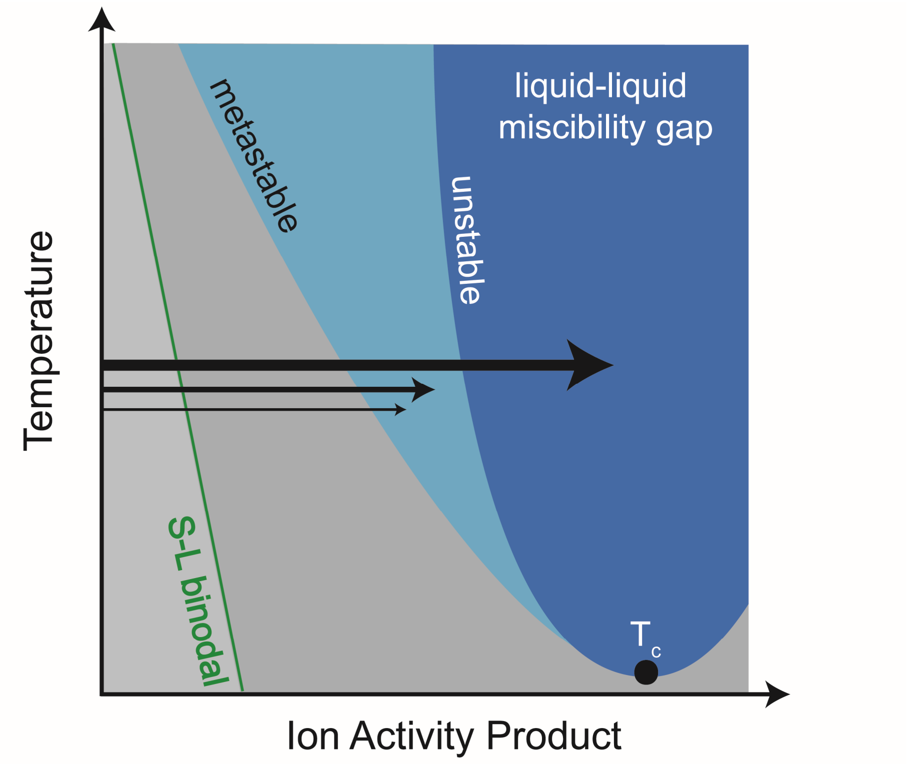

Figure 20 | Schematic representation of the regions accessed by the rate-dependent titration experiments. The slowest addition rate crosses the liquid-liquid binodal line and enters the metastable regime (smallest arrow). Faster addition rates enable exploring the range of the metastable regime(middle fat arrow) By a direct mixing of calcium chloride and sodium carbonate solutions, the spinodal region can be accessed by entering the unstable region by an even faster "addition" (bold arrow). The width of the arrow symbolizes the addition rate, the temperature offset serves for a better representation. S-L binodal represents the solid-liquid binodal of calcite in the $CaCO_3$ system as the system is stable before this limit is crossed; the light blue area represents a metastable state after the liquid-liquid binodal is crossed; the dark blue area is the unstable regime in the liquid-liquid regime and is excessed after the liquid-liquid spinodal is crossed.

The black curves in Figure 21 were obtained from titrations at the slowest addition rate of 0.1 µmol/min at pH 9.0, which leads to pc-ACC with an IAP = $3.2 \cdot 10^{-8}$ M² at 25°C. At a faster addition rate of 1.0 µmol/min (Figure 21 A red curve) the solubility product of the initially precipitated phase is higher. By further increasing the addition rate to 10 µmol/min, an even more soluble phase is formed after nucleation (Figure 21 A green curve). The same trend can be found for all investigated temperatures (Figure 21 A 15°C, B 25°C, C 35°C, D 45°C). Figure 22 shows the rate and temperature dependency of titration experiments at pH=10.0, in which similar trends as for pH 9.0 can be noted. The precipitated phase at pH 10 has always a higher solubility product than the one precipitated at pH 9.0. This effect was observed before by Gebauer *et al.* for the case of pc- and pv-ACCs, where pv-ACC has a higher solubility product compared to pc-ACC.[25]

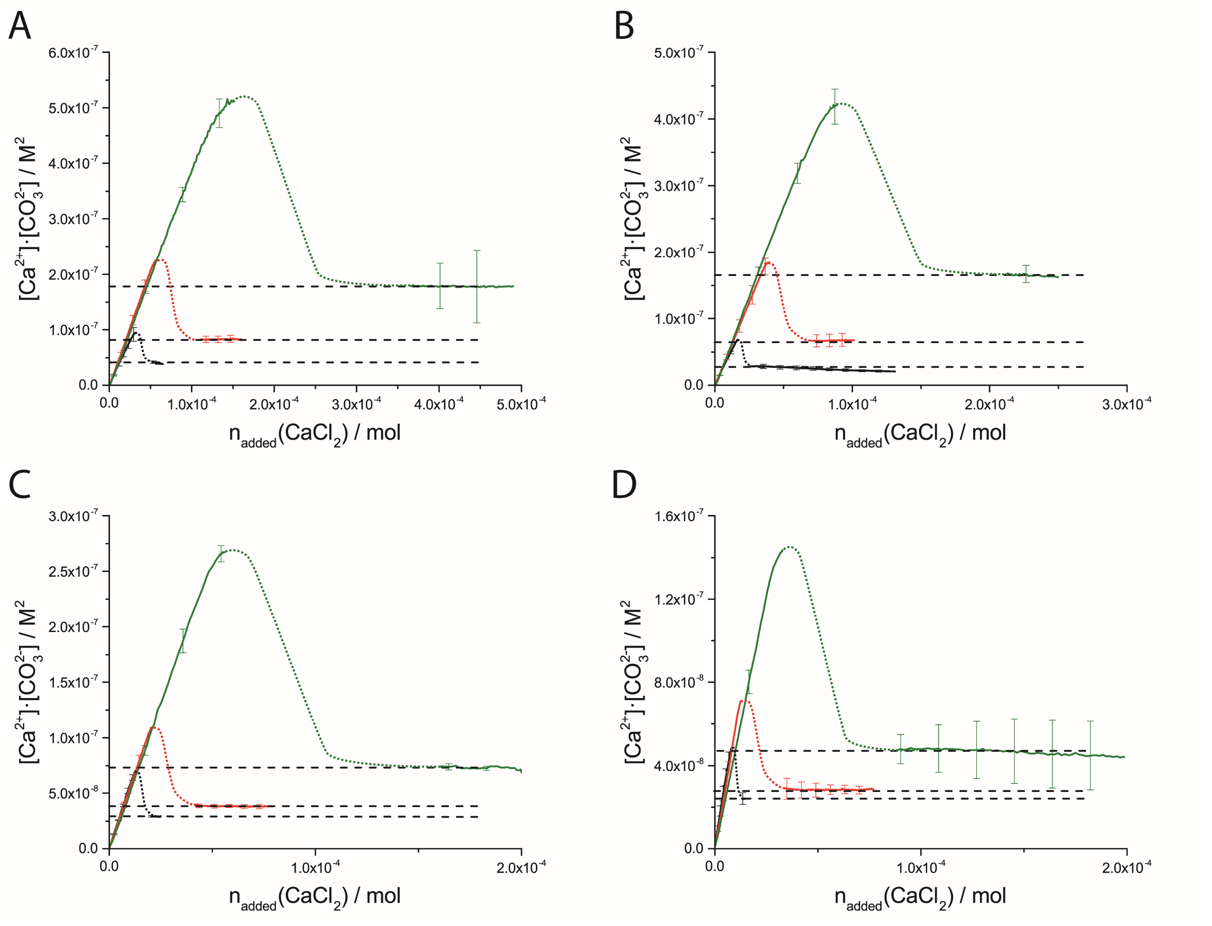

Figure 21 | Titration curves obtained from measurements at pH 9.0 at different temperatures (A 15°C, B 25°C, C 35°C, D 45°C) and for different addition rates (black 0.1 µmol/min; red 1.0 µmol/min; green 10 µmol/min). The y-axis shows the IAP of the precipitated phase. The coloured dashed lines are guidelines for the eyes because this part of the curve is dominated by kinetics the different measurements cannot be averaged. The black dashed lines directly give the solubility product of the precipitated phase.

From a thermodynamic viewpoint, the supersaturation level is high enough to access the proto structured ACCs as well as vaterite and all other crystalline polymorphs, and the observations made in the titration experiments are difficult to understand without the presence of a liquid-

liquid miscibility gap, and a pathway of ACC formation via solidification of liquid precursors as described in chapter 4. The supersaturation referenced to the precipitated solid phase ($S = IAP_{max}/IAP_{nuc}$) is in the range of about 2-3 for most of the addition rates and temperatures (exceptions: pH = 10.0, v = 10 µmol/min T = 35°C and T = 45°C; *cf.* Table 3 to Table 8). This observation is a hint that the probability of a solidification is sufficient under these conditions. It could be explained because a higher IAP in the second liquid phase leads to a more metastable liquid phase, which is directly linked with less stable phase after solidification of the liquid droplets.

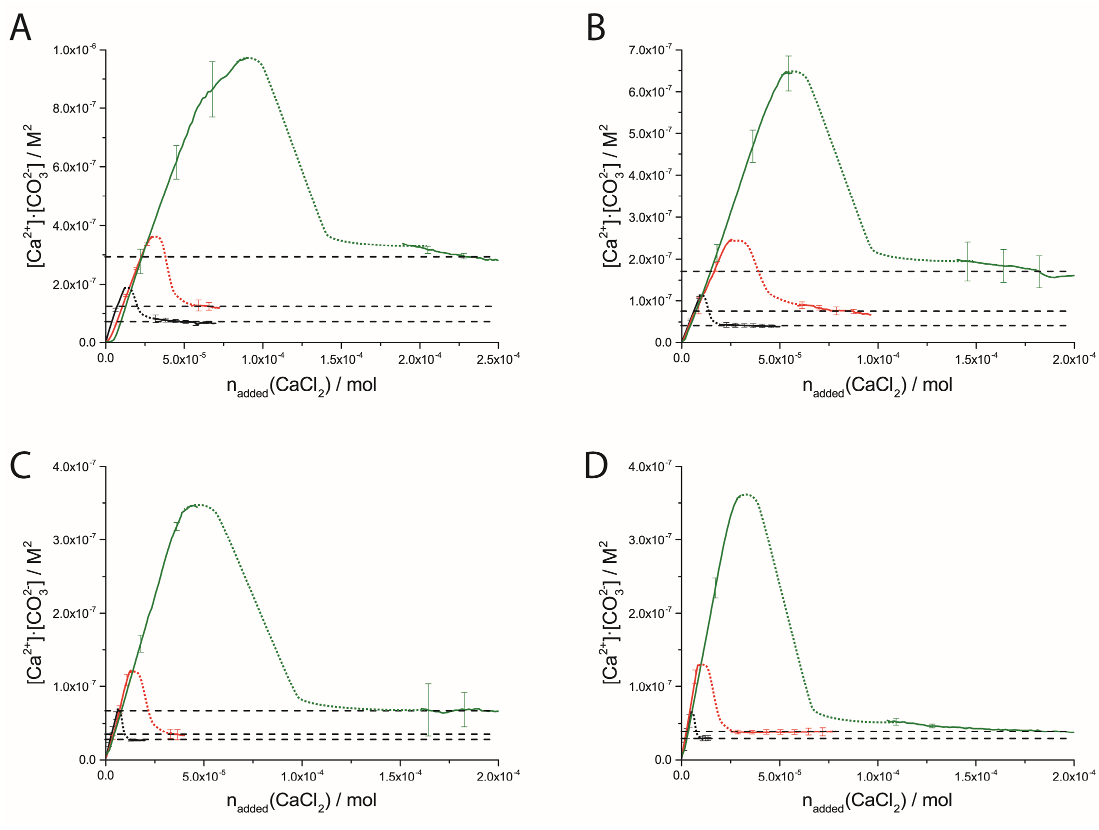

Figure 22 | Titration curves obtained from measurements at pH 10.0 at different temperatures (A 15°C, B 25°C, C 35°C, D 45°C) and for different addition rates (black 0.1 µmol/min; red 1.0 µmol/min; green 10 µmol/min). The y-axis shows the IAP of the precipitated phase. The coloured dashed lines are guidelines for the eyes because this part of the curve is dominated by kinetics the different measurements cannot be averaged. The black dashed lines directly give the solubility product of the precipitated phase.

The fact that higher addition rates lead to ACCs that are more soluble can be interpreted by solidification of the second liquid phase. As faster addition rates allow accessing the metastable regime deeper and deeper (Figure 20), the IAP of the second liquid phase and of the mother solution gets higher and therefore become more metastable. A more metastable phase may have a higher probability of solidification. Therefore, ACC formed *via* solidification of the second liquid phase also gets less stable, which results in a higher solubility product after precipitation. The solid phase formed from these less stable precursors leads to less stable ACCs as indicated by a higher solubility product after nucleation.

To investigate the origin of the different stabilities of nucleated ACCs, ATR-FTIR spectra were recorded. Figure 23 shows ATR-FTIR spectra obtained for the fastest addition rate of 10 µmol/min and for the slowest 0.1 µmol/min after quenching the solutions after the liquid-liquid nucleation event, but before solidification. Interestingly the structural order is not affected by the addition rate. This can be observed as there are no differences in the ν_1 and ν_3 stretching modes of the ACCs (Figure 23) The only difference between the two ACCs can be recognized around 3700 cm^{-1} – 3000 cm^{-1} where the water band is more pronounced for the less stable ACC (*cf.* Figure 23 red curve). A Recent study by Farhadi *et al.* showed that the temperature has no influence on pc-ACC (for this reason no temperature dependent ATR-FTIR spectra are shown).[56]

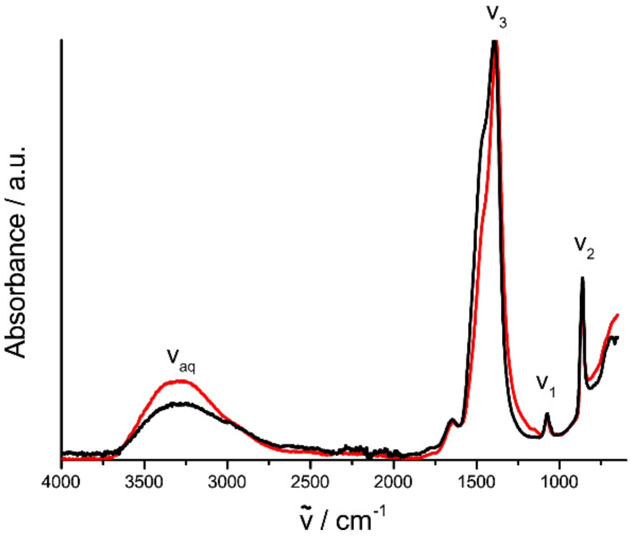

Figure 23 | ATR-FTIR spectra obtained from quenched ACCs before nucleation for an addition rate of 10 µmol/min (red) and for 0.1 µmol/min (black). The vibrational modes of carbonate ions (ν_1, ν_2, and ν_3) and water molecules (ν_{aq}) are indicated in the figure.

To investigate the kinetic stability of the different, initially precipitated amorphous calcium carbonates, titration stop experiments were performed. Figure 24 shows the results of such stop experiments at pH 9.0 and different temperatures (A 15°C, B 25°C, D 45°C). Interestingly, at faster addition rates (10 µmol/min) as soon as the addition is stopped the ion activity products drop immediately to values slightly lower than the solubility of proto-structured ACCs but not to a solubility related to the least stable anhydrous crystalline form (vaterite). This behavior applies to all temperatures (*cf.* Figure 24). The measurements underpin that the initially precipitated phases are transient intermediates towards a hydrated crystalline structure like monohydrocalcite (IAP of 2.5 10^{-8} M² at 25°C). [132] An IAP between 2.0 10^{-8} M² and 3.0 10^{-8} M² is observed in the titration experiments after the transition supporting the occurrence of monohydrocalcite.

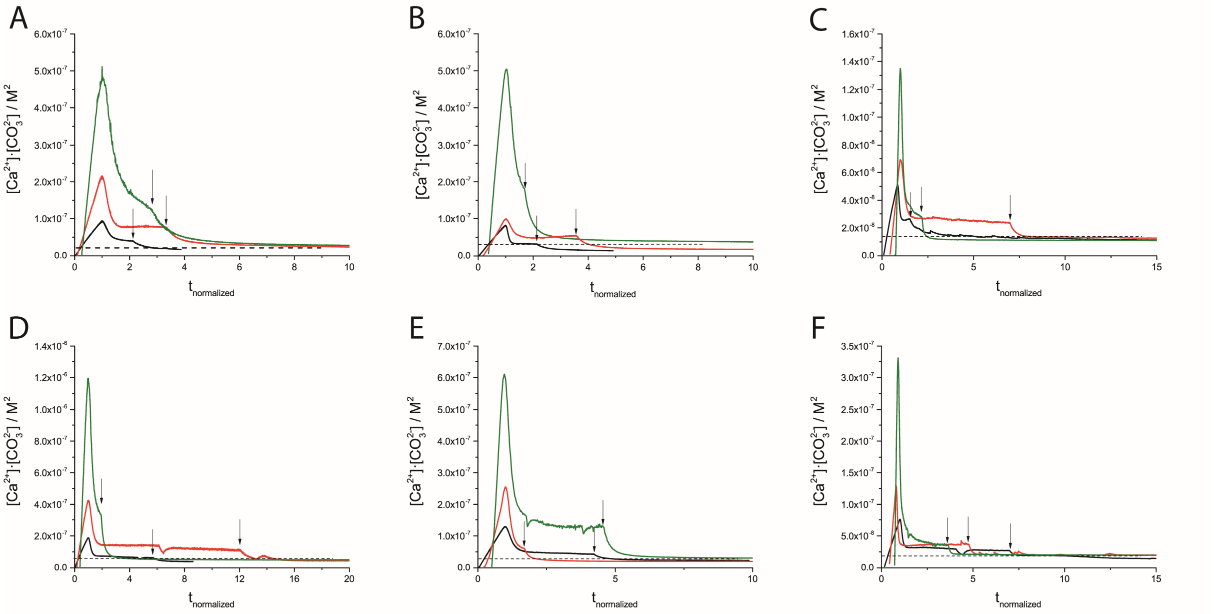

Figure 24 | Titration stop experiments at pH 9.0 (A,B,C) and pH 10.0 (D,E,F) at different temperatures (A & D 15°C, B & E 25°C, C & F 45°C) and pH=9.0 for different addition rates; black 0.1 µmol/min; red 1.0 µmol/min; green 10 µmol/min. The black arrows indicate the points, at which the calcium chloride addition was stopped. The time was normalized to the point of nucleation for the sake of comparability. The kinks in the graphs originated from the thermostat, which induces a voltage to the ISE because it is not running continuously.

To locate the unstable regime of the liquid-liquid miscibility gap we performed direct mixing experiments as described in the literature.[108] In the appendix measured IAPs from direct mixing experiments over time are shown in Figure 45. The experimental procedure can be found in chapter 3.4. It is obvious that the solubility of the ACC formed here is two orders of magnitudes higher than the one obtained from slow addition experiments as they lie in the range of $2{\cdot}10^{-6}$ at 25°C.

In Figure 25, titration experiments at different temperatures and pH values are compared. As it can be seen from this figure, at pH 9.0 and pH 10.0 the slope in the pre-nucleation regime is dependent on the temperature, so the pre-nucleation slope varies in these experiments. Therefore, the equilibrium constants for PNCs formation are slightly affected as reported previously (*cf.* Figure 25 A, B ,C).[106] The solubility products of the precipitated phases follow the known rule for calcium carbonate, stating that increasing temperature results in a lower solubility product.[129] A detailed analysis of the pre-nucleation slope and the corresponding energy ($\Delta G_{\mathrm{cluster}}$) values can be found in Figure 26. It can be observed that the values obtained from the measurements presented here are in accord with the literature.[36, 111]. Unfortunately, a clear temperature dependent trend like in the literature cannot be found in these titration experiments. Therefore, an evaluation of the entropic and enthalpic contributions is not possible.

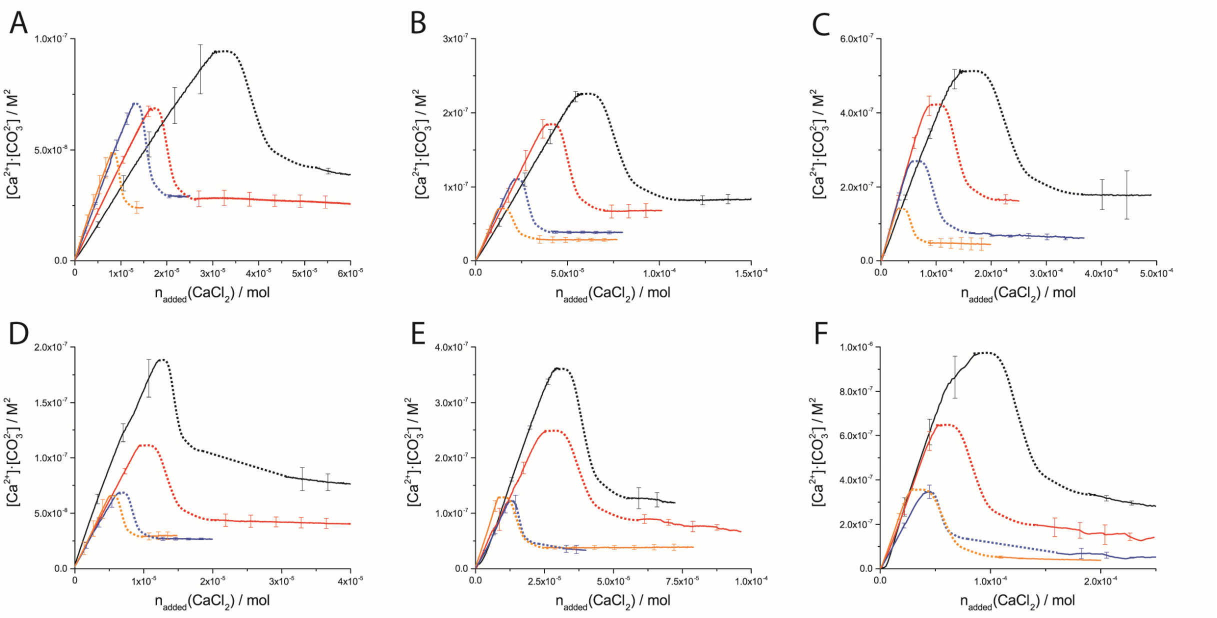

Figure 25 I Temperature dependend titrations (15°C (black) 25°C (red) 35°C (blue) 45°C (orange)) for the different addition rates at pH 9.0 (A 0.1 µmol/min; B 1.0 µmol/min; C 10µmol/min); and for pH 10.0 (D 0.1 µmol/min; E 1.0 µmol/min; F 10µmol/min). The dashed lines are guidlines for the eyes for the part of the curve where kinetic effects overrule thermodynamic contributions.

The results of all the different titration experiments are summarized in the appendix in Table 3-8. A constructed phase diagram for pc- and pv-ACC is shown in Figure 41 in the conclusion.

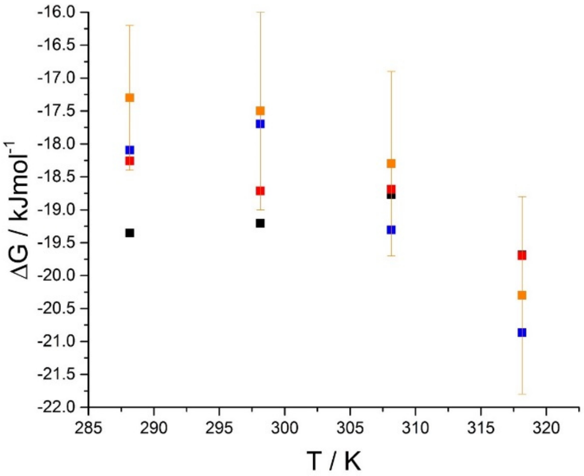

Figure 26 | A plot of free energy vs. the temperature in Kelvin. The black squares originate from 0.1 µmol/min titrations, the red squares originate from 1.0 µmol/min titrations, the blue squares originate from 10 µmol/min titrations, and the orange squares originate from ref.[111]

6. Influence of Additives on the Locus of the Liquid-Liquid Binodal and on the Stability of Nucleated Calcium Carbonate Phases[3]

To reveal whether or not the water dynamics are influenced by polyanions, which play a key role in biomineralization,[15] PAsp and PAA were added to the mineralization experiment. In presence of 5 µg/mL PAsp or PAA at pH 9.00, nucleation of solid calcium carbonate is strongly inhibited (Figure 28 A and B, respectively), in accordance with previous investigations.[74, 76] Note that in order to ensure a similar volume dilution as in the additive-free experiments, the concentration of the calcium chloride solution was increased by a factor of ten ([$CaCl_2$] = 100 mM) in presence of the polymers. There is no detectable THz effect of the polymers owing to their very low concentrations. As mentioned above, an assessment of the induction time shows that even after the addition of 0.6 mL $CaCl_2$ solution (100 mM $CaCl_2$ concentration, Figure 27; *cf.* chapter 4), nucleation of solid $CaCO_3$ does not occur immediately, while the decrease of the IAP – if any – occurs very slowly.

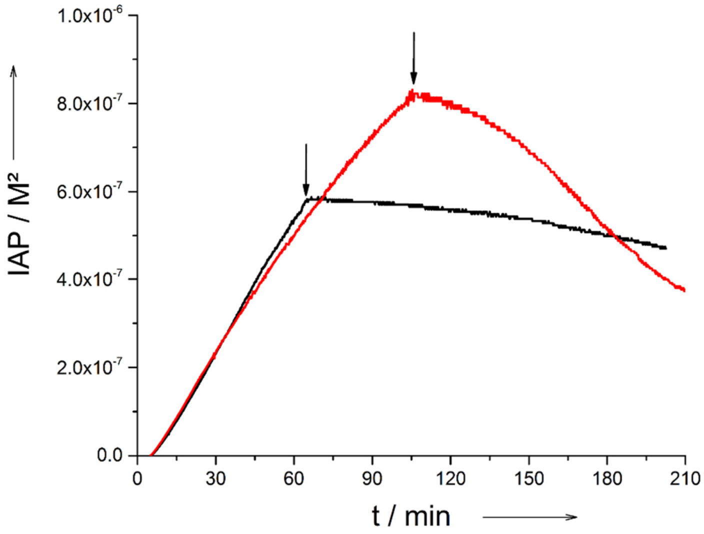

Figure 27 | Stop experiments after the addition of 0.6 ml (black curve) and 1.0 ml (red curve) of 100mM $CaCl_2$ solution to the $CaCO_3$ system with PAA. Black arrows mark the time point at which the addition of $CaCl_2$ was stopped.

---

[3] Parts of this chapter are published in *Angew. Chem. Int Ed,* **2017**, 56, 490-495, and *CrystEngComm* **2015**, 17, 6857-6862. For the sake of readability not all passages assumed from the published manuscript are marked by quotation marks (“ ”) additionally. Figures taken from these publications are also not marked additionally.

However, precipitation of solid $CaCO_3$ likely started during the THz measurements after the addition of 1 mL 100 mM calcium chloride solution in presence of the polymers. Interestingly, in presence of the polyanions, an increase in THz absorption in Regime I was observed, like the additive-free case (*cf.* Figure 9), despite a somewhat more pronounced increase in total ion concentration and a similar increase in the free calcium ion concentration. Reasonably, this arises from cooperative effects like the formation of neutral aggregates of ions, pre-nucleation clusters, and the polyanions.

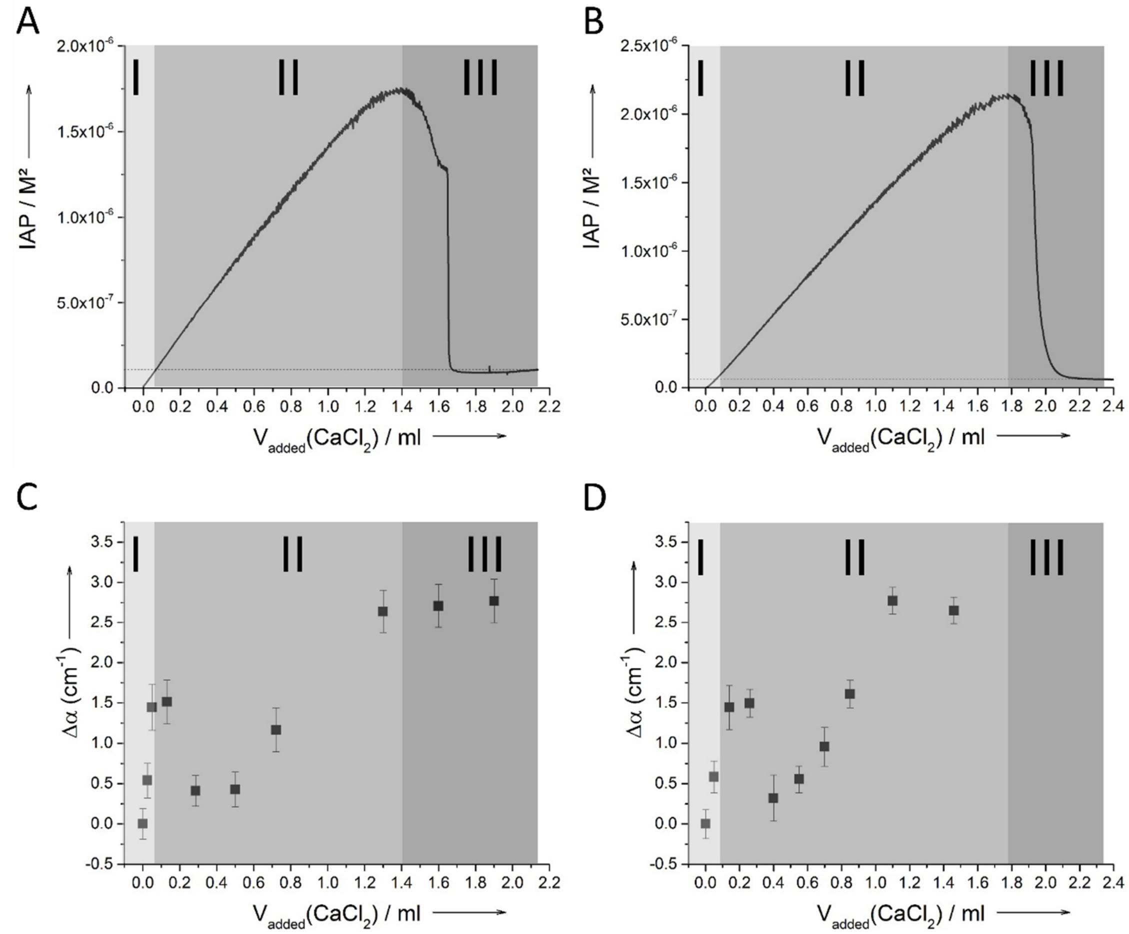

Figure 28 | Titration curve of pAsp (A) and PAA (B) as additive and THz- absorption in the frequency range of 2.1-2.8 THz with 5 µg/ml PAsp (C) and with 5 µg/mL PAA (D) at pH 9.00. The concentration of the added calcium solution was 100 mM. The horizontal dashed line in A represents the solubility threshold of the nucleated ACC phase (~3.9·10-8 M^2, in accordance with pv-ACC within experimental accuracy). Error bars represent +/- 1-σ-standard deviation of N = 4 single measurements.

In the actual titration experiment with 5 µg/mL PAsp (Figure 28 A, see the Figure 28 B for PAA), the initial linear trend of the THz absorption (Figure 28 C, D) is similar to the additive-free case, whereas the features of the curve are somewhat more pronounced. Interestingly, the turnover point in water dynamics is not affected by the presence of the polymer compared to the additive-free experiment (*cf.* Figure 9). This directly implies that the locus of the liquid-liquid binodal is not influenced by these polyanions. The effects of PAA are analogous (Figure 28 D); for both polymers, the nucleation of solid calcium carbonate is strongly inhibited (transition from Regime II to Regime III). Starting from the addition of 1.4 mL $CaCl_2$ solution, we find a plateau, which implies that no further changes with respect to collective modes of the hydrogen bond network occur.

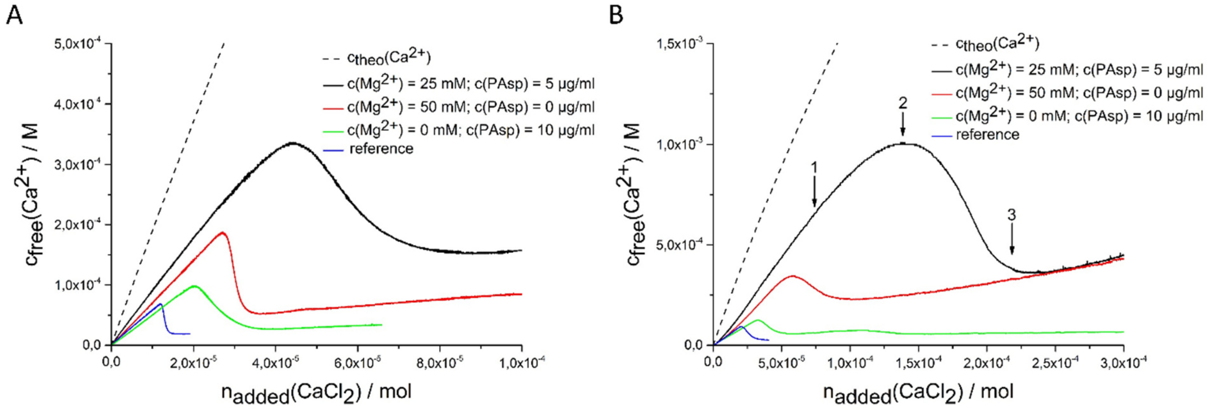

Figure 29 | Development of free calcium concentration upon continuous addition of calcium solution with and without additives (as indicated) into 10 mM carbonate buffer (pH 9.75) at a rate of 0.1 µmol/min (A) and 1.0 µmol/min (B). Note that less calcium is detected than added (c_{theo}) already in the pre-nucleation stage, which can be ascribed to the binding of ions in pre-nucleation clusters. Arrows 1-3 in B indicate states, at which samples were quenched or drawn for additional analyses.

After the locus of the liquid-liquid binodal for $CaCO_3$ system under the influence of polyanions was identified, the effect of two different additives – Mg^{2+} ions and PAsp – on the nucleation process was investigated due to their importance in biomineralization. As already mentioned above, in titration experiments a continuous addition of dilute calcium solution into carbonate buffer at a constant pH of 9.75 leads to a linear increase in the concentration of free calcium ions (Figure 29). Once a critical stage is reached, nucleation occurs, and the concentration of free calcium ions drops to a level that correlates with the solubility of the most soluble phase. Note, the system is not yet in equilibrium according to Gibbs' phase rule and that here not IAPs but free calcium concentrations are shown. The IAP cannot exactly be calculated due to an unknown amount of bound carbonate ions in $MgCO_3$ PNCs.

Typically, the precipitated phase is pv-ACC at this pH level (for the reference experiment without any additives, blue curve in Figure 29; solubility data see chapter 5).[36, 53] The measurements in presence of PAsp (10 µg/mL in the calcium solution; Figure 29, green curve) and magnesium ions (50 mM in the calcium solution; Figure 29, red curve) are consistent with previous investigations (*cf.* Figure 28 and references [74, 76]). Magnesium leads to a moderate inhibition of nucleation, and formation of thermodynamically less stable mixed calcium/magnesium carbonate pre-nucleation clusters [79] (indicated by a steeper slope in the pre-nucleation stage, i.e. a less pronounced binding of calcium ions in the pre-nucleation ion associates, a correspondingly lower equilibrium constant of cluster formation – $K_{cluster}$ cannot be calculated due to the unknown amount of bound carbonate ions in $MgCO_3$ PNCs – and with it, a less negative change in free enthalpy) and of the initially precipitated phase exhibiting a distinctly increased solubility.[79] PAsp, on the other hand, effectively inhibits nucleation already at very low concentrations (10 µg/mL in the calcium solution, which is furthermore considerably diluted upon addition into the carbonate buffer; note that in previous studies reported in the literature, PAsp was added to the carbonate buffer and dilution effects were insignificant).[76]

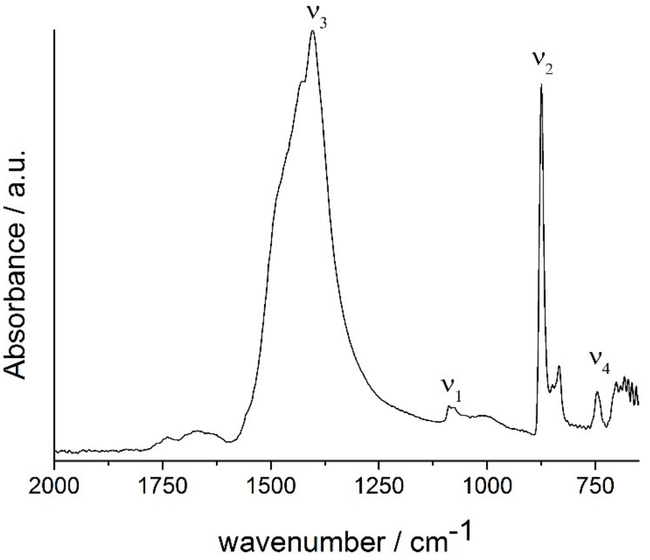

Figure 30 | ATR-FTIR spectrum of a sample obtained with 10 µg/ml PAsp at the end of the titration assay experiment. The bands are consistent with vaterite – (ν_4 = 743 cm^{-1}).

According to Ostwald's rule of stages, a more soluble phase than pv-ACC occurs first (as evident from a higher concentration of free calcium ions) that over time transforms into a more stable form (in this case pv-ACC, solubility data see chapter 5), after nucleation. Nevertheless, vaterite is already present at a certain time after nucleation as indicated by FTIR spectroscopy (Figure 30), however, this does not contradict the higher amount of free calcium ions (as discussed in chapter 4). When magnesium and PAsp are combined in the calcium solution (25 mM Mg^{2+} and 5 µg/mL PAsp), the efficiency towards inhibition of nucleation is significantly increased (Figure 29, black curve). Note that in this experiment with combined additives, the concentrations of PAsp and Mg^{2+} have been reduced in comparison to the individual measurements, to avoid a too high all-over additive concentration. Still, the inhibition of nucleation (apparent from the drop in the free calcium concentration) is far beyond the sum of the individual contributions. Moreover, a new effect arises; the pre-nucleation slope of the calcium concentration development is even steeper. This shows that the mixed calcium-magnesium carbonate pre-nucleation clusters are thermodynamically not as stable as in the experiment where only magnesium as additive is present (Figure 29, red curve, cf. also discussion above). Since electrode calibrations have been carried out with corresponding solutions containing Mg^{2+}, any activity or electrode effects can be ruled out.

The free calcium concentration for the initially precipitated phase is distinctly higher than with PAsp alone, and agrees with the one of the phase formed in presence of Mg^{2+} alone, suggesting a thermodynamic de-stabilisation of the nucleated phase. However, since the composition of this phase may differ from that of the ones precipitated without magnesium (cf. below), this is merely a qualitative assessment. In any case, a link between pre- and post-nucleation speciation (i.e. thermodynamically de-stabilised clusters lead to less stable solid precipitates) is observed — similar as in the case of the pH-dependent switch between proto-calcite ACC and pv-ACC or as described in chapter 5.[36, 53] This effect can also be found when reducing the addition rate of the calcium solution to 0:1 µmol/min (Figure 29 A).

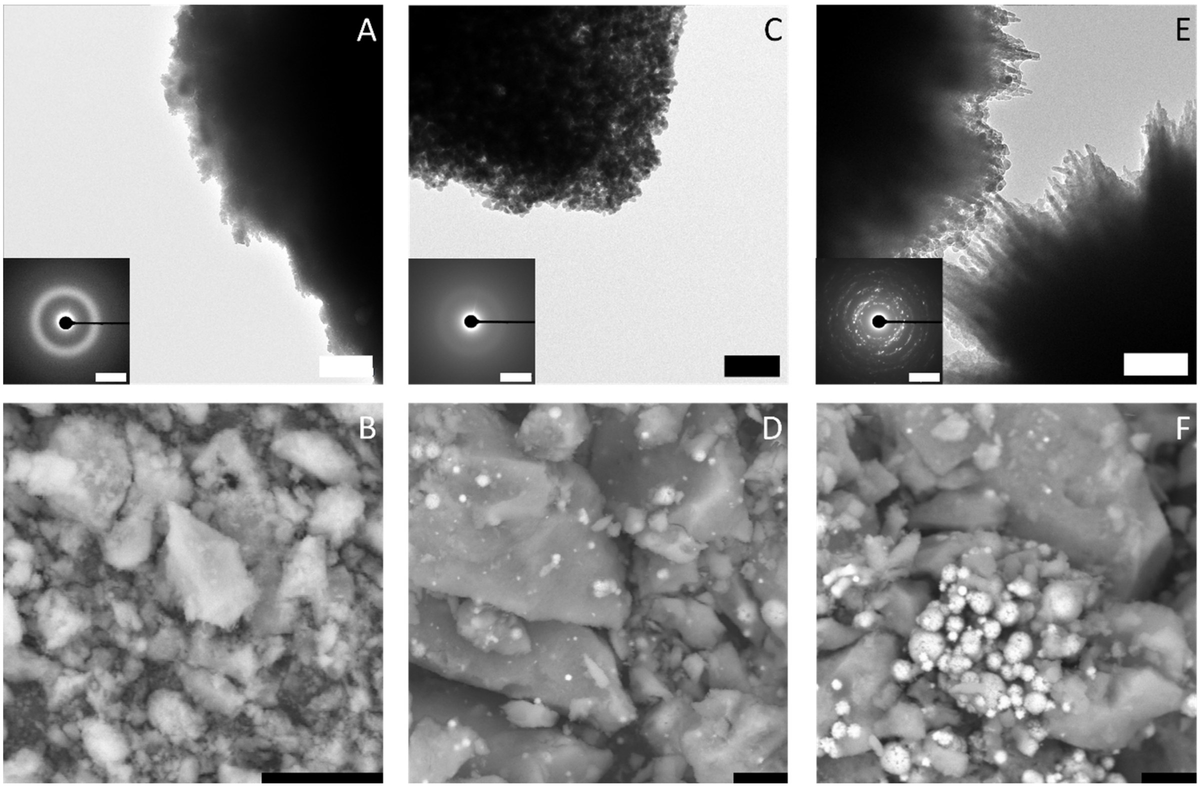

Figure 31 | TEM micrographs (A, C, E; scale bars 500 nm, 200 nm, 200 nm, respectively) with ED insets (scale bars; A 2/Å, C 2/Å, E 0,5/Å) and SEM (B, D, F; all scale bars 10 µm) images of specimens blotted from the quenched samples at different stages as indicated by arrows in Figure 29; arrow 1: left column; arrow 2: middle column; arrow 3: right column

While the molecular explanation for the more pronounced thermodynamic de-stabilisation of pre-nucleation clusters in the presence of both Mg^{2+} and PAsp remains unknown, it should be noted that it likely contributes to the synergistic increase in the kinetic efficiency towards inhibition of nucleation. Previous work has shown that an increase in ionic strength leads to similar effects, because the reduced activity of calcium and carbonate ions causes a lower amount of substance bound in pre-nucleation associates and in the second liquid phase after the liquid-liquid binodal is crossed.[110] Even though the level of IAP at high ionic strengths can be significantly higher compared to the additive free case (Figure 29), nucleation is inhibited, highlighting that the bound calcium carbonate is central to the event of phase separation as shown in chapter 4.[25, 110] Consequently, here, when mixed pre-nucleation clusters are thermodynamically destabilised, less calcium/magnesium carbonate is bound within pre-nucleation clusters and nucleation is inhibited to a greater extent than without the additives.

However, the cluster destabilisation effect in presence of both Mg^{2+} and PAsp likely cannot explain the pronounced synergistic effect with respect to inhibition of nucleation alone.

To investigate the species occurring during the early stages in presence of both Mg^{2+} and PAsp, and during the eventual drop to the constant ion product characterizing the solubility of the precipitated phase, samples were drawn at different stages (indicated by arrows in Figure 29 B), and analysed utilising TEM, SEM, EDS, FT-IR and TGA. TEM analyses illustrate that small amorphous particles (see ED pattern in Figure 31 A) are forming larger aggregates (Figure 31, left column). At the second time point, the observed particles are still amorphous but have a higher contrast compared to the first sample (Figure 31, middle column). This shows again that solidification and subsequent densification of amorphous particles due to the loss of water leads to the final product in aqueous $CaCO_3$ systems (note that unfortunately, the amount of sample obtained from time point 1 does not provide enough material for TGA measurements). The SEM micrographs (Figure 31 B, D) support this observation, as the amorphous material quenched from the pre-nucleation stage (Figure 29 B, arrow 1) exhibits a rather loose structure compared to the one obtained at the later time point.

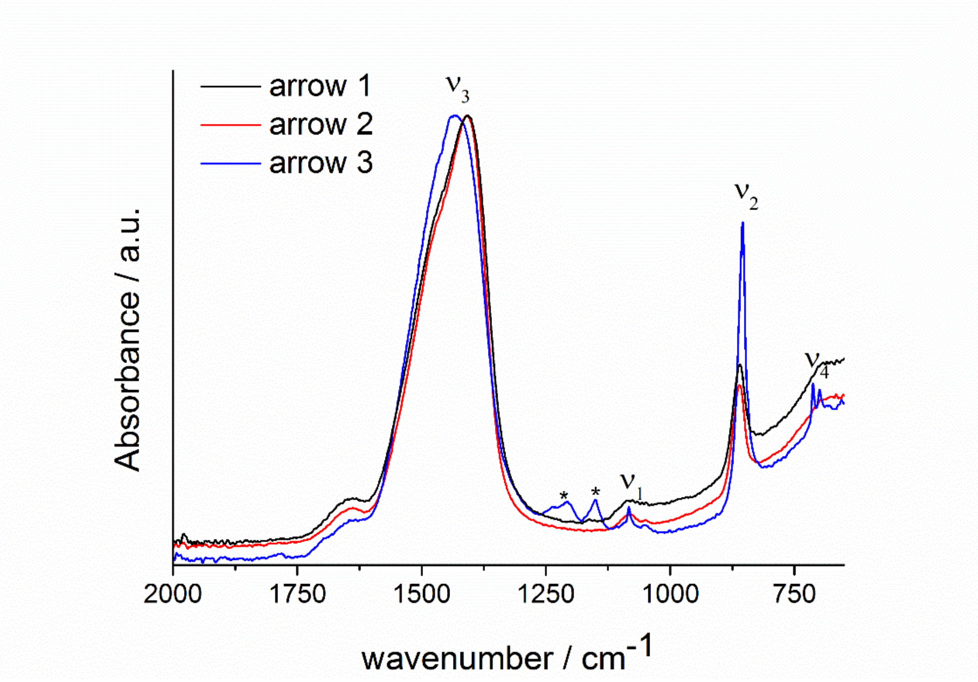

Figure 32 | ATR-FTIR spectra of the ACC samples quenched at different times in the titration assay, as indicated by arrows in Figure 1; arrow 2: red; arrow 3: black. Asterisks label bands that are due to the incorporation of polymer in the sample.

After nucleation occurred, amorphous and crystalline particles are present in the sample (Figure 31, E & F). This could be explained by a further densification of the particles and subsequent crystallisation yielding aragonite (Figure 32). FT-IR spectra of specimens quenched at the three different time points (Figure 32) show that the formed phase is amorphous, which is especially apparent from the ν_4 spectral region, which does not show any clear bands related to crystalline calcium carbonates. The ν_3 (1409/1468 cm^{-1}), ν_2 (861 cm^{-1}) and ν_1 (1083/1049 cm^{-1}) bands are typical for ACC.[53, 108, 133-137] However, considering band positions and shapes, there is no clear correlation between the ACC formed, in presence of magnesium ions and PAsp, and any ACC with distinct proto-structural features.[55-56]

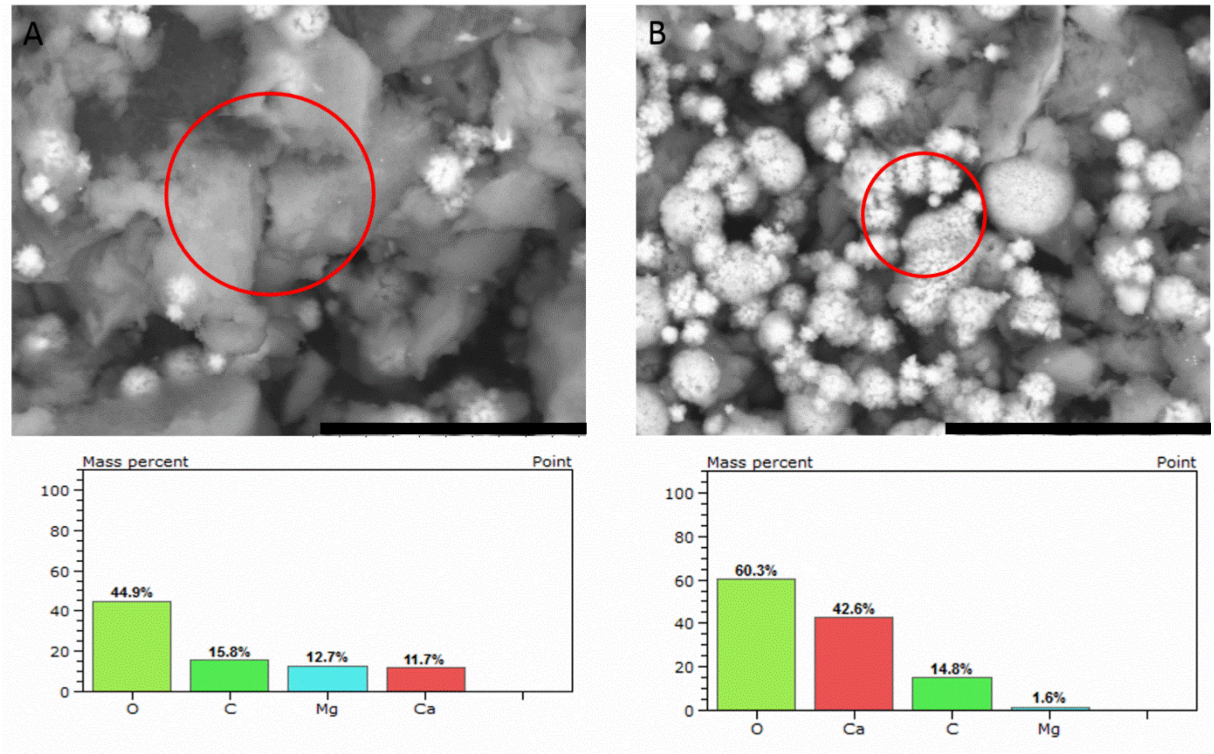

Figure 33 | SEM micrographs (scale bars 20 µm) of ACC samples quenched upon reaching a constant solubility product, as indicated by arrow 3 in Figure 29, and the respective EDS results obtained from the areas marked by circles.

While it is known that in presence of Mg^{2+}, synthetic ACC can adopt aragonite-like short-range structural features, [137] such short range order could not be observed in the FT-IR data. It should be noted, though, that the ν_1 band position coincides with that of aragonite,[138] and indeed, aragonite is formed upon reaching the constant solubility product (Figure 32, blue spectra).

In presence of PAsp, the first crystalline phase forming is vaterite (Figure 30), with Mg^{2+} alone, ACC is kinetically stabilised within experimental duration (Figure 34), whereas Rodriguez-Blanco et al.[139] report the formation of monohydrocalcite after Mg-ACC.

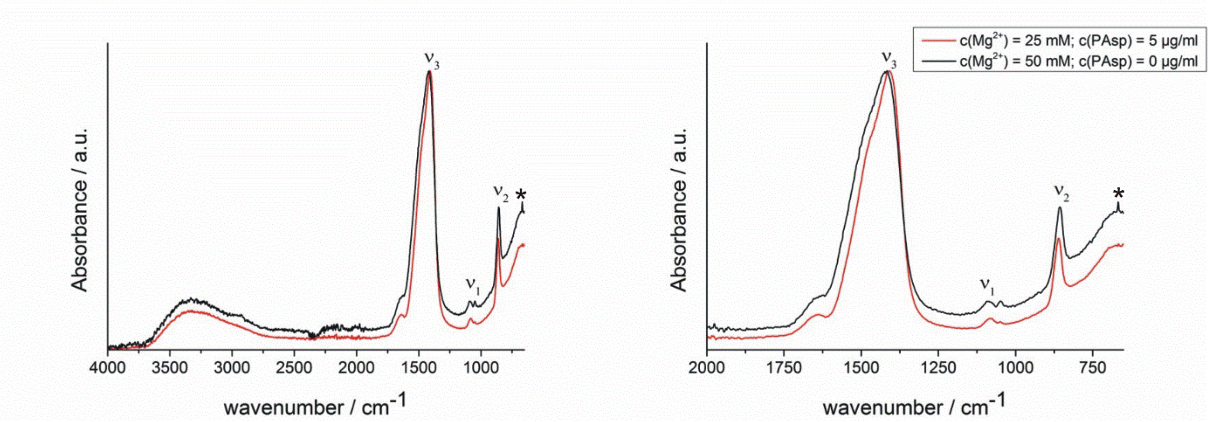

Figure 34 | Complete spectral range of the IR-spectra of the ACCs formed in presence of Mg and both Mg and PAsp The band marked by an asterisk is due to atmospheric CO_2 (668 cm^{-1}; bending vibration).

The reference experiment without any additives produces a mixture of calcite and vaterite.[36] The ACCs formed in presence of Mg^{2+} alone and in presence of both Mg^{2+} and PAsp appear to be largely identical considering the IR spectra (Figure 34). Furthermore, the presence of aragonite only when magnesium and PAsp are combined, indicates that PAsp could drive the crystallisation of the amorphous precursors, in agreement with previous studies.[71]

SEM investigation of the phase obtained upon reaching a constant solubility level (Figure 33) shows the presence of larger agglomerates, which are likely seen in TEM (cf. above) and pose similar aggregates of nanoscopic ACC entities. In addition, there are 2-3 µm sized aragonite crystals (flower-like structures, Figure 31 right, and Figure 33 B top). EDS analyses (Figure 33, bottom) show that the amorphous precipitates contain significant amounts of magnesium ions whereas the aragonite crystals contain only a few percent of magnesium. This effect of magnesium depletion can also be observed in biogenic calcium carbonates.[79]

However, owing to the presence of both amorphous (being more soluble and determining the solubility product, Figure 29) and crystalline phases (aragonite typically contains insignificant amounts of magnesium), it is difficult to delineate the composition of the different species based on EDS alone. TGA (Figure 35) of the fully amorphous precipitate quenched shortly before nucleation (arrow 2 in Figure 29) was performed to determine the composition of the precipitates. The TGA trace (Figure 35) shows three consecutive mass losses. The first one between 80-250 ºC corresponds to the release of water, the second one between 300-500 ºC to the calcination of magnesium carbonate,[140] and the third one between 600-750 ºC to the calcination of calcium carbonate. The corresponding relative weight losses are ~22%, ~18%, and ~ 18%, respectively, suggesting a $MgCO_3$ to $CaCO_3$ ratio of 1:1. This also implies that the mass of PAsp within the precipitates is negligible, consistent with the minor PAsp concentration in the titration assay experiments. Thus, TGA suggests a molecular formula $Ca_{0.5}Mg_{0.5}CO_3$•1.5 H_2O, on average.

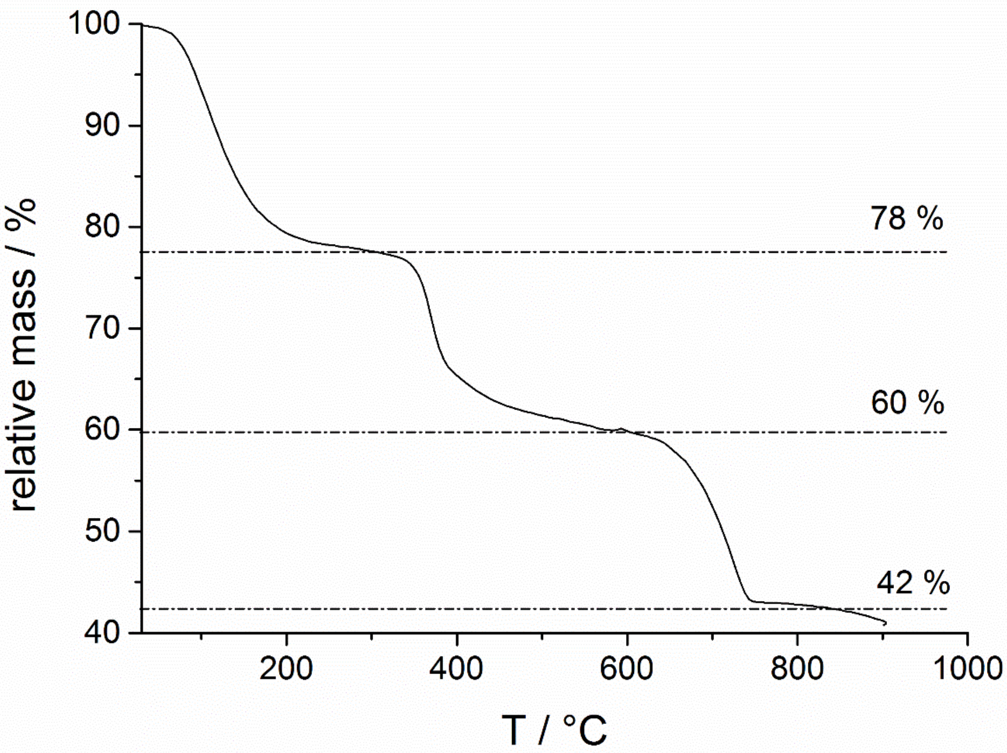

Figure 35 | TGA of an ACC sample containing both additives quenched shortly after the drop of the ion product, as indicated by arrow 2 in Figure 29

Albeit EDS analyses indicate a slightly higher Mg content of the sample, magnesium and calcium ions are distributed evenly over the whole sample (Figure 36). This suggests that only about 1/5 of the Mg^{2+} ions present in the titration experiment is incorporated into the initially amorphous precipitate. It could be shown in this chapter that the interplay between different additives is crucial for the solidification process in $CaCO_3$ systems and therefore important for the resulting crystal.

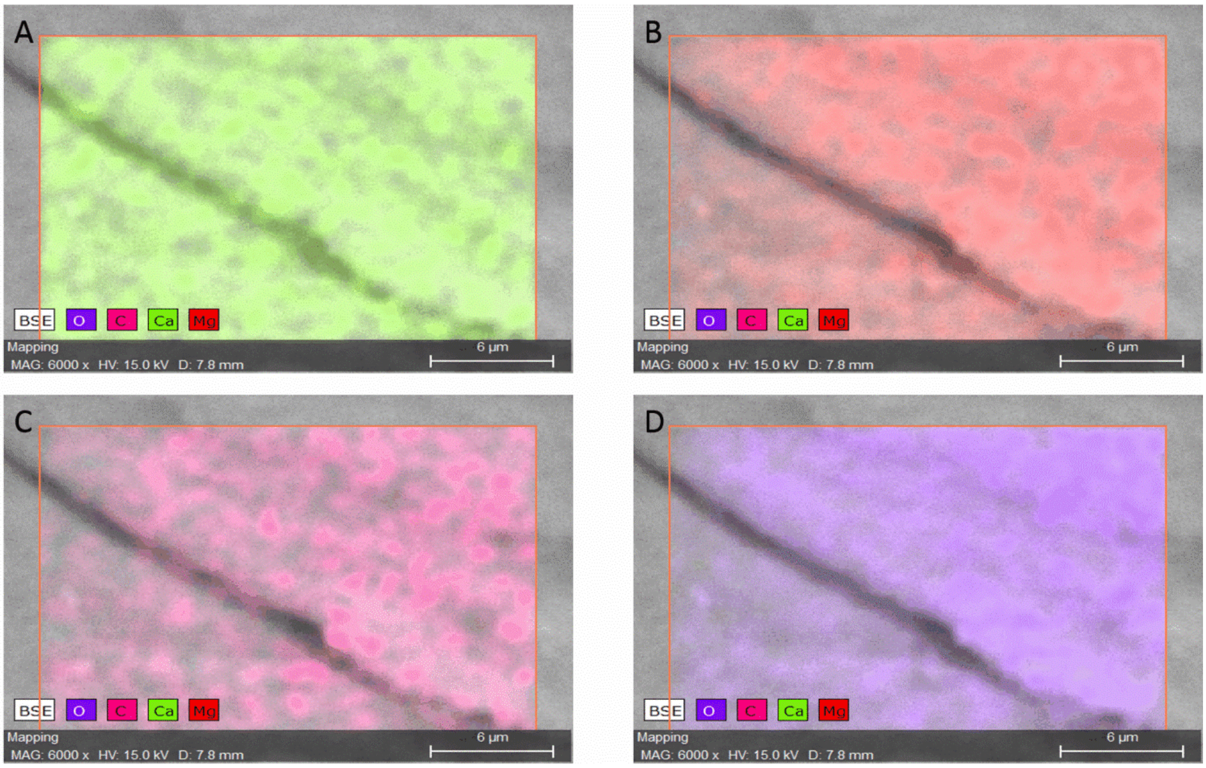

Figure 36 | EDS mapping of the different elements occurring in the sample A) Calcium, B) Magnesium, C) Carbon, D) Oxygen

7. Gel-Like Calcium Carbonate Precursors Observed by *in-situ* AFM[4]

After crossing the liquid-liquid binodal the liquid precursors can be stabilized by polymers or ions as mentioned in the introduction and shown in chapter 6. To investigate the physical properties of these liquid precursors, *in-situ* atomic force microscopy (AFM) was used. It is a well-established technique to observe interactions of proteins or small molecules with different surfaces.[141-143] *In-situ* AFM is also well suited to observe crystal growth processes directly in solution.[32, 144-145]

In this chapter, the growth behaviour of liquid-like species on a calcite {104} surface was observed using *in-situ* AFM. The liquid-like precursors are synthesized by mixing of poly(acrylic acid), calcium chloride and sodium bicarbonate (*cf.* chapter 3.10). Directly after mixing, deposition of precursors on the calcite surface can be observed. The properties of these droplets are still not completely investigated due to the relatively small existence region in the phase diagram (see also chapter 4 and chapter 6) and their instability. To examine in some detail the properties of the precursors, indentation-type tests were performed. Figure 37 presents a typical precursor profile, over which force curves are obtained. Forces are presented as a function of the distance between the hard substrate and the cantilever tip. It is seen that in all sectors of this precursor, the approaching curves show a small but abrupt attraction that occurs when the tip makes contact with the precursor surface. This is an indication of the existence of adhesion between the tip and the precursor. After this contact, the precursors deform elastically if they are thin enough, which is seen since the force increases with decreasing tip surface distance.

Note that the force increases very rapidly when the tip gets closer to the underlying calcite crystal, which is much harder than the precursor. In general, thicker areas of the precursors are more easily indented by the cantilever tip and are prone to exhibit large hysteresis in the force curves (Figure 37).

In Figure 38, the addition of the new species to the calcite {104} surface is presented as observed by *in-situ* AFM. In the height images, Figure 38 A and D, some plain spots indicated

---

[4] Parts of this chapter are published in *Langmuir* **2017**, 33, 158-163. For the sake of readability not all passages assumed from the published manuscript are cited additionally by quotation marks (“ ”). Figures taken from these publications are also not marked additionally.

by white circles (1, 3, 4, 6, 7 & 8) can be seen. An inspection of these regions shows relatively flat surfaces compared to the surrounding surface. The newly appeared species show a softer behavior clearly visible in the phase image as indicated in Figure 38 B and E. The force-distance curves (1 to 8; related to circles 1-8) show a different behavior for the approach (blue) and the retract (red) curves, which is not observed for the "clean" surface (circles 2 & 5). This feature can be explained by a gel-like structure where the AFM-tip is adhered by the growing species. The adhesion images, Figure 38 C and F, constructed by extracting, at each point the adhesion energy, W_{adh} from the adhesion force F_{adh}, perfectly correlate with the phase images and the smooth areas in the height images. In detail, first when the AFM-tip approaches the species on the surface, the tip slightly compresses the nanosized species until it hits the underlying calcite surface (4 & 6). During the retraction step, the tip is going the same way back but a significant adhesion force is observed before leaving the growth species. This hysteresis behaviour is not observed for the clean surface, Figure 38 B and E, circles 2 and 5, and can be explained assuming a gel-like behaviour of the precursors.

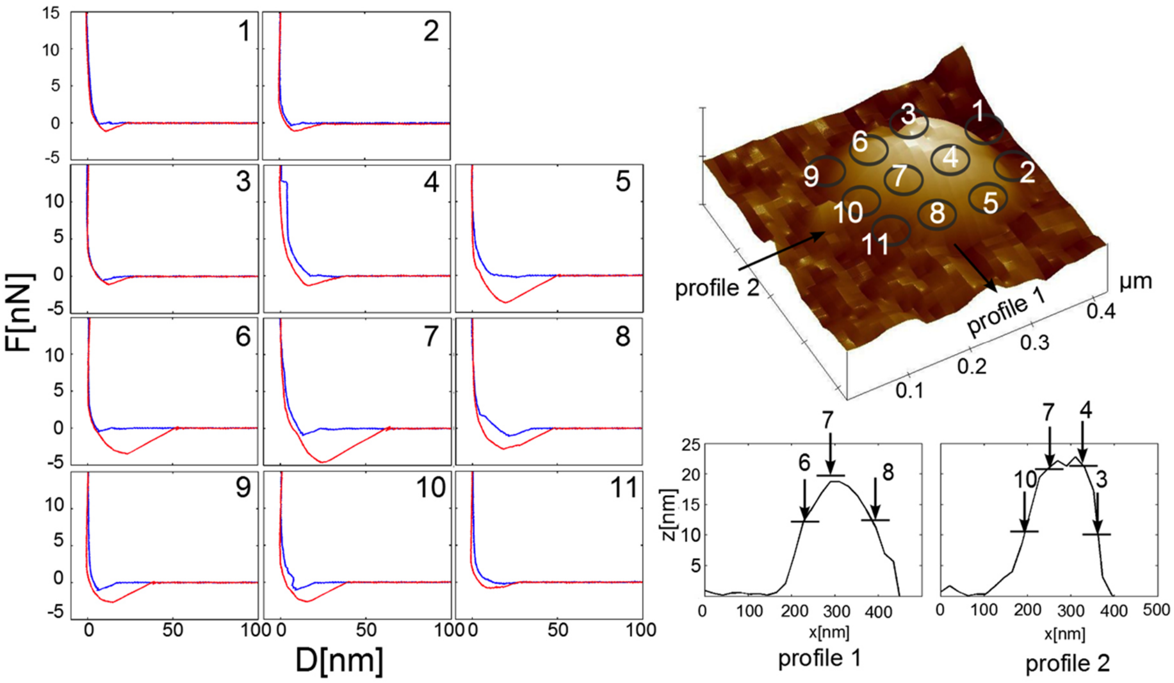

Figure 37 | Force as a function of the distance measured from the tip to the solid hard substrate. For the approaching tip (blue), some adhesion is observed through the attractive force between the precursor and the tip. This is followed by a compression, which reflects the elastic behavior of the precursors. In retraction, the elastic recovery of the precursor and the adhesion is clearly observed.

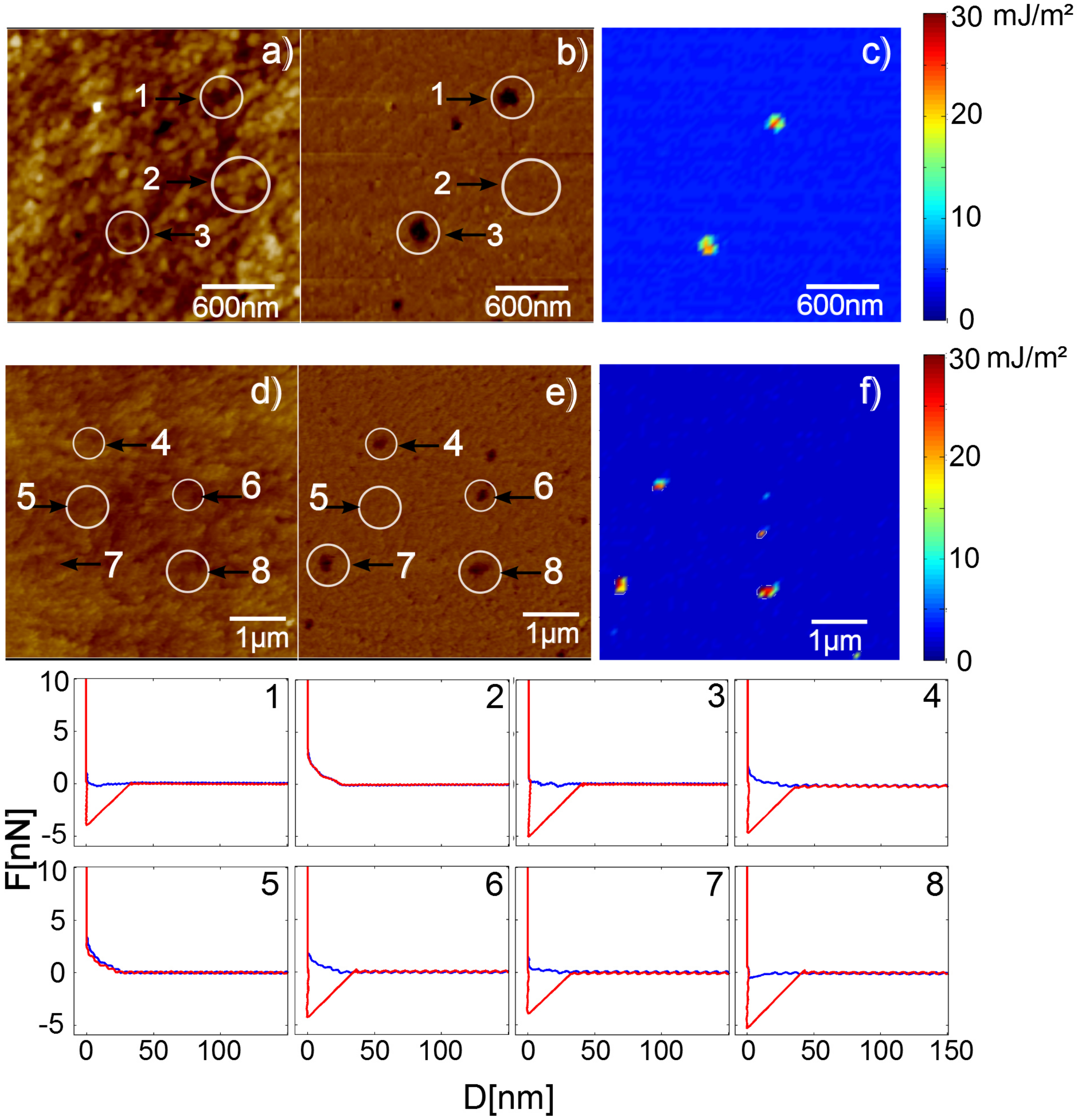

Figure 38 | In-situ AFM height (a & d), phase (b & e) and adhesion images (c & f) of a calcite surface shortly after infiltration of the solution. Numbers in the force-distance curves label the circles in the AFM height and phase images. Circles 2 & 5 show a clean calcite reference surface. Blue: approach to the surface, red: tip retraction from the surface. (Small drift downward, visible in panels c and f, is because adhesion maps are not taken simultaneously with height and phase images)

It should be mentioned that none of these features are observed in control experiments performed on calcite surface under the conditions described above but in the absence of PAA. Similarly, further controls performed with all components, with $NaHCO_3$ being the only exception, did not show the presence of soft droplets. Approaching force curves such as Figure 38 4 & 6, allow for the estimation of the Young modulus, Y_P, of the precursors through a fitting procedure. It should be noted that little adhesion or no adhesion is observed outside the precursors. Moreover, the force curves obtained outside of the precursors, measured through the same indentation protocol, showed no difference in approaching and retraction. Analyses of these curves indicated the existence of a thin section in which the Young modulus was close to 10 MPa that is much softer than the calcite crystal, but significantly harder than the precursors. This soft layer, whose depth is about 10 nm, is attributed to the roughness of the calcite crystal under growth conditions. The soft layer thickness is estimated directly from the force curve in approaching, by measuring the distance from the first tip-surface contact to the point where the force increases very rapidly due to the presence of the hard crystal.

The Young's modulus of the precursors is obtained as a fitting parameter through a suitable model expression for the force curve in approaching. The compression response force of a thin elastic film of thickness h, of Young modulus E, bound to a relatively hard substrate writes,[146]

$$F \approx \frac{16E}{9} R^{1/2} \delta^{3/2} \left[1 + 1.13\sqrt{R\delta/h} + 1.283 R\delta/h \right] \tag{37}$$

Where R is the curvature radius of the indenter and δ its penetration.

It is worth noting that for the application of this model, adhesion should be small. Therefore, curves with this feature were selected for Young modulus assessment. Experimentally, the thickness h of the soft layer can be read directly from the force curves since h corresponds to the distance between the point of first contact of the tip with the precursor and the hard substrate. For the precursor of Figure 37, the average h is about 20 nm, but can reach values up to 200 nm in thicker precursors. Through the fitting of a representative number of force curves (not shown), the average Young modulus of precursors ranged from 1 MPa to 2 MPa. This value is at least four orders of magnitude smaller than that of the calcite crystal and is characteristic of a relatively soft material. This small value of Young's modulus suggests that the observed species are gel-like structures composed of mineral and polymer. An approximate value of the work of adhesion, W_{adh}, is obtained through the measurement of the adhesion force F_{adh} that is directly determined by the magnitude of the snap off force, from the retraction curve. Since the Young's modulus of precursors revealed a relatively soft material, the known Johnson Kendall and Roberts formula[147] was employed, relating adhesion energy to force of adhesion. This is:

$$W_{adh} = \frac{2F_{adh}}{3\pi R} \tag{38}$$

This methodology allows for the construction of adhesion maps.

A value of $Y_P = 2$ MPa was obtained, which is about 2 orders of magnitude lower than that of a relatively soft rigid material but is the typical range of hydrogels like, for example, 0.91 ± 0.14 MPa for a poly(acrylic acid) hydrogel.[148] Interestingly, the shape and the range of the penetration in curves 2 and 5 (zones free of precursors) indicate the presence of a thin and soft layer of calcite of thickness about 10 nm. The Young's modulus of this layer is about 10 MPa, and this softness can be attributed the crystal roughness developed during the surface solution contact. However, other effects cannot be ruled out. Notice that force curves 1, 3, 7, and 8 in Figure 38 do not reveal a soft layer in approaching because the precursors are very thin in such areas. However, a strong adhesion in retraction is clearly visible. In addition, a complete exploration of the distribution of stiffness and adhesion over the surface of a single precursor is given in Figure 37. In order to check the mechanical stiffness of macroscopic samples, PAA-$CaCO_3$ hydrogels were prepared,[149] using PAA of large molecular weight (M_w ~ 100 000 g/mol), and independent measurements of Young's modulus were performed. Slopes extracted from stress versus strain curves lead to values of Young's modulus in the range of 50 kPa, which is significantly smaller than values obtained for droplets through indentation methods. This difference in bulk modulus is caused by the fact that calcium carbonate hydrogels, based on large molecular weight PAA, are spongy structures compared to precursor droplets.

To compare the growth behavior of these gel-like structures with the results reported by Gower *et al.* for the thin film formation by the PILP phase,[44] the solution was kept over several days on top of the calcite surface and analyzed again by *in-situ* AFM. The obtained results are shown in Figure 39. After the solution is injected into the cell, the slow evolution of the surface is followed through atomic force images in tapping mode and indentation series for 6 days. A set of data is taken every day (data for day 1 are taken 2h after injection) and force curves analyzed. Each raw image in Figure 39 presents AFM images indicating height, phase and adhesion, followed by the adhesion histogram and typical force curves in approaching and retraction. Adhesion diminishes with time. However, the analysis of the height images indicates that, while no significant change of the precursor diameter occurs in time, the surface roughness diminishes by a factor 2 within a period of 6 days.

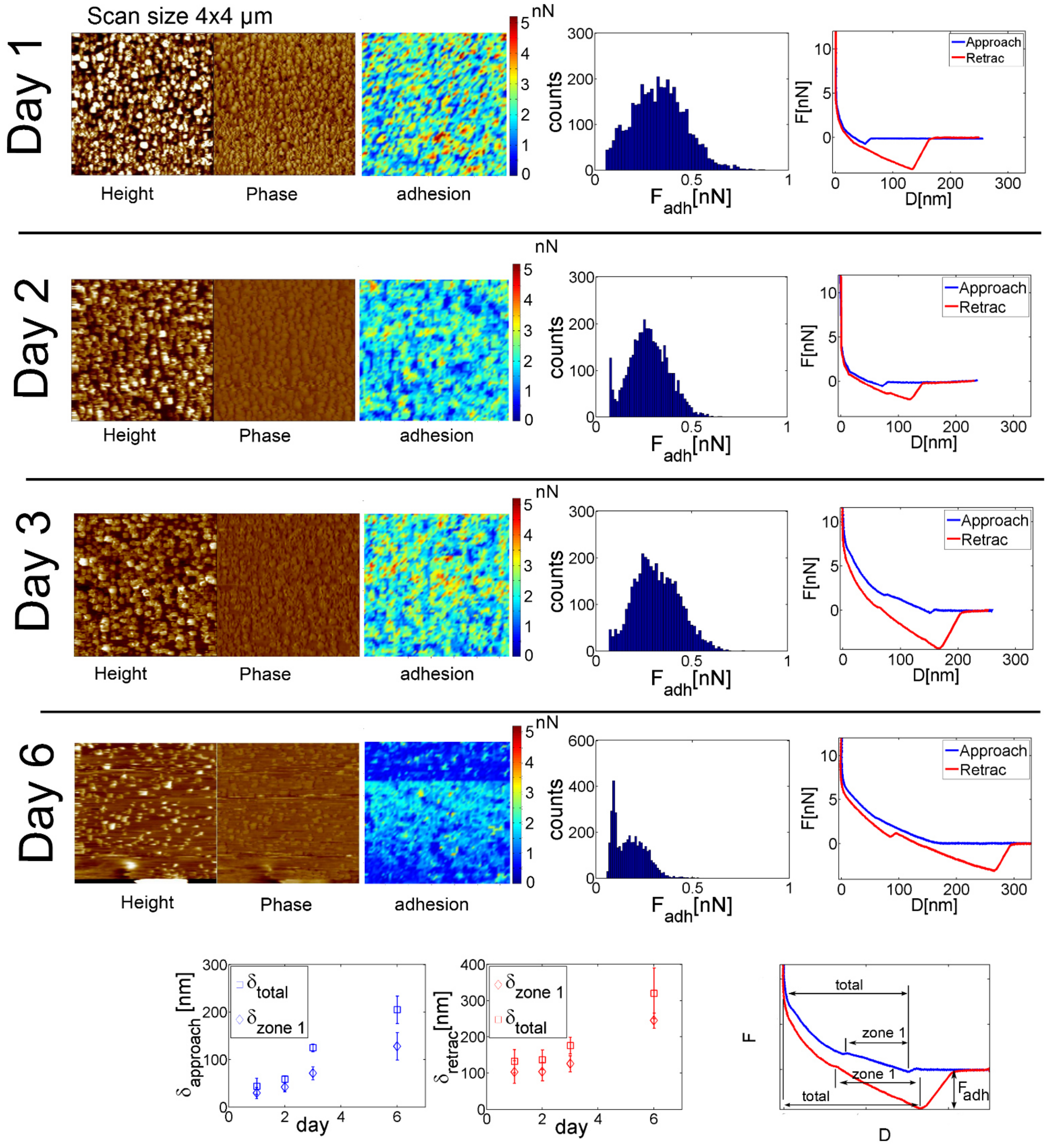

Figure 39 | The time evolution of precursors followed during 6 days. Each row indicates AFM images of height and phase and adhesion maps. The adhesion map is made by plotting the force of adhesion, F_{adh} at each point. Corresponding adhesion histograms and typical force curves are also shown. Lowest row indicates time evolution of total width of zone 1 and the thickness of precursor layer as defined in the right panel

As the precursors age, the force curves present interesting features (see rightmost panels in Figure 39) In approaching, a first zone (zone 1), in which the force grows linearly with penetration depth is obvious. As the tip approaches further, a different zone in which the force increases very rapidly with penetration is clearly visible. The latter can be associated with a plastic zone due to the progressive penetration of the tip into the precursor through plastic deformation, whereas the former is expected to result from either elastic or hyper elastic deformations. The strong increase of the force in zone 2 is then due to the tip reaching the hard substrate. These two zones are also observed upon retraction. Different zones and force features are summarized in the lower panels in Figure 39. The lower panel in Figure 39 shows that both the total width (zone 1 + zone 2) and the width of zone 1, increase with time. Since force is sensitive to both the first contact with the surface and the hard substrate, it is natural to identify the extension of the penetration force as the thickness of the layer precursor. Analysis of these quantities in time (lower panels Figure 39) indicates that thickening of the precursors takes place at a rate of about 1.4 nm/hr. It is worth noting that the long-range of the force on retraction curves indicate that the precursor surface can deform significantly under pulling before tip detachment actually occurs. An estimate of this deformation can be obtained by subtracting $\delta_{\text{zone 1}}$ in approach to $\delta_{\text{zone 1}}$ in retraction. From the corresponding panels (lowest) in Figure 39, it can be seen that these distances differ in about 50 nm. This is consistent with the observations of a relatively high adhesion and the soft character of precursors. Indeed, through a rough estimate, from maximum adhesion force (5 nN) and tip size (about 20 nm), it can be found that the tensile stress near the tip can reach values greater than 10 MPa, which implies that typical strain is very large (given the relatively low value of the measured Y_p of about 1 MPa), which would produce precursor elongation likely exceeding the typical distance of the measurement (tip radius of curvature).

To follow the mechanical feature of the softer layer of zone 1 in time, we define a relative stiffness of this layer as the slope of force penetration curve $K=\Delta F/\Delta\delta$ (see Figure 39 lower panel, for definition). At the early stages of growth *via* the precursors, the average of K is about 0.02 N/m and fluctuates significantly. However, fluctuations decrease and stabilize to about 20% after day 2. Overall, the average K does not change with time, and its value is kept close to 0.02 N/m, suggesting that growth continues by addition of (liquid) precursors on top of the freshly formed surface. It is worth noting that further analyses[150] of force curves demonstrated that the Young's modulus of the precursors ranges from 1 MPa to 2 MPa, which is close to the average value obtained from fit of force curves in the case of thin precursors.

These observations are in complete agreement with the postulated mechanism by Gower.[44] Furthermore, such a crystal growth cannot be explained by the classical Kossel layer by layer growth[151] because an ion-by-ion growth mechanism would lead to distinct layers with steps or kinks rather than to complete precursor species addition in the micrometer range.

8. Conclusions[5]

The results of this thesis shed light on the role of pre-nucleation clusters (PNCs) and liquid mineral precursors during phase separation in the aqueous calcium carbonate system. First, the THz absorption spectroscopy experiments show a transition from an initial linear increase to a non-linear behaviour. This is evidence for a change in water dynamics that can only be explained by a liquid-liquid phase separation, because no change in the linear increase of the ion-activity product (IAP) can be observed at that point. Consistently, assessments of induction times show that the observed changes in THz absorption do not correlate with the onset of precipitation of solid calcium carbonate. In addition, no precipitation is observed in the stop experiments if the liquid-liquid binodal is not crossed (chapter 4). The liquid-liquid transition – the system is saturated with respect to proto-structured ACC at this point – structurally and chemically corresponds to nanodroplet formation (high-density liquid)[52] via a higher order phase transition from the mother solution with PNCs (low-density liquid; Figure 40 B-C). To examine the characteristics of liquid-liquid phase separation in more detail, additional titration experiments were performed. The pathway to solid calcium carbonate in this case depends on the ionic excess in the system (a titration of bicarbonate buffer into calcium solution is abbreviated as $CO_3^{2-}\rightarrow Ca^{2+}$ and of calcium solution into bicarbonate buffer as $Ca^{2+}\rightarrow CO_3^{2-}$). In either case, the basic precursors are PNCs, which can become nanodroplets upon crossing the liquid-liquid binodal (Figure 40). Nanodroplets have internal pools of high-density liquid water (Figure 40 C, dark blue). Subsequently, the reduction of interfacial surface area drives further aggregation (Figure 40 E),[55] yielding hydrated proto-structured ACCs with a diameter of ~20 nm in case of the $Ca^{2+}\rightarrow CO_3^{2-}$ experiments.[53] During the $CO_3^{2-}\rightarrow Ca^{2+}$ experiments, the nanodroplets agglomerate to form larger networks, constituting a spatially much more extended second liquid phase than in $Ca^{2+}\rightarrow CO_3^{2-}$ experiments – most likely stabilized by electrostatic interactions due to the calcium excess – in which the formation of ACC takes place. These droplets seem to exhibit larger structures up to 500 nm but likely shrink during densification. The ACC particles in the second liquid phase can finally transform to crystalline particles and form the final crystal as has been suggested recently.[130]

---

[5] Parts of this chapter are published in *Angew. Chem. Int Ed,* **2017**, 56, 490-495, *Langmuir* **2017**, 33,158-163, and *CrystEngComm* **2015**, 17, 6857-6862. For the sake of readability not all passages assumed from the published manuscript are marked by quotation marks (“ ”) additionally.

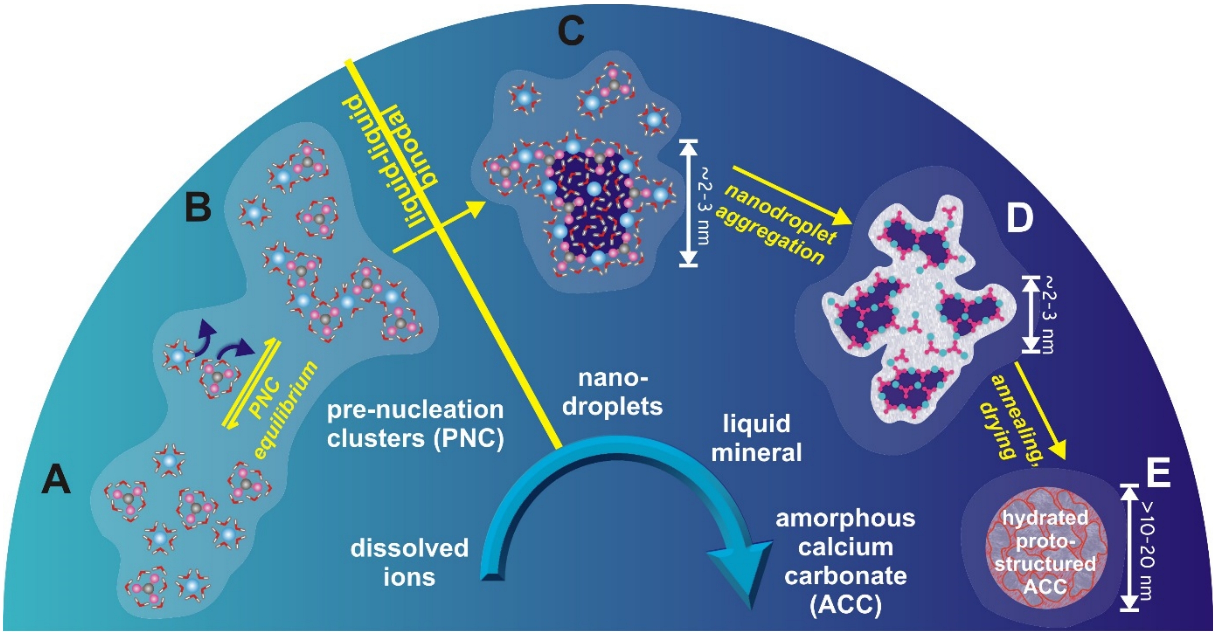

Figure 40 | Role of hydration dynamics during calcium carbonate nucleation. A) Onset of nucleation from hydrated calcium and carbonate ions where the light blue background indicates bulk water. B) Association of ions is accompanied by a partial dehydration of the ionic precursors. C) Liquid-liquid separation can occur upon crossing the liquid-liquid binodal, and structurally and chemically corresponds to nanodroplet formation (high-density liquid) from the mother solution with PNCs (low-density liquid). D) Aggregated nanodroplets of hydrated calcium carbonate (dark blue) embedded in the network of their dynamical hydration shells (steel blue). E) Further annealing and drying results in hydrated proto-structured amorphous calcium carbonate (ACC), approx. 10-20 nm in size. All sizes of precursors and intermediates indicated in the figure were determined elsewhere.[25] The fact that the liquid-liquid binodal limit is governed by the stability of solid ACC strongly suggests that it is formed upon solidification of the liquid precursors, rather than via a second nucleation event.

It is important to recognize that the liquid-liquid phase transition occurs in the pre-nucleation regime, which is not detected by the continuously developing IAP. The equilibrium constant $K_{cluster}$ quantifies the pre-nucleation ion association equilibrium, which includes the formation of PNCs, but the fact that there is no change upon liquid-liquid separation categorically implies that the very same value for the equilibrium constant characterizes the equilibrium between the ions across the liquid-liquid phase interface. This can be illustrated by the involved equilibria.[25]

$$Ca^{2+} + CO_3^{2-} \rightleftharpoons (CaCO_3)_{cluster}$$

$$[Ca^{2+} + CO_3^{2-}]_{L1} \rightleftharpoons [Ca^{2+} + CO_3^{2-}]_{L2}$$

From these equlibria the law of mass action can be deduced, quantifying the observation outlined above:

$$K_{cluster} = \frac{[CaCO_3]_{cluster}}{IAP_{L1}} = \frac{IAP_{L2}}{IAP_{L1}} = K_{L-L} \tag{39}$$

Where $K_{cluster}$ and $K_{L\text{-}L}$ are the pre-nucleation equilibrium constants for cluster formation and the equilibrium constant for the liquid-liquid phase co-existence, respectively. The concentrations of bound ions in PNCs and the second liquid phase are labelled as $[CaCO_3]_{cluster}$ and IAP_{L2}, respectively, and the product of the concentrations of free calcium and carbonate ions in the mother solution are labelled as IAP_{L1}. The equilibrium constant directly gives Gibbs free energy for PNC formation ($\Delta G_{cluster}$) according to:

$$\Delta G_{cluster} = -RT\ln K_{cluster} \tag{40}$$

Taken together, this demonstrates that the chemical potential ($\mu = \left({}^{\partial \Delta G}/_{\partial n}\right)$) develops continuously upon forming dense liquid droplets from PNCs, which consequently is not a first order phase transition in the sense of Ehrenfest. It is a continuous phase transition where the change in chemical potential does not even seem to exhibit a kink. The critical temperature of the liquid-liquid coexistence can be determined, as the compositions of the two liquid phases are identical at the critical point ($IAP_{L1} = IAP_{L2}$). This can only be realized when $K_{L\text{-}L}$ becomes unity. Therefore, $K_{cluster}$ must equal one, according to equation 39. The temperature dependency of $K_{cluster}$ can be accessed by:[106]

$$\Delta G_{cluster} = -RT\ln K_{cluster} = \Delta H_{cluster} - T\Delta S_{cluster} \tag{41}$$

Where, $\Delta H_{cluster}$ is the enthalpy and $\Delta S_{cluster}$ is the entropy associated with PNC formation, respectively, which are taken from the literature.[111] As $K_{cluster} = 1$ the Gibbs free energy ($\Delta G_{cluster}$) becomes zero (equation 40) and the evaluation yields a critical temperature of 98 K ($T_{crit} = \Delta H_{cluster}/\Delta S_{cluster}$) , which is far below the freezing point of water and cannot be reached for real aqueous $CaCO_3$ systems in the liquid state.

The solubility products of proto-structured ACCs define the locus of the liquid-liquid binodal. By means of temperature-dependent titration experiments at different pH values, the solubility products of proto-structured ACCs are obtained. Thereby, an advanced phase diagram for the liquid-liquid miscibility gap of calcium carbonate is constructed (Figure 41). This diagram shows the solid-liquid binodal represented by the solubility of calcite (black squares) as the stable phase, and vaterite (orange stars) as the unstable anhydrous crystalline form. Aragonite, however, is not shown in the phase diagram for the sake of clarity because its solubility product is close to that of calcite. The liquid-liquid binodal limit for titration experiments at pH 9.0 is located at the solubility product of pc-ACC indicated by the red dashed line. The dashed blue line represents the liquid-liquid binodal limit for pv-ACC that forms at pH 10.0. Recently, Farhadi *et al.* reported the formation of pa-ACC alongside pv-ACC above ~40°C and pH 9.80.[56] This implies that the ACC solubility threshold above 35°C represents the binodal limit for the liquid precursor phase to pa-ACC. It is obvious that at 35°C, the solubility products of pv-ACC and pc-ACC exhibit a similar value ($2.9 \cdot 10^{-8}$ M²). Considering all this, it can be speculated that there is a triple point in the liquid-liquid coexistence. At this point, three distinct liquid phases that are precursors to solid proto-structured polyamorphs – namely pc-, pa- and pv-ACC – co-exist, which can be understood as liquid polyamorphism. As the pH of this point should lie between pH 9.0 (pc-ACC) and pH 10.0 (pv-ACC), it can be suggested that the triple point is located at 35°C , an IAP of $2.9 \cdot 10^{-8}$ M² and pH ~9.5.

Titration experiments with slow addition rates of 0.1 µmol/min result in a solubility product related to proto-structured ACCs after solidification. To explore the liquid-liquid miscibility gap further, titration experiments with faster addition rates (1.0 µmol/min and 10.0 µmol/min) were performed. It was shown that various ACCs with different stabilities are accessible by a faster addition of calcium solutions to (bi)carbonate buffers at different pH values and temperatures. These results indicate that the stability of the second liquid phase is directly linked to the stability of the formed ACCs. When ACC is formed in a more metastable regime of the liquid-liquid coexistence region, the resulting ACC feature a higher solubility product, which indicates lower thermodynamic stability. This behavior can again only be explained if the ACCs are formed via solidification of a liquid phase and not by a second independent nucleation event within the dense liquid.

To complete the phase diagram of the liquid-liquid miscibility gap, the spinodal limit was determined. Cartwright *et al.* speculated that the corresponding IAP values could be obtained by direct mixing of two highly concentrated calcium and carbonate solutions (>1M), which is supported by the results presented in this thesis.[55, 108] Mixing of the two solutions even faster than above leads to the unstable region of the liquid-liquid miscibility gap (spinodal regime). Assuming solidification of the liquid precursors formed upon spinodal demixing, the solubility product, and with it IAP_{L2}, cannot assume higher values than the one that defines the locus of the liquid-liquid spinodal limit. Therefore, direct mixing experiments were performed, which lead to IAPs of $2 \cdot 10^{-6}$ M^2 at 25°C. This value was obtained by measurements with a Ca^{2+}-ISE and needs further confirmation by additional measurements, like turbidity measurements. Future experiments also require use of a KPG instead of a magnetic stirrer owing to the formation of gel-like calcium carbonate phases under spinodal conditions. Nevertheless, the obtained ACC solubility product is in the same order of magnitude as reported by Nielsen *et al.*,[107] who used the same synthesis protocol but the solubility product was determined using turbidity-based titrations. As these values are accepted within the scientific community, they were used to construct the spinodal branch of the phase diagram.

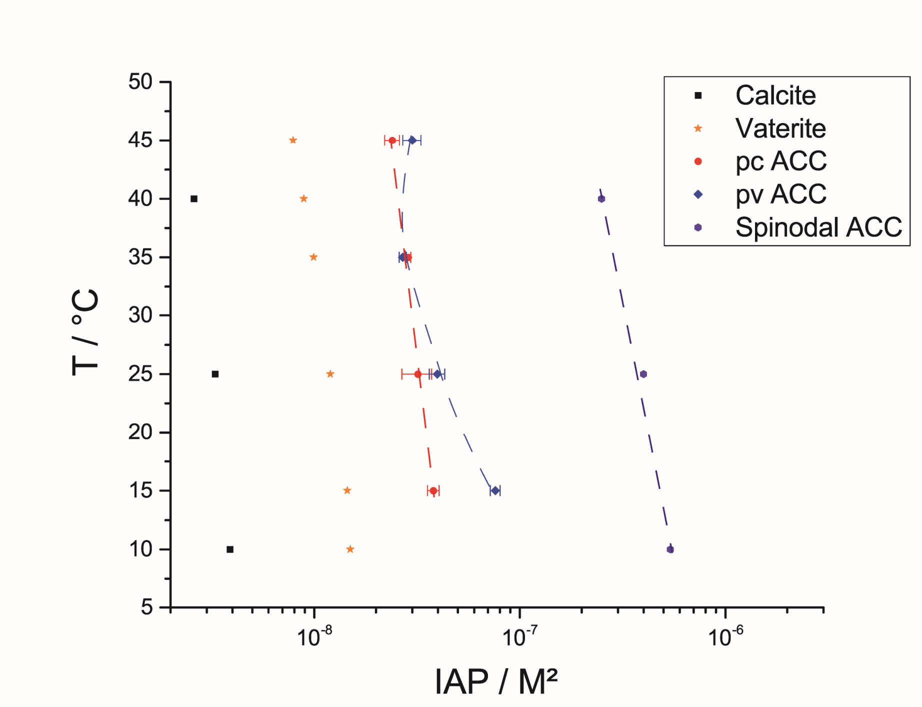

Figure 41 | Phase diagram for the aqueous calcium carbonate system; The values for the spinodal ACC can be found in the literature.[108] Note the lines represent no model and are guidelines for the eye.

Assessment of the influence of common inhibitors, namely poly(aspartic acid) (PAsp) and poly(acrylic acid) (PAA), confirms that the locus of the liquid-liquid binodal limit is not modified by the presence of these additives. The reasons for the inhibition of nucleation are still unclear but several explanations seem profound. It is possible that nanodroplets are colloidally stabilized by electrosteric interactions of polymers adsorbed on the mineral precursors.[131] In addition, the polymers may hamper the dehydration of the nanodroplets, thereby inhibiting the formation of solid forms of calcium carbonate and stabilizing the so-called PILP droplets. Furthermore, the combination of magnesium ions and poly(aspartic acid) brings about a pronounced synergistic effect leading to a significantly stronger inhibition of nucleation as compared to the individual contributions of the single additives. In part, this synergistic effect can be rationalised by the thermodynamic destabilisation of pre-nucleation species by magnesium ions, which results in a smaller amount of calcium/magnesium carbonate bound in a second liquid phase, which seems crucial for solidification. In addition, the polycarboxylate stabilizes the nanodroplets against aggregation and/or solidification as shown by THz spectroscopy. Following the above hypothesis, the stronger hydration of magnesium ions compared to calcium ions may lead to an even stronger hydration and, with it, a stronger stabilization of nano-droplets in the calcium/magnesium carbonate system in combination with PAsp, which is supported by recent published work.[111] A stronger hydration of nanodroplets can explain the inhibition of particle formation as the densification of precursors is a key step underlying particle formation in the $CaCO_3$ system as discussed above. From the point of view of classical nucleation theory, in contrast, the effect is difficult to understand, since the level of supersaturation is in fact distinctly increased when compared to the reference scenarios – already from the earliest stages of the experiment. These findings strongly suggest that magnesium ions may also play a significant role in the effectiveness of biological proteins, which often contain acidic mineral binding domains based on repeating units of aspartic acid.[15, 152] The synergy of mixtures of additives may thus be central to the realisation of sophisticated crystallisation control, since it is likely tuneable by the relative concentrations of the active co-additives.

Last, it was shown in this thesis for the first time that gel-like precursors – which were likely liquid before they encountered the surface – are a crystal growth species in inorganic crystal systems, like they appear in protein crystallization where such intermediates are well known.[153] This supports a non-classical crystal growth pathway involving micron-sized species as materials reservoir for crystal growth. Such liquid growth species could serve as a possible explanation for the growth of the elaborate and complex biomineral architectures and also be a unique precursor to realizing a plethora of complex shapes of synthetic crystals. These precursors can probably be used to build complex structures, comparable to biogenic ones.

9. Outlook

The before presented results raise some additional questions about the calcium carbonate system in general and some specific questions related to biomineralization processes. One important question can be related to chapter 4 and the locus of the liquid-liquid binodal. In this case, it is important to investigate peptides that are directly involved in the formation of biominerals. It could be a huge step in the understanding of biomineralization whether these peptides influence the locus of the liquid-liquid binodal limit or not. The method of choice would be again THz spectroscopy to gain this information. There is also a need to explore the effects of nucleation promoters like sugars or other small molecules on the locus of the liquid-liquid binodal limit.[75, 78]

Another crucial point, which should be addressed in the future, is the determination of the liquid-liquid spinodal limit in the aqueous $CaCO_3$ system. As described in the experimental chapter, it should be possible to locate the spinodal and confirm the ACC phase diagram, by the use of temperature dependent direct mixing experiments.

The short-range order of the ACCs obtained at different conditions like addition rate dependent titrations or direct mixing experiments is also of high interest for future studies. It can be further assessed by spectroscopic methods like ss-NMR, EXAFS and IR spectroscopy. Information about the chemical composition can be gathered by EDX and TGA measurements. A similar project is necessary to obtain information on the influence of additives on the ACC structure. An important question, which should be solved is, if and how do Mg^{2+} ions in combination with other additives influence the short-range order of ACC and how do they stabilize ACC. These results could then be compared to biogenic ACC.

One important question that raises from the last chapter is; could liquid precursors like PILPs be used in a simple and effective way for practical applications. Such application could be ranging from restoration of artwork to the improvement of artificial materials to a possible use in the building industry as a hardener.

10. Summary

Many important phenomena depend on calcium carbonate nucleation and crystallisation, *e.g.* the incrustation of pipelines or the formation of coral reefs. The investigation of the early stages of phase separation of calcium carbonate was the topic of this work, addressing open questions within the frameworks of "non-classical" nucleation and crystallization. As established in previous work, the first species, which appear in the nucleation process, are solute pre-nucleation clusters (PNCs), which exhibit a highly dynamic, chain-like structural form called DOLLOP (dynamically ordered liquid-like oxyanion polymers).[25] In contrast to classical nucleation theory (CNT) these clusters are thermodynamically stable and occur already in undersaturated solutions. It is hypothesized that the dynamics of PNCs can significantly decrease upon reaching a certain ion activity product (IAP), and thereby, the PNCs transform into phase-separated nanodroplets or liquid mineral precursors. These nanodroplets then agglomerate and form amorphous calcium carbonate (ACC) *via* solidification, or a second nucleation event. Previous work showed that ACC that is formed via equilibrated PNC precursors exhibits short-range orders that relate to distinct anhydrous crystalline polymorphs of calcium carbonate, which is controlled by pH and temperature.[53, 56]

The first part of this thesis examined the transition from PNCs to liquid mineral precursors, thereby proving and quantifying the aforementioned hypothesis. The solvent, in this case water, plays an important role for nucleation mechanisms. A titration assay in combination with THz spectroscopy revealed nonlinear changes in THz absorption during the early stages of $CaCO_3$ nucleation. This provided evidence for altered coupled motions of hydrated calcium and carbonate ions. The direct link between these changes and the continuous development of the IAP during the early stages of precipitation revealed the locus of a liquid-liquid binodal limit in aqueous $CaCO_3$ solutions. The liquid-liquid binodal was located at the ion activity product of the proto-structured ACCs for pH 9.0 and pH 10.0 ($IAP_{pc} = 3.1 \cdot 10^{-8}$ M² and $IAP_{pv} = 3.8 \cdot 10^{-8}$ M², respectively). The THz spectroscopy experiments in combination with the titration experiments strongly suggested that, after liquid-liquid phase separation, solid ACC was formed *via* solidification of the liquid precursors, and not a second nucleation event. Furthermore, advanced titration experiments employing different mixing conditions illustrated that calcium into carbonate titrations ($Ca^{2+} \rightarrow CO_3^{2-}$) follow a different pathway than carbonate into calcium experiments ($CO_3^{2-} \rightarrow Ca^{2+}$), as the liquid precursors are more stable in $Ca^{2+} \rightarrow CO_3^{2-}$ titrations probably due to electrostatic stabilization. In addition, CO_3^{2-}→Ca^{2+} titrations in combination with cryo-TEM supported the notion that liquid precursors always occurred during $CaCO_3$ nucleation. Here cryo-TEM clearly showed co-existing amorphous and crystalline structures, while the Ca^{2+}-ISE detected a solubility product related to vaterite but not ACC, which is not expected as the ISE always detects the most soluble phase. These findings imply that the observed ACC was liquid or was 'hidden' in a dense liquid phase.

The second part was advanced on this insight by establishing experiments towards the construction of a phase diagram for the metastable liquid-liquid coexistence in the aqueous $CaCO_3$ system, in which three proto-structured ACCs were considered. This was achieved by means of temperature- and rate-dependent titration experiments. These experiments showed that various different, progressively more (thermodynamically) metastable ACCs were accessible by increasing the titration rates. The precipitated ACCs most likely differed in the amounts of water incorporated into their structure as indicated by FT-IR spectroscopy, leading to different solubility products – which directly reflected their thermodynamic stability. This observation was interpreted based on the notion that the ACCs had formed from liquid precursors via solidification. Faster addition rates allowed accessing a thermodynamically more metastable regime of the liquid-liquid miscibility gap, i.e., the second liquid phase was more metastable when faster addition rates were applied. This means that solidification of a more metastable second liquid phase also led to less stable ACC. All ACCs formed in the binodal regime of the liquid-liquid miscibility gap were transient towards more stable phases, like proto-structured ACCs or crystalline forms. The THz experiments together with the advanced titration experiments demonstrated that the loci of liquid-liquid binodal limits were accessible by measuring the solubility of proto-structured ACCs. Hence, the phase diagram for the liquid-liquid miscibility gap of calcium carbonate was constructed *via* temperature- and pH-dependent measurements of the ACC solubilities. The phase diagram suggests the existence of a triple point (where three different liquid calcium carbonate phases co-exist, yielding proto-calcite, proto-vaterite and proto-aragonite upon solidification) at 35 °C, an IAP of $2.9 \cdot 10^{-8}$ M^2 and at a pH ~9.5. The spinodal limit in the system was determined by direct mixing experiments and completed the left branch of the phase diagram. In addition, the experiments allowed arriving at a model to calculate the critical temperature T_{crit} for the miscibility gap by the use of the enthalpy ($\Delta H_{cluster}$) and entropy ($\Delta S_{cluster}$) for the cluster formation ($T_{crit} = \Delta H_{cluster} / \Delta S_{cluster} = {\sim}98\,K$).

The influence of different additives on liquid precursors and ACCs was examined in the third chapter. THz experiments showed that polycarboxylates, which are known to stabilize liquid precursors of calcium carbonate, significantly enhanced the kinetic stability of the metastable liquid-liquid state, but they did not affect the locus of the corresponding binodal limit. A mixture of different additives, in this case polycarboxylates and magnesium ions, was also investigated by means of titration experiments. It was shown that both magnesium ions and poly(aspartic acid) (PAsp) inhibited nucleation of $CaCO_3$. Interestingly, a combination of PAsp with magnesium ions led to synergistic effects that brought about a dramatic increase in the efficiency of nucleation and growth inhibition of nanoscopic $CaCO_3$ precursors. Analyses of the precipitated phases showed that an amorphous phase containing calcium and magnesium ions in equimolar ratios occurred. Furthermore, PAsp triggered the crystallization process, because aragonite was observed only in the presence of PAsp. Therefore, it can be speculated that Mg^{2+} ions extended the existence region of liquid calcium carbonate precursors, while PAsp kinetically destabilized ACC and caused it to crystallize. These effects appear to be crucial for biomineralization processes, where polycarboxylate motifs occur in corresponding proteins, and magnesium ions are thought to play important roles.

The last part of this thesis was concerned with the physical characterization of liquid calcium carbonate precursors, which were stabilized by polycarboxylates. These so-called "polymer-induced" liquid precursor (PILP) phases can play a role in non-classical calcium carbonate crystallization and growth processes, as thoroughly established in the literature.[6] In this thesis, the physical properties of PILPs were investigated by *in-situ* AFM studies. Here, for the first time, the observation of gel-like precursors was possible. An evaluation of the data yielded a Young's modulus of ~2 MPa for the observed precursors, which was comparable to the stiffness of poly(acrylic acid) (PAA) gels. Crystal growth on a calcite surface was observed over time by means of an *in-situ* AFM. The time dependent measurements showed that crystal growth occurred *via* the addition of gel-like precursors, which were likely liquid before they attached to the surface.

Overall, the liquid-liquid binodal limit in the aqueous calcium carbonate system was successfully quantified. In addition, it was shown that (proto-structured) ACCs form *via* solidification and not by a second nucleation event. Based on this knowledge, a phase diagram for the liquid-liquid miscibility gap was constructed, including three proto-structured ACCs.

This is a strong indication that the aqueous $CaCO_3$ system displays metastable liquid polyamorphism, where the three distinct liquid phases coexist at a triple point. Furthermore, the influence of additives – which are thought to be relevant for biomineralization – on the liquid-liquid miscibility gap was explored and the physical behaviour of stabilized dense liquids (i.e., PILPs) was investigated. Globally, this new data taken together helps to improve the understanding of "non-classical" nucleation and growth processes in general, and of biomineralization more specifically. Importantly, transferring the experimental techniques to other systems like calcium phosphates, or small organic molecules like amino acids, will allow testing the applicability of the mechanisms established for $CaCO_3$ nucleation and growth in future work.

11. Zusammenfassung

Nukleations- und Kristallisationsprozesse von Calciumcarbonat sind wesentlich für viele Phänomene, wie beispielsweise die Verkalkung von Pipelines oder die Bildung von Korallenriffen. Die Untersuchung der frühen Stadien der Phasenseparation von Calciumcarbonat war Gegenstand der vorliegenden Arbeit und behandelt offene Fragen im Kontext der „nicht-klassischen“ Nukleation und Kristallisation. In vorherigen Arbeiten wurde gezeigt, dass die ersten Spezies, welche im Nukleationprozess auftreten, gelöste pre-nukleations Cluster (PNCs) sind. Diese PNCs besitzen eine hochdynamische Struktur aus alternierenden Calcium- und Carbonat-Ionen, welche als DOLLOPs (engl. dynamically ordered liquid-like oxyanion polymers) bezeichnet werden.[25] Im Gegensatz zur klassischen Nukleationstheorie sind diese PNCs thermodynamisch stabil und treten auch in untersättigten Lösungen auf. Es wird vermutet, dass sich die Dynamik der PNCs bei einer Erhöhung des Ionenaktivitätsprodukts (IAP) verlangsamt wodurch PNCs phasenseparierte Nanotröpfchen oder flüssige Mineralvorstufen bilden. Anschließend bildet sich amorphes Calcium Carbonat (ACC) über eine Agglomeration dieser Tröpfchen, oder durch ein zweites Nukleationsereignis. Frühere Studien legten dar, dass ACC, welches über im Gleichgewicht befindliche PNCs gebildet wurde, Nahordnungen aufweist, die kristallinen wasserfreien $CaCO_3$ Strukturen zugeordnet werden können. Die dabei entstehenden Nahordnungen können über den pH Wert und die Temperatur gesteuert werden.[53, 56]

Der erste Teil dieser Doktorarbeit beschreibt den Übergang von PNCs zu flüssigen Mineralvorstufen und bestätigt die zuvor aufgestellte Hypothese der verlangsamten Dynamik der PNCs. Das Lösungsmittel, in diesem Falle Wasser, spielt eine entscheidende Rolle im Nukleationsmechanismus. Ein quantitatives Titrationsexperiment in Kombination mit THz Spektroskopie offenbarte nicht lineare Änderungen in der THz Absorption während der frühen Stadien der $CaCO_3$ Nukleation. Dies gibt Grund zu der Annahme, dass Veränderungen in den gekoppelten Bewegungen der hydratisierten Calcium und Carbonat-Ionen auftreten. Eine direkte Konnexion dieser Änderungen, mit der kontinuierlichen Zunahme des IAP während der frühen Stadien der Fällungsreaktion, offenbarte die Lage der flüssig-flüssig Binodalen im wässrigen Calciumcarbonat System. Die flüssig-flüssig Binodal wurde direkt am IAP der proto-strukturierten ACCs für pH 9,0 und pH 10,0 ($IAP_{pc} = 3{,}1 \cdot 10^{-8}$ M² bzw. $IAP_{pv} = 3{,}8 \cdot 10^{-8}$ M²) lokalisiert. Die THz Absorptionsexperimente, zusammen mit den Titrationsexperimenten, legen die Vermutung nahe, dass nachdem eine flüssig-flüssig Phasenseparation stattfand, festes ACC durch Verfestigung der flüssigen Vorstufen und nicht über ein zweites Nukleationsereignis gebildet wird. Des Weiteren zeigten weiterentwickelte Titrationsexperimente, bei denen verschiedene Überschüsse vorlagen, dass Calcium in Carbonat (Ca^{2+}→CO_3^{2}) Titrationen einen anderen Nukleationsweg beschreiten als Carbonat in Calcium (CO_3^{2-}→Ca^{2+}) Experimente, da die flüssigen Präkursoren in CO_3^{2-}→Ca^{2+} Titrationen, vermutlich durch elektrostatische Wechselwirkungen, stabilisiert sind. Zusätzlich unterstützen CO_3^{2-}→Ca^{2+} Experimente die Idee, dass flüssige Vorstufen während der Nukleation von $CaCO_3$ immer auftreten. Es zeigte sich, dass im cryo-TEM sowohl amorphe, wie auch kristalline Strukturen zu erkennen waren. Die Calcium Ionen selektive Elektrode (ISE) detektierte allerdings ein Löslichkeitsprodukt, welches Vaterit zugeordnet werden konnte. Daraus lässt sich schließen, dass das im cryo-TEM beobachtete ACC entweder selbst flüssig sein muss, oder in flüssigem ACC „verborgen“ liegt.

Der zweite Teil dieser Arbeit beschäftigt sich mit der Etablierung von Experimenten die, die Möglichkeit schaffen, ein Phasendiagramm für das metastabile flüssig-flüssig Regime zu konstruieren, welches drei proto-strukturierte ACCs berücksichtig. Dies wurde mittels temperatur- und ratenabhängigen Titrationsexperimenten realisiert. Die Experimente zeigten, dass viele verschiedene, zunehmend (thermodynamisch) instabilere ACCs, durch Erhöhen der Zugaberate, zugänglich wurden. FT-IR Studien deuten darauf hin, dass die erhaltenen ACCs sich hauptsächlich durch ihren Wassergehalt unterscheiden und mit steigendem Wassergehalt ein höheres Löslichkeitsprodukt aufweisen, welches direkt mit der thermodynamischen Stabilität in Zusammenhang steht. Diese Beobachtung kann mithilfe der Verfestigungstheorie erklärt werden. Eine schnellere Zugaberate ermöglicht es tiefer in den metastabilen Bereich der flüssig-flüssig Mischungslücke vorzudringen. ACC welches in einem metastabileren Bereich verfestigt wurde, weist anschließend auch ein höheres Löslichkeitsprodukt und damit eine geringere thermodynamische Stabilität auf. Alle ACCs, welche in der flüssig-flüssig Mischungslücke gebildet wurden, sind transient in Bezug auf stabilere Phasen wie zum Beispiel proto-strukturiertes ACC oder kristalline Phasen. Die THz Studien und die weiterentwickelten Titrationsexperimente verdeutlichten, dass die Lage der flüssig-flüssig Binodalen über die Messung der Löslichkeitsprodukte der proto-strukturierten ACCs zugänglich ist. Daher war es möglich ein Phasendiagram für die flüssig-flüssig Mischungslücke des Calciumcarbonat Systems mittels raten- und temperaturabhängigen Titrationsexperimenten zu konstruieren. Das Phasendiagramm weist einen Tripelpunkt auf, an welchem drei verschiedene flüssige $CaCO_3$

Phasen vorliegen, welche sich zu pa-, pc- und pv verfestigen, bei 35 °C, einem pH Wert ~9,5 und einem IAP von $2{,}9 \cdot 10^{-8}$ M². Die Spinodale dieses Systems wurde durch direktes Mischen von Calcium- und Carbonat-Lösungen erhalten und komplettiert damit den linken Ast des Phasendiagrams. Zusätzlich erlauben die Ergebnisse ein Model anzuwenden, um die kritische Temperatur der Mischungslücke mittels Enthalpie ($\Delta H_{cluster}$) und Entropie ($\Delta S_{cluster}$) der Clusterbildung zu berechnen ($T_{crit} = \Delta H_{cluster}/\Delta S_{cluster} = {\sim}98\,K$).

Der Einfluss verschiedener Additive auf die flüssigen Vorstufen und ACC wurden im dritten Teil ausgearbeitet. THz Experimente zeigten, dass Polycarboxylate, welche dafür bekannt sind flüssige Vorstufen zu stabilisieren, die kinetische Stabilität von metastabilen Zuständen deutlich erhöhen, die Lage der Binodalen hingegen nicht verändern. Eine Mischung von verschiedenen Additiven, in diesem Fall Magnesium-Ionen und Polycarboxylaten, wurde mithilfe von Titrationsexperimenten untersucht. Es zeigte sich, dass sowohl Mg^{2+}-Ionen als auch Polyasparaginsäure (PAsp) die Nukleation von Calciumcarbonat inhibieren. Interessanterweise führte eine Kombination der beiden Additive zu einem synergetischen Effekt, welcher die Hemmung einer Addition der einzelnen Effekte auf die flüssigen Vorstufen bei Weitem überstieg. Analysen des ausgefallenen Feststoffs zeigten das Auftreten einer amorphen Phase, welche Calcium- und Magnesium-Ionen in einem äquimolaren Verhältnis enthält. Des Weiteren löst PAsp die Kristallisation aus, da nur in Anwesenheit von PAsp Aragonit beobachtet werden konnte. Daher kann spekuliert werden, dass Magnesium-Ionen den Existenzbereich der flüssigen Calciumcarbonat Vorstufen erweitern, wohingegen PAsp das ACC kinetisch destabilisiert und es so kristallisiert. Diese Ergebnisse könnten drastische Auswirkungen auf das Verständnis der Biomineralisation haben, da Polycarboxylate in Proteinen, welche an der Biomineralisation beteilig sind, vermehrt auftreten und vermutet wird, dass Magnesium-Ionen eine wichtige Rolle in der Biomineralisation einnehmen.

Der abschließende Teil dieser Dissertation beschäftigte sich mit der physikalischen Charakterisierung von flüssigen Calciumcarbonat Vorstufen, welche durch Polycarboxylate stabilisiert wurden. Diese sogenannten „polymer-induzierten“ flüssigen Präkursor (engl. PILP) Phasen, wurden in der Literatur als Paradebeispiel für nicht-klassischen Calciumcarbonat Kristallisation herangezogen.[6] In dieser Arbeit wurden die physikalischen Eigenschaften der PILPs mittels *in-situ* AFM untersucht. Auf einer Calcit-Oberfläche konnten erstmals gelartige Vorstufen beobachtet werden. Eine Auswertung der erhaltenen Daten ergab einen Young

Modulus von ~2 MPa für die untersuchten Vorstufen. Dieser Wert ist mit der Elastizität eines Polyacrylsäure Hydrogels vergleichbar. Das Kristallwachstum auf einer Calcit-Oberfläche wurde über die Zeit hinweg mithilfe von *in-situ* AFM beobachtet. Die zeitabhängigen Experimente zeigten ein Kristallwachstum, welches über die Addition von gelartigen Vorstufen abläuft. Diese Präkursoren waren vor Auftreffen auf die Oberfläche aller Wahrscheinlichkeit nach flüssig.

Zusammenfassend konnte die flüssig-flüssig Binodale im wässrigen Calciumcarbonate System quantitativ lokalisiert werden. Zusätzlich konnte gezeigt werden, dass sich (proto-strukturiertes) ACC *via* Verfestigung und nicht durch ein zweites Nukleationsereignis bildet. Basierend auf diesen Erkenntnissen wurde ein Phasendiagram für die flüssig-flüssig Mischungslücke konstruiert, welches drei proto-strukturierte ACCs berücksichtig. Das Phasendiagram ist ein starkes Indiz, dass im wässrigen $CaCO_3$ System ein flüssiger Polyamorphismus vorliegt, welcher in einem Tripelpunkt mündet an dem drei verschiedene flüssige Phasen koexistieren. Des Weiteren wurde der Einfluss von Additiven, die als elementar für die Biomineralisation angesehen werden, auf die flüssig-flüssig Mischungslücke untersucht und die physikalischen Eigenschaften von stabilisierten flüssigen Vorstufen erforscht. Global gesehen, erweitern diese neuen Erkenntnisse das Verständnis von „nicht-klassischer“ Nukleation und Kristallisation im Allgemeinen und im Speziellen bzgl. der Biomineralisation. Ein wesentlicher Aspekt ist hier weiterhin der Transfer der experimentellen Expertise auf andere Systeme wie Beispielsweise Calciumphosphate oder kleine organische Moleküle wie z. B. Aminosäuren, um die Anwendbarkeit des für die $CaCO_3$ Nukleation etablierten Mechanismus zu eruieren.

“We are all in the gutter, but some of us are looking at the stars”

Oscar Wilde

Lady Windermere’s Fan (1892)

12. References

[1] M. O. Andreae, D. Rosenfeld, *Earth-Science Reviews* 2008, *89*, 13-41.

[2] J. H. Seinfeld, P. N. Pandis, *Atmospheric chemistry and physics: from air pollution to climate change*, John Wiley & Sons, INC., 2006.

[3] R. A. Feely, C. L. Sabine, K. Lee, W. Berelson, J. Kleypas, V. J. Fabry, F. J. Millero, *Science* 2004, *305*, 362-366.

[4] J. Bijma, H. O. Portner, C. Yesson, A. D. Rogers, *Marine Pollution Bulletin* 2013, *74*, 495-505.

[5] M. E. Q. Pilson, *An introduction to the chemistry of the sea*, Cambridge University Press, 2013.

[6] L. B. Gower, *Chem. Rev.* 2008, *108*, 4551-4627.

[7] H. A. Lowenstam, *On biomineralization*, Oxford University Press, New York, 1989.

[8] F. C. Meldrum, H. Cölfen, *Chem. Rev.* 2008, *108*, 4332-4432.

[9] N. Gehrke, N. Nassif, N. Pinna, M. Antonietti, H. S. Gupta, H. Cölfen, *Chemistry of Materials* 2005, *17*, 6514-6516.

[10] J. Aizenberg, A. Tkachenko, S. Weiner, L. Addadi, G. Hendler, *Nature* 2001, *412*, 819-822.

[11] J. H. E. Cartwright, A. G. Checa, *Journal of The Royal Society Interface* 2007, *4*, 491-504.

[12] W. F. Tegethoff, *Calcium Carbonate: From the Cretaceous Period into the 21st Century*, Birkhäuser Basel, 2001.

[13] L. Addadi, S. Weiner, *Angew. Chem. Int. Ed.* 1992, *31*, 153-169.

[14] Y.-Y. Hu, A. Rawal, K. Schmidt-Rohr, *Proc. Natl. Acad. Sci.* 2010, *107*, 22425-22429.

[15] B.-A. Gotliv, N. Kessler, J. L. Sumerel, D. E. Morse, N. Tuross, L. Addadi, S. Weiner, *ChemBioChem* 2005, *6*, 304-314.

[16] J. Rieger, M. Kellermeier, L. Nicoleau, *Angew. Chem. Int. Ed.* 2014, *53*, 12380-12396.

[17] S. L. P. Wolf, K. Jähme, D. Gebauer, *CrystEngComm* 2015, *17*, 6857-6862.

[18] J. W. Gibbs, *Scientific Papers of J. Willard Gibbs...: Thermodynamics, Vol. 1*, Longmans, Green and Company, 1906.

[19] V. I. Kalikmanov, in *Nucleation Theory*, Springer Netherlands, Dordrecht, 2013, pp. 17-41.

[20] M. Volmer, A. Weber, *Zeitschrift Für Physikalische Chemie--Stöchiometrie Und Verwandtschaftslehre* 1926, *119*, 277-301.

[21] M. Volmer, *Zeitschrift Für Physikalische Chemie--Stöchiometrie Und Verwandtschaftslehre* 1922, *102*, 267-275.

[22] J. Frenkel, *J. Chem. Phys.* 1939, *7*, 538-547.

[23] J. M. Stillman, A. J. Cox, *J. Am. Chem. Soc.* 1903, *25*, 732-742.

[24] F. K. Cameron, A. Seidell, *J. Phys. Chem.* 1901, *6*, 50-56.

[25] D. Gebauer, M. Kellermeier, J. D. Gale, L. Bergström, H. Cölfen, *Chem. Soc. Rev.* 2014, *43*, 2348-2371.

[26] D. Gebauer, H. Cölfen, *Nano Today* 2011, *6*, 564-584.

[27] R. Becker, W. Doring, *Annalen Der Physik* 1935, *24*, 719-752.

[28] L. Farkas, *Zeitschrift Fur Physikalische Chemie--Stochiometrie Und Verwandtschaftslehre* 1927, *125*, 236-242.

[29] J. B. Zeldovich, *Acta Physicochimica Urss* 1943, *18*, 1-22.

[30] J. W. Mullin, *Crystallization*, 4 ed., Butterworth-Heinemann, 2001.

[31] A. E. Nielsen, *Kinetics of precipitation*, Pergamon Press; [distributed in the Western Hemisphere by Macmillan, New York], 1964.

[32] J. J. De Yoreo, P. G. Vekilov, *Reviews in Mineralogy and Geochemistry* 2003, *54*, 57-93.

[33] H. H. Teng, P. M. Dove, C. A. Orme, J. J. De Yoreo, *Science* 1998, *282*, 724-727.

[34] Q. Hu, M. H. Nielsen, C. L. Freeman, L. M. Hamm, J. Tao, J. R. I. Lee, T. Y. J. Han, U. Becker, J. H. Harding, P. M. Dove, J. J. De Yoreo, *Faraday Discuss.* 2012, *159*, 509-523.

[35] D. Kashchiev, *The Journal of Chemical Physics* 2008, *129*, 164701.

[36] D. Gebauer, A. Völkel, H. Cölfen, *Science* 2008, *322*, 1819-1822.

[37] K. Onuma, A. Ito, *Chemistry of Materials* 1998, *10*, 3346-3351.

[38] M. Kellermeier, R. Rosenberg, A. Moise, U. Anders, M. Przybylski, H. Cölfen, *Faraday Discuss.* 2012, *159*, 23-45.

[39] J. Scheck, B. Wu, M. Drechsler, R. Rosenberg, A. E. S. Van Driessche, T. M. Stawski, D. Gebauer, *The Journal of Physical Chemistry Letters* 2016, *7*, 3123-3130.

[40] R. Demichelis, P. Raiteri, J. D. Gale, D. Quigley, D. Gebauer, *Nat Commun* 2011, *2*, 590.

[41] A. F. Wallace, L. O. Hedges, A. Fernandez-Martinez, P. Raiteri, J. D. Gale, G. A. Waychunas, S. Whitelam, J. F. Banfield, J. J. De Yoreo, *Science* 2013, *341*, 885-889.

[42] M. Faatz, F. Gröhn, G. Wegner, *Adv. Mater.* 2004, *16*, 996-1000.

[43] L. A. Gower, D. A. Tirrell, *J. Cryst. Growth* 1998, *191*, 153-160.

[44] L. B. Gower, D. J. Odom, *J. Cryst. Growth* 2000, *210*, 719-734.

[45] L. Dai, E. P. Douglas, L. B. Gower, *Journal of Non-Crystalline Solids* 2008, *354*, 1845-1854.

[46] S. Weiner, L. Addadi, *Trends in Biochemical Sciences* 1991, *16*, 252-256.

[47] G. Falini, S. Albeck, S. Weiner, L. Addadi, *Science* 1996, *271*, 67-69.

[48] M. J. Olszta, D. J. Odom, E. P. Douglas, L. B. Gower, *Connective Tissue Research* 2003, *44*, 326-334.

[49] M. J. Olszta, X. Cheng, S. S. Jee, R. Kumar, Y.-Y. Kim, M. J. Kaufman, E. P. Douglas, L. B. Gower, *Materials Science and Engineering: R: Reports* 2007, *58*, 77-116.

[50] S. E. Wolf, J. Leiterer, M. Kappl, F. Emmerling, W. Tremel, *J. Am. Chem. Soc.* 2008, *130*, 12342-12347.

[51] S. E. Wolf, L. Muller, R. Barrea, C. J. Kampf, J. Leiterer, U. Panne, T. Hoffmann, F. Emmerling, W. Tremel, *Nanoscale* 2011, *3*, 1158-1165.

[52] M. A. Bewernitz, D. Gebauer, J. Long, H. Cölfen, L. B. Gower, *Faraday Discuss.* 2012, *159*, 291-312.

[53] D. Gebauer, P. N. Gunawidjaja, J. Y. P. Ko, Z. Bacsik, B. Aziz, L. Liu, Y. Hu, L. Bergström, C.-W. Tai, T.-K. Sham, M. Edén, N. Hedin, *Angew. Chem. Int. Ed.* 2010, *49*, 8889-8891.

[54] L. Kabalah-Amitai, B. Mayzel, Y. Kauffmann, A. N. Fitch, L. Bloch, P. U. P. A. Gilbert, B. Pokroy, *Science* 2013, *340*, 454-457.

[55] J. H. E. Cartwright, A. G. Checa, J. D. Gale, D. Gebauer, C. I. Sainz-Díaz, *Angew. Chem. Int. Ed.* 2012, *51*, 11960-11970.

[56] M. Farhadi-Khouzani, D. M. Chevrier, P. Zhang, N. Hedin, D. Gebauer, *Angew. Chem. Int. Ed.* 2016, *55*, 8117-8120.

[57] Y. Levi-Kalisman, S. Raz, S. Weiner, L. Addadi, I. Sagi, *Adv. Funct. Mater.* 2002, *12*, 43-48.

[58] L. Addadi, S. Raz, S. Weiner, *Adv. Mater.* 2003, *15*, 959-970.

[59] J. Aizenberg, G. Lambert, S. Weiner, L. Addadi, *J. Am. Chem. Soc.* 2001, *124*, 32-39.

[60] J. Mahamid, A. Sharir, L. Addadi, S. Weiner, *Proc. Natl. Acad. Sci.* 2008, *105*, 12748-12753.

[61] J. Seto, Y. Ma, S. A. Davis, F. Meldrum, A. Gourrier, Y.-Y. Kim, U. Schilde, M. Sztucki, M. Burghammer, S. Maltsev, C. Jäger, H. Cölfen, *Proc. Natl. Acad. Sci.* 2012, *109*, 3699-3704.

[62] H. Cölfen, M. Antonietti, *Angew. Chem. Int. Ed.* 2005, *44*, 5576-5591.

[63] Y. Politi, D. R. Batchelor, P. Zaslansky, B. F. Chmelka, J. C. Weaver, I. Sagi, S. Weiner, L. Addadi, *Chemistry of Materials* 2010, *22*, 161-166.

[64] W. J. E. M. Habraken, A. Masic, L. Bertinetti, A. Al-Sawalmih, L. Glazer, S. Bentov, P. Fratzl, A. Sagi, B. Aichmayer, A. Berman, *Journal of Structural Biology* 2015, *189*, 28-36.

[65] R. A. Berner, *Geochimica et Cosmochimica Acta* 1975, *39*, 489-504.

[66] S. Raz, S. Weiner, L. Addadi, *Adv. Mater.* 2000, *12*, 38-42.

[67] S. Weiner, J. Mahamid, Y. Politi, Y. Ma, L. Addadi, *Frontiers of Materials Science in China* 2009, *3*, 104-108.

[68] S. Weiner, L. Addadi, in *Annual Review of Materials Research, Vol 41, Vol. 41* (Eds.: D. R. Clarke, P. Fratzl), 2011, pp. 21-40.

[69] J. K. Berg, T. Jordan, Y. Binder, H. G. Börner, D. Gebauer, *J. Am. Chem. Soc.* 2013, *135*, 12512-12515.

[70] G. Falini, M. Gazzano, A. Ripamonti, *J. Cryst. Growth* 1994, *137*, 577-584.

[71] J. Tao, D. Zhou, Z. Zhang, X. Xu, R. Tang, *Proc. Natl. Acad. Sci.* 2009, *106*, 22096-22101.

[72] D. Wang, A. F. Wallace, J. J. De Yoreo, P. M. Dove, *Proc. Natl. Acad. Sci.* 2009, *106*, 21511-21516.

[73] L. Wang, G. H. Nancollas, *Chem. Rev.* 2008, *108*, 4628-4669.

[74] D. Gebauer, A. Verch, H. G. Börner, H. Cölfen, *Crystal Growth & Design* 2009, *9*, 2398-2403.

[75] D. Gebauer, H. Cölfen, A. Verch, M. Antonietti, *Adv. Mater.* 2009, *21*, 435-439.

[76] A. Verch, D. Gebauer, M. Antonietti, H. Cölfen, *Phys. Chem. Chem. Phys.* 2011, *13*, 16811-16820.

[77] A. Picker, M. Kellermeier, J. Seto, D. Gebauer, H. Cölfen, in *Zeitschrift für Kristallographie - Crystalline Materials, Vol. 227*, 2012, p. 744.

[78] A. Rao, J. K. Berg, M. Kellermeier, D. Gebauer, *European Journal of Mineralogy* 2014, *26*, 537-552.

[79] A. Verch, M. Antonietti, H. Cölfen, in *Zeitschrift für Kristallographie - Crystalline Materials, Vol. 227*, 2012, p. 718.

[80] J. J. De Yoreo, P. U. P. A. Gilbert, N. A. J. M. Sommerdijk, R. L. Penn, S. Whitelam, D. Joester, H. Zhang, J. D. Rimer, A. Navrotsky, J. F. Banfield, A. F. Wallace, F. M. Michel, F. C. Meldrum, H. Cölfen, P. M. Dove, *Science* 2015, *349*.

[81] H. Cölfen, S. Mann, *Angew. Chem. Int. Ed.* 2003, *42*, 2350-2365.

[82] R. L. Penn, J. F. Banfield, *Geochimica et Cosmochimica Acta* 1999, *63*, 1549-1557.

[83] Q. Zhang, S. J. Liu, S. H. Yu, *Journal of Materials Chemistry* 2009, *19*, 191-207.

[84] L. Bergström, E. V. Sturm, G. Salazar-Alvarez, H. Cölfen, *Accounts of Chemical Research* 2015, *48*, 1391-1402.

[85] H. Cölfen, M. Antonietti, *Mesocrystals and nonclassical crystallization*, Wiley, 2008.

[86] O. Galkin, P. G. Vekilov, *J. Am. Chem. Soc.* 2000, *122*, 156-163.

[87] P. G. Vekilov, *Nanoscale* 2010, *2*, 2346-2357.

[88] O. Gliko, N. Neumaier, W. Pan, I. Haase, M. Fischer, A. Bacher, S. Weinkauf, P. G. Vekilov, *J. Am. Chem. Soc.* 2005, *127*, 3433-3438.

[89] Y. Ma, G. Mehltretter, C. Plüg, N. Rademacher, M. U. Schmidt, H. Cölfen, *Adv. Funct. Mater.* 2009, *19*, 2095-2101.

[90] Y. Jiang, L. Gower, D. Volkmer, H. Cölfen, *Phys. Chem. Chem. Phys.* 2012, *14*, 914-919.

[91] S. Wohlrab, H. Cölfen, M. Antonietti, *Angew. Chem. Int. Ed.* 2005, *44*, 4087-4092.

[92] M. J. Olszta, S. Gajjeraman, M. Kaufman, L. B. Gower, *Chemistry of Materials* 2004, *16*, 2355-2362.

[93] X. Cheng, P. L. Varona, M. J. Olszta, L. B. Gower, *J. Cryst. Growth* 2007, *307*, 395-404.

[94] T. Thula-Mata, A. Burwell, L. B. Gower, S. Habelizt, G. Marshall, *MRS Online Proceedings Library* 2011, *1355*.

[95] A. K. Burwell, T. Thula-Mata, L. B. Gower, S. Habeliz, M. Kurylo, S. P. Ho, Y. C. Chien, J. Cheng, N. F. Cheng, S. A. Gansky, S. J. Marshall, G. W. Marshall, *PLoS One* 2012, *7*, e38852.

[96] H. Galster, *pH-Messung*, VCH Weinheim, Winheim, 1990.

[97] U. Oesch, Z. Brzozka, A. P. Xu, B. Rusterholz, G. Suter, H. V. Pham, D. H. Welti, D. Ammann, E. Pretsch, W. Simon, *Anal. Chem.* 1986, *58*, 2285-2289.

[98] H.-l. Wu, R.-Q. Yu, *Talanta* 1987, *34*, 577-579.

[99] K. Cammann, H. Galster, *Das Arbeiten mit ionenselektiven Elektroden*, Springer-Verlag Berlin Heidelberg New York, 1996.

[100] D. Ammann, *Ion-Selective Micro-electroedes*, Springer-Verlag Berlin Heidelberg New York, 1986.

[101] P. W. Hawkes, J. C. H. Spence, *Science of Microscopy, Vol. 1*, Springer Verlag Berlin Heidelberg Ney York, 2008.

[102] R. A. Robinson, R. H. Stokes, *Electrolyte solutions*, Courier Corporation, 2002.

[103] P. Debye, E. Huckel, *Physikalische Zeitschrift* 1923, *24*, 185-206.

[104] F. Malatesta, *Journal of Solution Chemistry* 2000, *29*, 771-779.

[105] J. Kielland, *J. Am. Chem. Soc.* 1937, *59*, 1675-1678.

[106] H. S. Harned, S. R. Scholes, *J. Am. Chem. Soc.* 1941, *63*, 1706-1709.

[107] F. C. Meldrum, R. P. Sear, *Science* 2008, *322*, 1802-1803.

[108] L. Brečević, A. E. Nielsen, *J. Cryst. Growth* 1989, *98*, 504-510.

[109] A. D. Visscher, J. Vanderdeelen, *J. Phys. Chem. Ref. Data* 2012, *41*, 023105-023105-023137.

[110] M. Kellermeier, A. Picker, A. Kempter, H. Cölfen, D. Gebauer, *Adv. Mater.* 2014, *26*, 752-757.

[111] M. Kellermeier, P. Raiteri, J. K. Berg, A. Kempter, J. D. Gale, D. Gebauer, *ChemPhysChem* 2016, *17*, 3535-3541.

[112] A. Bergner, U. Heugen, E. Bründermann, G. Schwaab, M. Havenith, D. R. Chamberlin, E. E. Haller, *Review of Scientific Instruments* 2005, *76*, 063110.

[113] E. Bründermann, D. R. Chamberlin, E. E. Haller, *Applied Physics Letters* 2000, *76*, 2991-2993.

[114] F. Sebastiani, S. L. P. Wolf, B. Born, T. Q. Luong, H. Cölfen, D. Gebauer, M. Havenith, *Angew. Chem. Int. Ed.* 2017, *56*, 490-495.

[115] S. L. P. Wolf, L. Caballero, F. Melo, H. Cölfen, *Langmuir* 2017, *33*, 158-163.

[116] R. Buchner, J. Barthel, J. Stauber, *Chemical Physics Letters* 1999, *306*, 57-63.

[117] D. S. Venables, C. A. Schmuttenmaer, *The Journal of Chemical Physics* 1998, *108*, 4935-4944.

[118] J. T. Kindt, C. A. Schmuttenmaer, *Journal of Physical Chemistry* 1996, *100*, 10373-10379.

[119] C. Rønne, P.-O. Åstrand, S. R. Keiding, *Physical Review Letters* 1999, *82*, 2888-2891.

[120] J. T. Kindt, C. A. Schmuttenmaer, *J. Phys. Chem.* 1996, *100*, 10373-10379.

[121] C. Rønne, P.-O. Åstrand, S. R. Keiding, *Phys. Rev. Lett.* 1999, *82*, 2888-2891.

[122] T. Q. Luong, P. K. Verma, R. K. Mitra, M. Havenith, *J. Phys. Chem. A* 2011, *115*, 14462-14469.

[123] A. Patra, T. Q. Luong, R. K. Mitra, M. Havenith, *Physical Chemistry Chemical Physics* 2014.

[124] U. Heugen, G. Schwaab, E. Bründermann, M. Heyden, X. Yu, D. M. Leitner, M. Havenith, *Proc. Natl. Acad. Sci.* 2006, *103*, 12301-12306.

[125] S. Funkner, G. Niehues, D. A. Schmidt, M. Heyden, G. Schwaab, K. M. Callahan, D. J. Tobias, M. Havenith, *J. Am. Chem. Soc.* 2012, *134*, 1030-1035.

[126] V. Sharma, F. Böhm, M. Seitz, G. Schwaab, M. Havenith, *Phys. Chem. Chem. Phys.* 2013, *15*, 8383-8391.

[127] V. Sharma, F. Böhm, G. Schwaab, M. Havenith, *Phys. Chem. Chem. Phys.* 2014, *16*, 25101-25110.

[128] F. Böhm, V. Sharma, G. Schwaab, M. Havenith, *Phys. Chem. Chem. Phys.* 2015, *17*, 19582-19591.

[129] J.-Y. Gal, J.-C. Bollinger, H. Tolosa, N. Gache, *Talanta* 1996, *43*, 1497-1509.

[130] M. H. Nielsen, S. Aloni, J. J. De Yoreo, *Science* 2014, *345*, 1158-1162.

[131] M. Kellermeier, D. Gebauer, E. Melero-García, M. Drechsler, Y. Talmon, L. Kienle, H. Cölfen, J. M. García-Ruiz, W. Kunz, *Adv. Funct. Mater.* 2012, *22*, 4301-4311.

[132] H. Hull, A. G. Turnbull, *Geochimica et Cosmochimica Acta* 1973, *37*, 685-694.

[133] E. Loste, R. M. Wilson, R. Seshadri, F. C. Meldrum, *J. Cryst. Growth* 2003, *254*, 206-218.

[134] J. Aizenberg, L. Addadi, S. Weiner, G. Lambert, *Adv. Mater.* 1996, *8*, 222-226.

[135] C. Günther, A. Becker, G. Wolf, M. Epple, *Z. Anorg. Allg. Chem.* 2005, *631*, 2830-2835.

[136] Y. Kojima, A. Kawanobe, T. Yasue, Y. Arai, *Nippon Seramikkusu Kyokai Gakujutsu Ronbunshi-Journal of the Ceramic Society of Japan* 1994, *102*, 1128-1136.

[137] R. S. K. Lam, J. M. Charnock, A. Lennie, F. C. Meldrum, *CrystEngComm* 2007, *9*, 1226-1236.

[138] N. V. Vagenas, A. Gatsouli, C. G. Kontoyannis, *Talanta* 2003, *59*, 831-836.

[139] J. D. Rodriguez-Blanco, S. Shaw, P. Bots, T. Roncal-Herrero, L. G. Benning, *Geochimica et Cosmochimica Acta* 2014, *127*, 204-220.

[140] N. Khan, D. Dollimore, K. Alexander, F. W. Wilburn, *Thermochimica Acta* 2001, *367–368*, 321-333.

[141] L. Caballero, J. Mena, A. Morales-Alvarez, M. J. Kogan, F. Melo, *Langmuir* 2015, *31*, 299-306.

[142] R. Gonzalez, L. Caballero, J. Pavez, F. Melo, *Langmuir* 2012, *28*, 9506-9514.

[143] L. Sonnenberg, Y. Luo, H. Schlaad, M. Seitz, H. Cölfen, H. E. Gaub, *J. Am. Chem. Soc.* 2007, *129*, 15364-15371.

[144] J. J. De Yoreo, S. Chung, R. W. Friddle, *Adv. Funct. Mater.* 2013, *23*, 2525-2538.

[145] E. Ruiz-Agudo, C. V. Putnis, C. Jiménez-López, C. Rodriguez-Navarro, *Geochimica et Cosmochimica Acta* 2009, *73*, 3201-3217.

[146] E. K. Dimitriadis, F. Horkay, J. Maresca, B. Kachar, R. S. Chadwick, *Biophys. J.* 2002, *82*, 2798-2810.

[147] K. L. Johnson, K. Kendall, A. D. Roberts, *Proceedings of the Royal Society of London A: Mathematical, Physical and Engineering Sciences* 1971, *324*, 301-313.

[148] Y.-J. Lin, F.-C. Hsu, C.-W. Chou, T.-H. Wu, H.-R. Lin, *Journal of Materials Chemistry B* 2014, *2*, 8329-8337.

[149] S. Sun, L.-B. Mao, Z. Lei, S.-H. Yu, H. Cölfen, *Angew. Chem. Int. Ed.* 2016, *55*, 11765-11769.

[150] L. Sirghi, F. Rossi, *Appl. Phys. Lett.* 2006, *89*, 243118.

[151] W. Kossel, *Annalen der Physik* 1934, *413*, 457-480.

[152] R. A. Metzler, G. A. Tribello, M. Parrinello, P. U. P. A. Gilbert, *J. Am. Chem. Soc.* 2010, *132*, 11585-11591.

[153] Y. G. Kuznetsov, A. J. Malkin, A. McPherson, *J. Cryst. Growth* 2001, *232*, 30-39.

13. Appendix

Table 3 IAP and supersaturation values for different experiments at pH 9 for 0.1 µmol/min addition rate

	IAP_{max} (10^{-8} M²)	IAP_{nuc} (10^{-8} M²)	S
15°C	9.4±1.9	3.8±0.4	2.4
25°C	7.0±0.4	3.2±0.4	2.2
35°C	7.0±0.06	2.9±0.1	2.4
45°C	4.7±0.4	2.4±0.2	2.0

Table 4 IAP and supersaturation values for different experiments at pH 9 for 1.0 µmol/min addition rate

	IAP_{max} (10^{-8} M²)	IAP_{nuc} (10^{-8} M²)	S
15°C	22.6±2.6	8.2±1.1	2.8
25°C	18.6±0.6	6.5±0.7	2.8
35°C	10.9±0.1	3.8±0.2	2.8
45°C	7.1±1.2	2.8±0.2	2.5

Table 5 IAP and supersaturation values for different experiments at pH 9 for 10.0 µmol/min addition rate

	IAP_{max} (10^{-8} M²)	IAP_{nuc} (10^{-8} M²)	S
15°C	51.4±2.0	17.8±5.0	2.8
25°C	42.6±3.6	16.4±1.1	2.8
35°C	26.6±0.5	7.4±0.4	3.6
45°C	14.3±0.7	4.8±0.5	2.9

Table 6 IAP and supersaturation values for different experiments at pH 10 for 0.1 µmol/min addition rate

	IAP_{max} (10^{-8} M²)	IAP_{nuc} (10^{-8} M²)	S
15°C	18.7±1.5	7.6±0.5	2.5
25°C	11.6±0.9	3.9±0.4	3.0
35°C	6.8±0.3	2.7±0.2	2.5
45°C	6.5 ±0.4	3.0±0.3	2.1

Table 7 IAP and supersaturation values for different experiments at pH 10 for 1.0 µmol/min addition rate

	IAP_{max} (10^{-8} M²)	IAP_{nuc} (10^{-8} M²)	S
15°C	36.2±2.4	12.7±1.7	2.8
25°C	25±0.8	8.9±0.8	2.8
35°C	12.2±0.6	3.7±0.7	3.2
45°C	12.9 ±1.0	3.8±0.2	3.4

Table 8 IAP and supersaturation values for different experiments at pH 10 for 10.0 µmol/min addition rate

	IAP_{max} (10^{-8} M²)	IAP_{nuc} (10^{-8} M²)	S
15°C	97.2±25	30.4±1.0	3.2
25°C	65.1±4.4	15.8±3.8	4.1
35°C	34.6±4.8	6.4±2.0	5.4
45°C	36.4 ±1.2	5.0±0.3	7.3

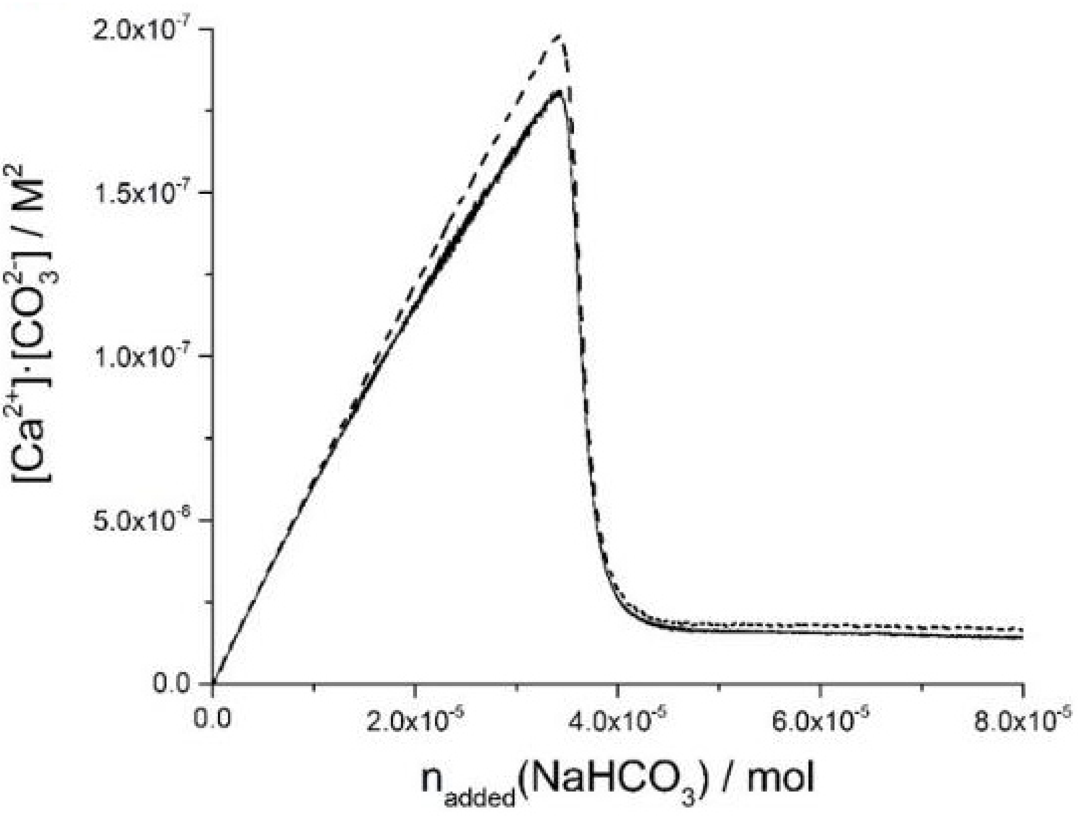

Figure 42 | Showing the two different calculation approaches from the sodium hydroxide data only (black dashed curve) and for the case where the calcium concentration is measured by the calcium ISE (black solid line).

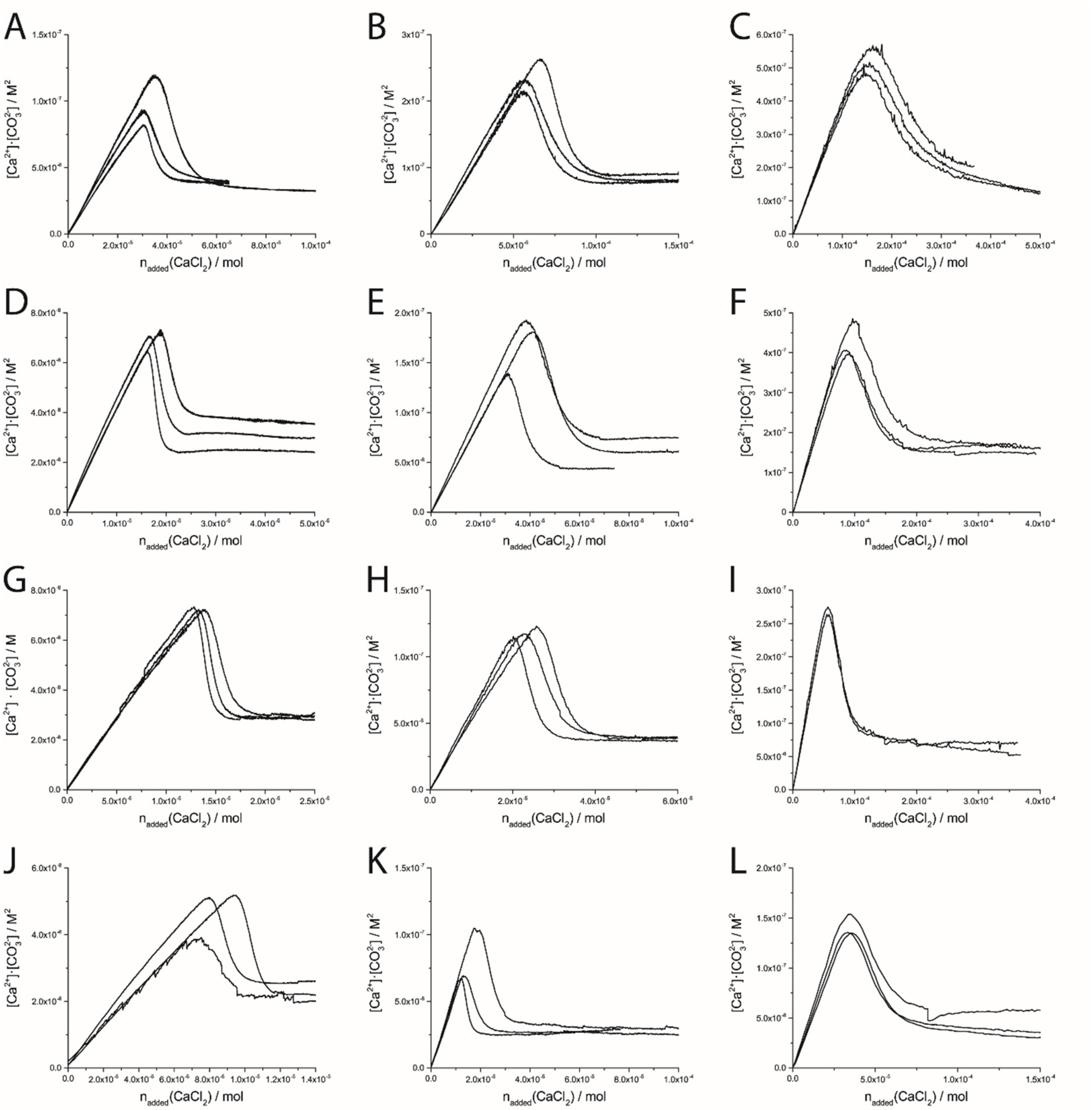

Figure 43 Reproducibility of the experiments performed at pH 9.0. At different temperatures and addition rates. T = 15°C: A – C; T = 25°C: D – F; T = 35°C: G – I; T = 45°C: J – L; 0.1 µmol/min: A, D, G, J; 1.0 µmol/min: B, E, H, K; 10 µmol/min: C, F, I, L.

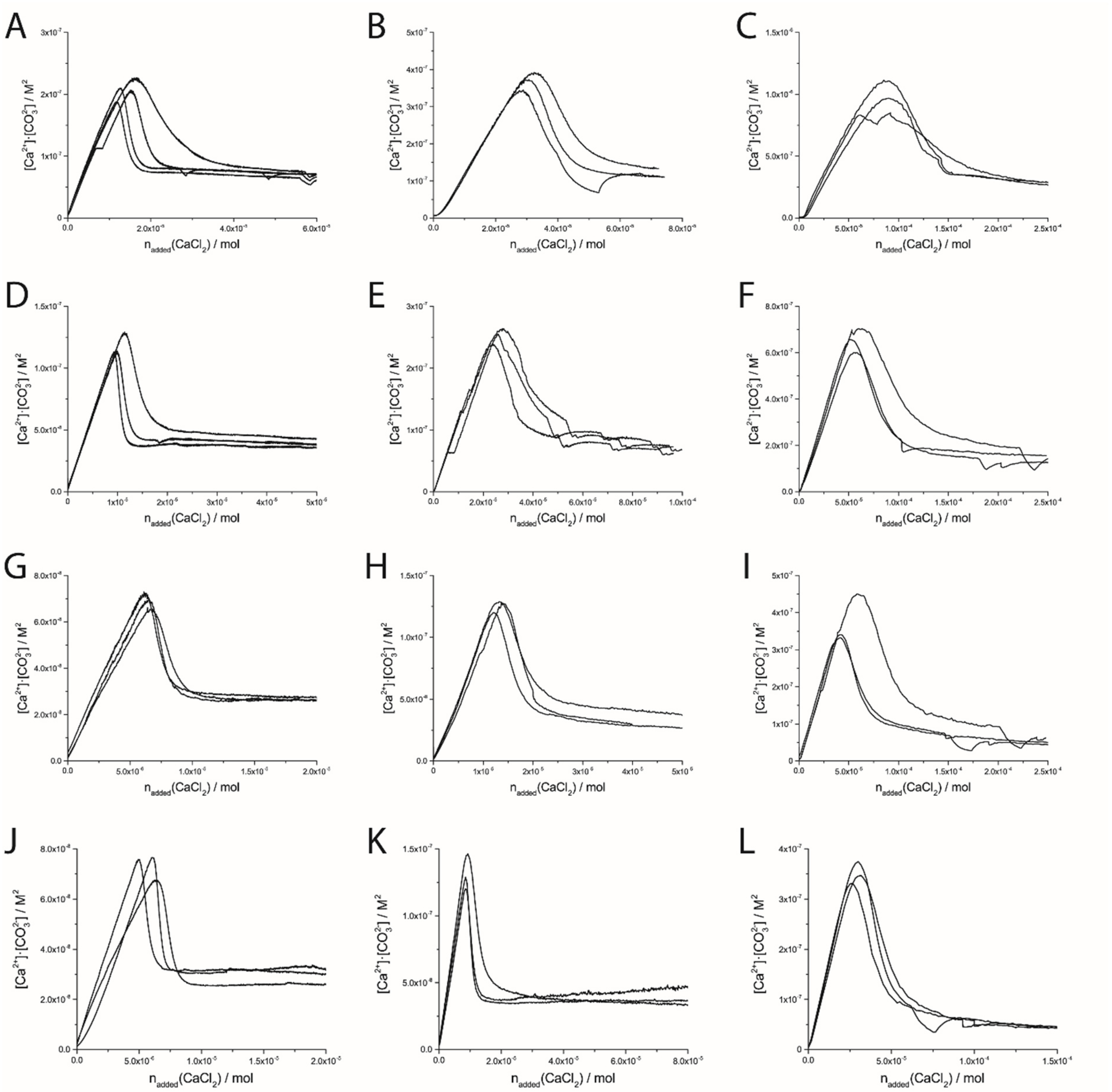

Figure 44 Reproducibility of the experiments performed at pH 10.0. At different temperatures and addition rates. T = 15°C: A – C; T = 25°C: D – F; T = 35°C: G – I; T = 45°C: J – L; 0.1 µmol/min: A, D, G, J; 1.0 µmol/min: B, E, H, K; 10 µmol/min: C, F, I, L.

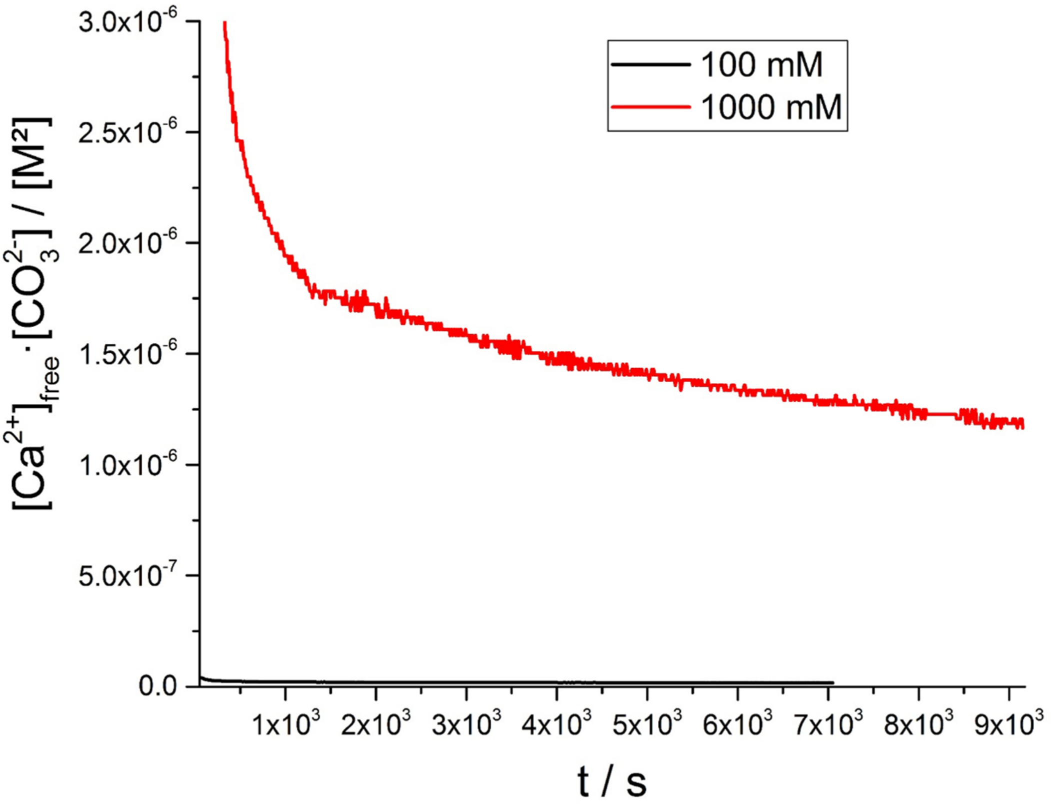

Figure 45 | A plot of the IAP over time resulting from the direct mixing experiments of a 100 mM calcium chloride solution and a 100 mM carbonate buffer (black) and of a direct mixing experiment of a 1000 mM calcium chloride solution a 1000 mM carbonate buffer (red)

List of Abbreviations

PNC	pre-nucleation cluster
r	radius
γ	surface tension
ΔG_v	free energy change of the transformation per unit volume
S	supersaturation
IAP	ion activity product
IP	ion product
K_{sp},	solubility constant
T	absolute Temperature
k_B	Boltzmann constant
ν	the molecular volume
J	nucleation rates
CNT	classical nucleation theory
DOLLOPs	dynamically ordered liquid like oxyanion polymers
ACC	amorphous calcium carbonate
PAsp	poly(aspartic acid)
PAA	Poly(acrylic acid)
PILP	polymer induced liquid precursor
TEM	transmission electron microscopy

SEM	scanning electron microscopy
cryo	cryogenic
NMR	nuclear magnetic resonance
TDDA	tridodecylamine
MDUDA	methyldioctadecylamine
ISE	ion selective electrode
kV	kilo Volt
nm	nanometer
mL	milliliter
μmol	micromol
g	gram
mM	milli-molar
min	minutes
a	activity
γ	activity coefficient
U	measured potential
U_0	standard potential
R	universal gas constant
$a^{\oplus}$	standard activity
z	the charge valence

F	Faraday constant
c	concentration
n	amount of substance
V	volume
THz-TD	Terahertz Time Domain
ATR FT-IR,	attenuated total reflection Fourier transformed infra-red
TGA	Thermogravimetric analysis
EDX	energy-dispersive X-ray spectroscopy
K	Kelvin
AFM	atomic force microscopy
Y	Young’s modulus
F	force
W_{adh}	work of adhesion
SAXS	small angle X-ray scattering

Table of Figures

List of Tables